Technische Universität München
TUM School of Medicine and Health

Optoacoustics in lipid metabolism and metabolic disorders

Nikolina Alexia Fasoula

Vollständiger Abdruck der von der TUM School of Medicine and Health der Technischen Universität München zur Erlangung einer

Doktorin der Naturwissenschaften **(Dr.rer.nat.)**

genehmigten Dissertation.

Vorsitz: Prof. Dr. Henning Wackerhage

Prüfende der Dissertation:

1. Prof. Dr. Vasilis Ntziachristos
2. Prof. Dr. Paul Thomas Pfluger
3. Prof. Nikolaos Papanas

Die Dissertation wurde am 28. Dezember 2023 bei der Technischen Universität München eingereicht und durch die TUM School of Medicine and Health am 7. August 2024 angenommen.

Technical University of Munich

TUM School of Medicine and Health (MH)

Chair of Biological Imaging

Optoacoustics in lipid metabolism and metabolic disorders

Nikolina Alexia Fasoula

Munich, 2023

Acknowledgments

First, I would like to extend my heartfelt gratitude to those who stimulated critical thinking and reshaped my perspectives.

I am deeply thankful to those who guided me through challenges with unwavering support and to those who attentively listened to my concerns and offered valuable advice with respect.

Moreover, I would like to express my appreciation to my colleagues (K.A., K.N., B.M., R.M., and O.I.) for their collaborative spirit, help, and support, which have played a vital role in our shared achievements.

Lastly, I am indebted to my family and friends for their unshakeable faith in me.

Nikolina Alexia Fasoula

“In order to succeed, we must first believe that we can.”

— *Nikos Kazantzakis*

Abstract

Optoacoustics is a powerful, non-invasive imaging technique that combines the benefits of both optical and ultrasound imaging. It holds great potential for the imaging of hemoglobin and lipids, among other molecules, providing valuable insights into their spatial distribution and dynamics within biological tissues. By taking advantage of the inherent light absorption properties of hemoglobin and lipids, acoustic responses are generated and recorded when these molecules absorb light pulses. Detection and processing of the acoustic waves enable the visualization and quantification of the chromophores mentioned above within the blood vessels, soft tissues, and parenchymal organs, such as the adipose tissues, liver, skin, and skeletal muscles. Such visualizations provide the user with detailed insights into not only tissue physiology but also the pathophysiology of relevant metabolic diseases, such as obesity and diabetes. In this work, we employ optoacoustic techniques to investigate different aspects of metabolism and metabolic disease, as reflected in the hemoglobin- and lipid-specific changes induced in affected tissues and organs, such as the blood, the liver, and the skin. In particular, we first explore the lipid dynamics in the bloodstream after the oral consumption of a high-fat meal, hypothesizing that imaging of postprandial lipemia using multispectral optoacoustic tomography (MSOT) would provide an innovative approach for studying postprandial lipid dynamics: a feature that is distorted in various health conditions. By employing multiple wavelengths of near-infrared light (680-980 nm) and analyzing the resulting optoacoustic signals, this technique allowed for the comprehensive mapping of lipid distribution within not only blood vessels but also different tissue compartments, such as the subcutaneous fat and muscle. With MSOT, we demonstrate for the first time the unique capability of the technology to accurately image the temporal fluctuations of lipids within tissues in healthy volunteers based only on the characteristic absorption peak of the lipids when illuminated at 930 nm.

Furthermore, apart from dynamic lipid readouts, we further explore the capability of MSOT to detect lipids in parenchymal organs, such as the human liver, lying at depths of several cm under the skin surface. Thus, as a next step, we captured MSOT images of subjects with already diagnosed hepatic steatosis, a disorder characterized by intrahepatic fat accumulation, which deteriorates the function of the hepatic tissue, leading to potential progression to more severe conditions. In this study, we demonstrate for the first time the capability of MSOT to image hepatic steatosis in humans. Here, we also include data from a relevant mouse model (high-fat diet), which underlines the excellent translational potential of MSOT. Our non-invasive approach holds promise for early detection or even for the assessment of treatment responses in future patients with hepatic steatosis.

Finally, in another study, we employ raster-scan optoacoustic mesoscopy (RSOM) to image the microvasculature of the skin in patients with diabetes. By using green light (532 nm), we were able to

produce high-resolution (7-10 µm) images of the skin microvasculature in healthy volunteers and patients with diabetes based on the strong presence of hemoglobin in the skin. RSOM revealed a degradation of the skin microvasculature in diabetes by detecting the statistically significant lower number of vessels and blood volume compared to the healthy group. Our findings provided important insights into the microangiopathy related to diabetes and displayed once again the great potential of the RSOM technology as a tool for translational research and future clinical practice. Overall, optoacoustic imaging holds significant potential for imaging different aspects of tissue physiology and its distortion in disease. By exploiting the unique features of optoacoustics and through detailed design and conduction, our studies aim to improve our understanding of various diseases such as obesity, non-alcoholic fatty liver disease (NAFLD), and diabetes, and to facilitate the management of these patients in the future.

Zusammenfassung

Die Optoakustik ist ein leistungsfähiges nicht-invasives Bildgebungsverfahren, das die Vorteile der optischen Bildgebung und der Ultraschall-Bildgebung vereint. Sie birgt großes Potenzial für die Darstellung von Hämoglobin, Lipiden und anderen Molekülen und bietet wertvolle Einblicke in deren räumliche Verteilung sowie Dynamik in biologischen Geweben. Unter Ausnutzung der inhärenten Lichtabsorptionseigenschaften von Hämoglobin und Lipiden werden akustische Reaktionen erzeugt und aufgezeichnet, wenn diese Moleküle Lichtimpulse absorbieren. Die Erkennung und Verarbeitung der akustischen Wellen ermöglicht die Visualisierung und Quantifizierung der oben genannten Chromophore in Blutgefäßen, Weichteilen und parenchymatösen Organen wie Fettgewebe, Leber, Haut und Skelettmuskeln. Derartige Visualisierungen bieten dem Nutzer nicht nur detaillierte Einblicke in die Gewebephysiologie, sondern auch in die Pathophysiologie relevanter Stoffwechselkrankheiten wie Fettleibigkeit und Diabetes. In dieser Arbeit setzen wir optoakustische Verfahren ein, um verschiedene Aspekte des Stoffwechsels und Stoffwechselkrankheiten zu untersuchen, die sich in den hämoglobin- und lipidspezifischen Veränderungen in den betroffenen Geweben und Organen wie dem Blut, der Leber und der Haut niederschlagen. Insbesondere untersuchen wir zunächst die Lipiddynamik im Blutkreislauf nach dem oralen Verzehr einer fettreichen Mahlzeit und stellten die Hypothese auf, dass die Darstellung der postprandialen Lipämie mittels multispektraler optoakustischer Tomographie (MSOT) einen innovativen Ansatz für die Untersuchung der postprandialen Lipiddynamik bieten würde, welche bei verschiedenen Gesundheitszuständen gestört ist. Durch die Verwendung mehrerer Wellenlängen von Licht im Nahinfrarotbereich (680-980 nm) und die Analyse der daraus resultierenden optoakustischen Signale ermöglichte diese Technik nicht nur in den Blutgefäßen eine umfassende Kartierung der Lipidverteilung, sondern auch in verschiedenen Gewebekompartimenten wie dem subkutanen Fett und den Muskeln. Mit MSOT demonstrieren wir zum ersten Mal die einzigartige Fähigkeit der Technologie, die zeitlichen Fluktuationen von Lipiden im Gewebe gesunder Probanden allein auf der Grundlage des charakteristischen Absorptionspeaks der Lipide bei einer Beleuchtung von 930 nm präzise darzustellen.

Darüber hinaus erforschen wir neben der dynamischen Lipidmessung auch die Fähigkeit von MSOT, Lipide in parenchymatösen Organen zu erkennen, die mehrere Zentimeter unter der Hautoberfläche liegen, wie z. B. in der menschlichen Leber. In einem nächsten Schritt erfassten wir MSOT Daten von Personen mit bereits diagnostizierter Lebersteatose, einer Erkrankung, die durch intrahepatische Fettanhäufung gekennzeichnet ist, welche die Funktion des Lebergewebes verschlechtert und zu Leberfunktionsstörungen führt, die sich potentiell zu schwereren Erkrankungen ausweiten. In dieser

Studie zeigen wir erstmalig die Fähigkeit von MSOT Lebersteatose beim Menschen darzustellen. Hierbei beziehen wir auch Daten von einem relevanten Mausmodell (fettreiche Diät) ein, die das hervorragende translationale Potenzial von MSOT unterstreichen. Unser nicht-invasiver Ansatz ist vielversprechend für die frühzeitige Erkennung von Lebersteatose oder sogar für die Bewertung des Behandlungserfolgs bei künftigen Patienten mit Lebersteatose.

Abschließend nutzen wir darüber hinaus in einer weiteren Studie die optoakustische Mesoskopie mit Rasterabtastung (RSOM), um das Mikrogefäßsystem der Haut bei Patienten mit Diabetes abzubilden. Durch die Verwendung von grünem Licht (532 nm) konnten wir hochauflösende (7-10 µm) Bilder der Mikrovaskulatur der Haut bei gesunden Probanden und Patienten mit Diabetes erstellen, die auf der starken Präsenz von Hämoglobin in der Haut basieren. RSOM zeigte eine Verschlechterung der Hautmikrovaskulatur bei Diabetes, was sich in einer statistisch signifikant geringeren Anzahl von Gefäßen und einem geringeren Blutvolumen im Vergleich zur gesunden Gruppe äußerte. Unsere Ergebnisse lieferten wichtige Einblicke in die Mikroangiopathie bei Diabetes und zeigten einmal mehr das große Potenzial der RSOM-Technologie als Instrument für translationale Forschung und die künftige klinische Praxis. Insgesamt birgt die optoakustische Bildgebung ein erhebliches Potenzial für die Darstellung verschiedener Aspekte der Gewebephysiologie und ihrer Störung bei Krankheiten. Durch die Nutzung einzigartiger optoakustischer Merkmale und mithilfe von detaillierter Planung wie auch Durchführung zielen unsere Studien darauf ab, unser Verständnis verschiedener Erkrankungen wie Adipositas, nichtalkoholische Fettlebererkrankung (NAFLD) und Diabetes zu verbessern und die Behandlung dieser Patienten in Zukunft zu erleichtern.

I dedicate this to my parents (Panagiota and Pavlos), sister (Vicky), niece/godchild (Pavlina Valentina), and grandparents (Angelina and Nikos).

Publication and Submission Record

My work is a publication-based dissertation, which is based on three publications that are published in international journals (* indicates equal author contribution):

1. **NA Fasoula** *, A Karlas *, M Kallmayer, AB Milik, J Pelisek, HH Eckstein, M Klingenspor, and V Ntziachristos, "Multicompartmental non-invasive sensing of postprandial lipemia in humans with multispectral optoacoustic tomography", *Molecular Metabolism* 2021 May; 47: 101184.
2. **NA Fasoula** *, A Karlas *, O Prokopchuk, N Katsouli, M Bariotakis, E Liapis, A Goetz, M Kallmayer, J Reber, A Novotny, H Friess, M Ringelhan, R Schmid, HH Eckstein, S Hofmann, and V Ntziachristos, "Non-invasive multispectral optoacoustic tomography resolves intrahepatic lipids in patients with hepatic steatosis", *Photoacoustics*.2023 Feb; 29:100454.
3. H He*, **NA Fasoula** *, A Karlas, M Omar, J Aguirre, J Lutz, M Kallmayer, M Füchtenbusch, HH Eckstein, A Ziegler, and V Ntziachristos, "Opening a window to skin biomarkers for diabetes stage with optoacoustic mesoscopy", *Light: Science & Applications* 12 (1), 231 (2023).

The following publications that I have contributed to during my Ph.D. are relevant to this work but are not included in this dissertation as individual chapters:

4. A Karlas, **NA Fasoula**, K Paul-Yuan, J Reber, M Kallmayer, D Bozhko, M Seeger, HH Eckstein, M Wildgruber, and V Ntziachristos, "Cardiovascular optoacoustics: From mice to men - A review", *Photoacoustics*. 2019 Mar 29; 14:19-30.
5. M Kroenke, A Karlas, **N Fasoula**, N Markwardt, K Scheidhauer, M Eiber, W Weber, and V Ntziachristos, "Multispectral Optoacoustic Tomography: A Novel Label-Free Imaging Technique for the Assessment of hyperthyroid diseases", *Journal of Nuclear Medicine*, May 2019, 60 (supplement 1) 525.
6. A Karlas*, M Kallmayer*, **NA Fasoula**, E Liapis, M Bariotakis, M Krönke, M Anastasopoulou, J Reber, HH Eckstein, and V Ntziachristos, "Multispectral Optoacoustic Tomography of Muscle Perfusion and Oxygenation under Arterial and Venous Occlusion - A Human Pilot Study", *Journal of Biophotonics*, 2020 Mar 5: e201960169.

7. NK Chlis*, A Karlas*, **NA Fasoula**, M Kallmayer, HH Eckstein, FJ Theis, V Ntziachristos, and C.A Marr, "Sparse Deep Learning Approach for Automatic Segmentation of Human Vasculature in Multispectral Optoacoustic Tomography", *Photoacoustics*.2020 Dec; 20:100203.
8. A Karlas*, M Masthoff *, M Kallmayer, A Helfen, M Bariotakis, **NA Fasoula**, M Schäfers, M Seidensticker, HH Eckstein, V Ntziachristos, and M Wildgruber, "Multispectral optoacoustic tomography of peripheral arterial disease based on muscle hemoglobin gradients—a pilot clinical study", *Annals of Translational Medicine*. 2021 Jan; 9 (1): 36.
9. A Karlas*, M Kallmayer*, M Bariotakis, **NA Fasoula**, E Liapis, F Hyafil, J Pelisek, M Wildgruber, Eckstein HH, and V Ntziachristos, "Multispectral optoacoustic tomography of lipid and hemoglobin contrast in human carotid atherosclerosis", *Photoacoustics*.2021 Jul 9;23:100283. https://doi.org/10.1016/j.pacs.2021.100283
10. A Karlas, **NA Fasoula**, N Katsouli, M Kallmayer, S Sieber, S Schmidt, E Liapis, M Halle, H-H Eckstein, and V Ntziachristos, "Skeletal Muscle Optoacoustics Reveals Patterns of Circulatory Function and Oxygen Metabolism during Exercise", *Photoacoustics*. 2023 Apr; 30:100468.
11. PN Kampaktsis, M Emfietzoglou, A Al Shehhi, **NA Fasoula**, C Bakogiannis, D Mouselimis, A Tsarouchas, VP Vassilikos, M Kallmayer, HH Eckstein, L Hadjileontiadis, and A Karlas, "Artificial intelligence in atherosclerotic disease: Applications and trends", Front. Cardiovasc. Med., 19 January 2023. Volume 9 - 2022 | https://doi.org/10.3389/fcvm.2022.949454.
12. **NA Fasoula *,** Y Xie*, N Katsouli, M Reidl, MA Kallmayer, HH Eckstein, V Ntziachristos, L Hadjileontiadis, DV Avgerinos, A Briasoulis, G Siasos, K Hosseini, I Doulamis, PN Kampaktsis, and A Karlas, "Clinical and Translational Imaging and Sensing of Diabetic Microangiopathy: A Narrative Review", J. Cardiovasc. Dev. Dis. 2023, 10(9), 383; https://doi.org/10.3390/jcdd10090383.
13. A Karlas, **NA Fasoula**, M Kallmayer, C Schäffer, G Angelis, N Katsouli, M Reidl, F Dülmer, K Al Adem, L Hadjileontiadis, H-H Eckstein, and V Ntziachristos, "Optoacoustic Biomarkers of Lipids, Hemorrhage and Inflammation in Carotid Atherosclerosis", Front Cardiovasc Med. 2023 Nov 9;10:1210032. doi: 10.3389/fcvm.2023.1210032.

14. A Karlas*, N Katsouli*, **NA Fasoula**, M Bariotakis, NK Chlis, M Omar, H He, D Iakovakis, C Schäffer, M Kallmayer, M Füchtenbusch, A Ziegler, HH Eckstein, L Hadjileontiadis, and V Ntziachristos, "Dermal features derived from optoacoustic tomograms via machine learning correlate microangiopathy phenotypes with diabetes stage", Nat Biomed Eng. 4 December 2023. doi: 10.1038/s41551-023-01151-w. Epub ahead of print.

Abbreviations

	Description
1D	One-dimensional
2D	Two-dimensional
3D	Three spatial dimensions / Three-dimensional
4D	Fourth dimension
5D	Fifth dimension
6D	Sixth dimension
AI	Artificial Intelligence
BAT	Brown Adipose Tissue
BGR	Background Region
CCD	Charge-Coupled Device
CD	Chow Diet
CEUS	Contrast-Enhanced Ultrasound
CVD	Cardiovascular Disease
CT	Computed Tomography
DFU	Diabetic Foot Ulcer
DEXA	Dual-Energy X-ray Absorptiometry
DOT	Diffuse Optical Tomography
ED	Endothelial Dysfunction
FDG	^{18}F-Fluorodeoxyglucose
FMT	Fluorescence Molecular Tomography
FOV	Field Of View

Hb	Deoxygenated Hemoglobin
HbO_2	Oxygenated Hemoglobin
HCC	Hepatocellular Carcinoma
HDL	High-Density Lipoprotein
HDL-C	High-Density Lipoprotein-Cholesterol
HFD	High-Fat Diet
HSI	Hyperspectral Imaging
ICG	Indocyanine Green
IDL	Intermediate-Density Lipoprotein
LDF	Laser Doppler Flowmetry
LDI	Laser Doppler Imaging
LDL	Low-Density Lipoprotein
LSCI	Laser Speckle Contrast Imaging
IRT	Infrared Thermography
MiROM	Mid-infrared Optoacoustic Microscopy
MMPs	Matrix Metalloproteinases
MRI	Magnetic Resonance Imaging
MSOT	Multispectral Optoacoustic Tomography
NAFLD	Non-Alcoholic Fatty Liver Disease
NIR	Near-Infrared Region
OA	Optoacoustics
OAM	Optoacoustic Microscopy
OAT	Optoacoustic Tomography

OCT	Optical Coherence Tomography
PAT	Photoacoustic Tomography
PET	Positron Emission Tomography
PORH	Post-Occlusive Reactive Hyperemia
ROI	Region Of Interest
RSOM	Raster Scan Optoacoustic Mesoscopy
SAT	Subcutaneous Fat
SPPF	Single-Pulse-Per-Frame
TBV	Total Blood Volume
THb	Total Hemoglobin
US	Ultrasound
UT	Ultrasound Transducer
VAT	Visceral Adipose Tissue
VLDL	Very-Low-Density Lipoprotein
WAT	White Adipose Tissue

Contents

List of figures in chapter 1

1 | Introduction and Methodology

1.1 | Lipid metabolism in humans: A brief introduction

The term “lipids” refers to a group of diverse organic compounds, which includes fats, oils, phospholipids, waxes, and steroids. Lipids are crucial for the general homeostasis of the body, mainly by i) storing energy and regulating energy metabolism and ii) offering structural and functional support to the cellular membranes [1]. Thus, lipids, along with proteins and carbohydrates, belong to the most essential components of living cells. Nevertheless, apart from their significance at a cellular or microscale level, lipids are also crucial for the structure and function of the body at the macroscale. Lipids are mainly accumulated in specific cells, called adipocytes, which lie in many different positions throughout the body. Adipocytes contain fat globules in the form of triglycerides that occupy almost 90% of the total cell volume. Adipocytes are the main constituents of adipose or, alternatively, fat tissues. Adipose tissues offer protection and provide structural support to prevent injury and damage to essential organs in the human body, such as the spleen, liver, heart, and kidneys, among others [2].

The body is supplied with lipids mainly via food consumption (lipid digestion and absorption) or their *de novo* synthesis that takes place in the liver using glucose as substrate (Fig. 1.1). The digestion and absorption of lipids happen along the whole gastrointestinal tract. First, in the oral cavity, the mixing with saliva, the mechanical digestion, and the initial step of the enzymatic digestion, via the effect of lingual lipase, take place. Second, in the stomach, the enzymatic digestion continues mainly via the action gastric lipase – and a small amount of lingual lipase, which reaches the stomach with food/saliva – and the supporting effect of mixing and churning via the gastric peristaltic contractions. Third, and finally, in the small intestine, the lipids are emulsified by bile acids (produced in the liver and kept stored in the gallbladder), leading to the formation of small lipid globules from the breakdown of larger ones [3]. Emulsification is also enhanced by further enzymatic digestion through the activity of the pancreatic lipase so that, in the end, micelles are formed. Micelles are microscopic structures (< 10 nm in diameter) consisting of lipids and bile salts that are finally absorbed by specific epithelial cells of the small intestine and provide their lipid content so that chylomicrons are formed and enter the bloodstream [4].

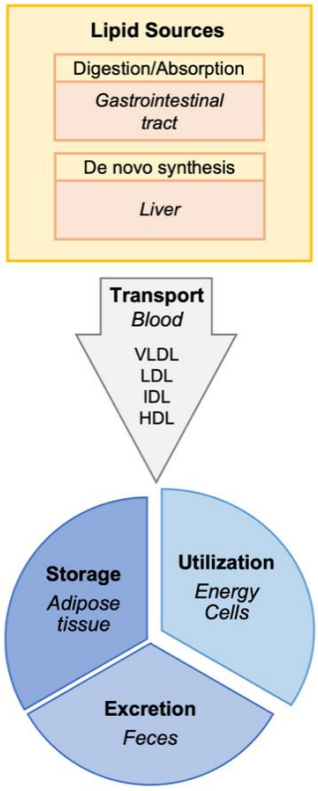

Fig. 1.1 | Overview of the main steps of lipid metabolism in humans. VLDL: very-low-density lipoprotein, LDL: low-density lipoprotein, IDL: intermediate-density lipoprotein, and HDL: high-density lipoprotein.

Lipids are blood-insoluble, so after entering the bloodstream, they soon react with/bind to proteins that are water- and blood-soluble. Consequently, lipids are transported in the form of lipoproteins in the blood. As also mentioned below, the lipoproteins (very-low-density lipoprotein/VLDL, high-density lipoprotein/HDL, low-density lipoprotein/LDL, and intermediate-density lipoprotein/IDL) are produced in the liver [5]. Even if there is always a relatively steady supply of lipids in the bloodstream, the lipid concentration changes over time. For example, it rises rapidly after ingesting a meal (postprandial lipemia) [2]. In any case, lipoproteins facilitate the transport of lipids to their destination organs to be used as energy sources (via oxidation), stored for later use, or even excreted from the body (e.g., in feces) [2]. In particular, lipid storage takes place when the body is not in acute need of energy and the form of triglycerides in adipose tissue [6].

Furthermore, apart from their digestion and absorption, lipids are produced *de novo* in the liver (lipogenesis) by converting excess glucose into fatty acids and triglycerides [7, 8]. The latter are then packaged into VLDL, released into the bloodstream, and transported to

adipose tissue for storage or muscle for energy. The HDL, another liver-produced lipoprotein, also plays a significant yet opposite role compared to the VLDL. It serves the removal of excess cholesterol from body tissues and transports them back to the liver to be metabolized and finally excreted [5]. In other words, the liver is an organ important for lipid metabolism or homeostasis since it is essentially involved in lipogenesis, lipid storage (either by facilitating their transport to adipose tissues or storing lipids in the form of triglycerides), lipid transport (via lipoproteins), lipid breakdown and production of bile acids [5]. Thus, the liver is responsible for providing the correct concentrations of lipids in the blood, ensuring their proper distribution throughout the body [6]. As a result, lipid metabolism remains in a continuous dynamic balance condition. The complexity of human lipid metabolism highlights its importance for general homeostasis. Indeed, dysregulation of any step of lipid metabolism leads to corresponding diseases, such as dyslipidemia, atherosclerosis, non-alcoholic fatty liver disease (NAFLD), obesity, and other significant diseases [9],[10]. Thus, in the next section (1.2), we provide further insights into the role of lipid metabolism and its dysregulation in relevant diseases, such as the ones belonging to metabolic syndrome.

1.2 | The role of lipids and adipose tissues in metabolic diseases

The metabolic syndrome is a group of several different and complex conditions that lead to metabolic dysregulation and known severe diseases, such as cardiovascular disease (e.g., coronary heart disease, stroke, peripheral arterial disease) and diabetes. The latter, along with other conditions, such as hypertension, dyslipidemia, and obesity, are not only possible "results" but also possible "causes" of metabolic syndrome, highlighting the complex associations and "vicious circle" character of relevant underlying conditions, overt diseases, and risk factors. Within the same framework, different risk factors, either modifiable (e.g., lifestyle factors, such as obesity, smoking, etc.) or non-modifiable (e.g., age, gender, race, family history), have an impact on the general metabolism and function of organs controlling it, leading, thus, to the development or acceleration of conditions mentioned above and diseases and, therefore, of metabolic syndrome [11].

In obesity, a persistent condition (more than 600 million adults are obese in the whole world), which is characterized by metabolic dysregulation, the disbalance between energy intake and expenditure is linked with excessive accumulation of adipose tissue and lipids in different tissues and organs [12]. In particular, the metabolism of several lipid types is affected. For example, triglycerides, VLDL, and small dense LDL are detected in increased levels in the bloodstream, while HDL-C is found to be decreased [13]. As a result, lipids accumulate in the liver, leading to liver steatosis/NAFLD, an initially benign condition, which, when left untreated, however, might not only lead to end-stage liver disease, hepatocellular carcinoma (HCC) but also increase the risk for other conditions, such as kidney disease or colorectal cancer [14]. Moreover, intramuscular lipid metabolism is also affected in subjects with obesity, where fatty acids enter the myocytes via the bloodstream but remain unoxidized in contrast to normal subjects, where increased intramuscular lipid oxidization drives their clearance via the capillaries [15, 16]. Excess intramuscular lipids seem to play an essential role in developing insulin resistance, thus consisting of a solid pathophysiological link among insulin resistance, obesity, and diabetes mellitus [17].

Diabetes is also associated with distorted lipid metabolism via the development of diabetic dyslipidemia, taking into account that the metabolism of glucose and lipids are highly interconnected via a common insulin-based regulation [18, 19]. As in obesity, serum triglycerides (also postprandially) and small dense LDL are elevated, while HDL-C is found to be decreased in patients with diabetes [18, 20]. The majority (> 75%) of patients with type 2 diabetes mellitus have diabetic dyslipidemia as well [20]. Of course, diabetic dyslipidemia is

one of the factors elevating the risk of developing cardiovascular disease in patients with diabetes.

Finally, not only in diabetes but also in obesity, the adipose tissues (the main lipid depots) are also affected, apart from other abovementioned metabolic tissues and organs. For example, in obesity, adipose tissue dysfunctions and this local dysfunction promote a generalized inflammatory condition via the dysregulation of several adipokines, a family of endocrine active proteins. It is this very adipose tissue dysfunction that is finally associated with an increased risk for cardiovascular disease [21]. Furthermore, the mentioned earlier chronic low-grade adipose tissue inflammation seems to affect insulin sensitivity and glucose tolerance and is associated with the development of diabetes [10],[22].

In any case, lipid metabolism dysregulation and adipose tissue dysfunction are pathophysiological hallmarks in obesity, diabetes, and cardiovascular disease: all components of the metabolic syndrome [23]. Thus, assessing these changes might give insights into disease mechanisms and possible future therapies. Imaging serves this goal, so several techniques have been developed and introduced. In the upcoming section (1.3), we provide a short overview of the imaging modalities used in everyday clinical practice in adipose tissue imaging while discussing the role of optoacoustic technologies in relevant applications.

1.3 | Clinical imaging of adipose tissues using non-invasive techniques

The primary goals of adipose tissue clinical imaging are i) the description of their morphology, ii) the characterization of their functional status and metabolism, and iii) the mapping of their distribution and quantity throughout the body [24-26]. The abovementioned goals are based on observations that not only the morphology but also the function/metabolism and spatial distribution/quantity of adipose tissues are distorted in relevant diseases [27-29], rendering imaging a convenient tool for understanding disease pathophysiology or improving diagnostics and therapy assessment. Furthermore, taking into account the common differentiation of human adipose tissues mainly into white fat (WAT) and brown fat (BAT) tissues, two tissues with frequently opposing and/or complementary sets of characteristics and roles in lipid and general metabolism [30], relevant imaging techniques of both adipose tissues may offer a plethora of image-based biomarkers for the precise definition of any disease-induced alterations. Current clinical methods include ultrasound (US), magnetic resonance imaging (MRI), computed tomography (CT), dual-energy x-ray absorptiometry (DEXA), and positron emission tomography (PET).

The US offers high portability and ease of use but lacks standardization by showing high dependency on the expertise of the examiner [31]. However, US has been used not only in white subcutaneous fat studies but also in abdominal WAT and BAT [contrast-enhanced US (CEUS)] studies [32-34]. The trade-off between resolution and penetration imposes resolutions of down to 0.3 mm if deep tissue imaging over several centimeters is needed [35]. MRI, in contrast with the US, is appropriate for whole-body imaging, offering the opportunity to assess all fat depots and different tissues/organs in the human body in a single examination. Typical MRI techniques offer resolutions of one to a few mm [36, 37]. Nevertheless, the long examination times (usually 30-45 min) and the need for specialized personnel and infrastructure hinder the dissemination of the technique, even if it does not employ ionizing radiation. MRI has been hired to image both WAT and BAT in health and metabolic diseases [38].

Apart from MRI, CT can also be used to quantify fat in tissues, organs, compartments, or even the whole body. CT is more convenient for the patient due to shorter examination times but comes with exposure to ionizing radiation. Furthermore, CT also offers high resolutions (< 1 mm) [39], even if it is less accurate and reproducible when it comes to the quantification of adipose tissues compared to MRI [40]. Even if CT has been employed in label-free WAT imaging (imaging of visceral adipose tissue, VAT) [40], BAT can only be visualized/detected

after the intravenous injection of a contrast agent [41]. The possible nephrotoxicity of such contrast agents, as well as the use of ionizing radiation, are two factors possibly hindering the use of CT for adipose tissue imaging in everyday practice.

In contrast to the abovementioned imaging techniques, which provide mainly structural/morphological information, PET gives insights into adipose tissue function/metabolism. For this reason, ^{18}F-Fluorodeoxyglucose (FDG)-PET is the technique of choice to image metabolically active adipose tissue, such as BAT [42]. Conventional PET, characterized by a spatial resolution of 4-5 mm, is usually combined with CT, which has a resolution of approximately 1 mm, to provide the user with complementary metabolic and anatomic imaging. However, newer PET scanners offer even higher resolutions, which are comparable to the ones provided by CT [43]. Even if PET is usually used to image BAT activity, studies using PET to image WAT have also been reported [44, 45].

Dual-energy x-ray absorptiometry (DEXA) has also been used for whole-body adipose tissue assessment [46]. DEXA is a relatively low-cost technique that is easily available and can be used to quantify fat throughout the body [47] without being able to differentiate between WAT and BAT [48]. DEXA is a two-dimensional (2D) modality employing ionizing radiation and, in particular, X-rays with two different energy levels, mainly to differentiate between bone and soft tissues [49]. DEXA scans generally expose the patient to much lower radiation levels compared to CT [50], and its readouts can also be translated into a “fat shadow” image (which has, however, a low resolution) for the whole human body [51].

Apart from the abovementioned techniques, usually used in everyday adipose tissue imaging, others have been used in relevant translational studies. For example, infrared thermography (IRT) has been used to image BAT activation in humans by measuring the temperature increase of the supraclavicular region, where the BAT lies, upon BAT activation [52, 53]. IRT takes advantage of the infrared radiation emitted at the wavelength range of (8–15 μm) by the human body to image tissue metabolism as reflected in local temperature changes. Even if it is low-cost, highly portable, and easy to use, IRT does not provide depth information while lacking standardization [52].

Optoacoustics, particularly multispectral optoacoustic tomography (MSOT, see sections 1.5 and 1.6), has been recently introduced as a powerful tool for human imaging of adipose tissues, both BAT and WAT [54]. By illuminating the body surface at several different wavelengths at the near-infrared region (NIR) (usually 680-980 nm or even 680-1300 nm for

the new systems), MSOT offers the opportunity to directly image lipids, the main constituent of adipose tissues, within the human body [55]. Lipids can be detected and visualized based on their light absorption spectrum at the NIR, characterized by a prominent absorption peak at 930 nm [56]. MSOT is now available in highly portable, hand-held systems that can be used in everyday practice, even at the bedside. For a more detailed description of MSOT technology, please refer to sections 1.5 and 1.6 and relevant studies (chapters 2 and 3). In this thesis, we demonstrate the incredible capabilities of MSOT to visualize lipids not only within the bloodstream ([57], chapter 2) but also within complex tissue parenchymata, such as the one of the human liver ([58], chapter 3), or else compartments/organs full of hemoglobin, a potent light absorber whose presence may well render the detection of other chromophores, such as the lipids, indeed challenging.

Furthermore, apart from MSOT, which is the optoacoustic technology with the highest translational potential at the moment, another technique, the so-called raster-scan optoacoustic mesoscopy (RSOM), has also been investigated as a powerful tool for imaging tissue changes induced in metabolic diseases. Usual RSOM implementations may not be real-time (45 s are needed for the acquisition of one image for the new systems) but provide the user with high-resolution (7-10 μm) images of the microvasculature by employing green (532 nm) light. In this work, we explore for the first time the capability of RSOM to deliver detailed images of the skin microarchitecture and its distortion in patients with diabetes ([59], chapter 4).

Thus, the current work, by combining both MSOT (macroscopy) and RSOM (mesoscopy), achieves the demonstration of the unique capability of optoacoustics: to provide not only a multi-aspect (by enabling the examination of several tissues/organs) but also a multi-scale (different resolutions and scales of detail) characterization of soft tissue physiology/metabolism and metabolic disease pathophysiology based on the same phenomenon and principle.

1.4 | Diabetes and skin microangiopathy

Diabetes develops in concert with metabolic abnormalities mirroring and causing changes in the vasculature. Persistently high blood glucose levels and insulin resistance damage the microvascular status of various target organs, such as the peripheral nerves (diabetic neuropathy). Diabetes is also connected to macrovascular diseases, such as coronary and peripheral arterial disease. Both the micro- (such as neuropathy) and macrovascular (such as atherosclerosis) complications of diabetes affect the skin, the body's largest and most easily accessible organ, which serves as both a protective barrier against external factors like mechanical, chemical, and thermal and a susceptible sensory organ. These complications lead to microvascular rarefaction, structural and functional changes in the skin's microvascular organization [59], such as endothelial dysfunction (ED), and reduction of the capillary density and size, resulting in inadequate tissue perfusion and thus in loss of its health and functional integrity. Especially in the lower extremities, diabetic complications may result in skin ulcerations, wound healing disorders, and even amputations [60]. However, in diabetes, these microvascular abnormalities often occur early in the disease [61] and before other complications become evident.

Diabetes-related dysfunctions and their significant impact on the quality of life illustrate the need to detect microvascular dysfunction in an early stage and diagnose patients with diabetes at risk. Skin microvascular changes and, specifically, skin microangiopathy caused by diabetes occur early in the course of the disease and before other serious complications manifest and serve as possible biomarkers for monitoring disease progression and severity, particularly concerning complications like diabetic foot ulcers (DFUs). To efficiently assess these changes non-invasively, several imaging and sensing technologies have been employed so far.

One such tool, capillaroscopy, uses digital cameras to capture high-resolution images of skin capillaries, with resolutions typically ranging from 1 to 6 µm per pixel. This technique has found extensive use in diabetes research. Capillaroscopy boasts numerous advantages, including its widespread availability, ease of use, and a high degree of repeatability and reliability [62]. However, it does not provide tomographic imaging of the skin's depth.

Laser Doppler flowmetry (LDF) and laser Doppler imaging (LDI) represent optical methods for monitoring skin microvascular perfusion. LDF provides one-dimensional (1D) skin perfusion measurements by illuminating the skin with laser light. LDF devices incorporate small sensors

applied directly to the skin, extracting real-time perfusion information over skin volumes of approximately one mm^3. LDI offers the ability to reach depths of around 1–2 mm and real-time imaging of skin perfusion with a spatial resolution of 1 µm. While both LDF and LDI rely on the Doppler effect and offer valuable insights into skin perfusion, it is essential to note that the information they provide is indirect, as they do not directly visualize the skin microvasculature at the single-vessel level. These techniques are frequently employed in functional tests, such as post-occlusive reactive hyperemia (PORH), thermal challenges, or iontophoresis tests. During these tests, the skin is stimulated through physical or chemical means, and its resulting hyperemic response is measured and evaluated as an indicator of its functional well-being. Studies have indicated that diabetes influences the hyperemic responses recorded by LDF and LDI [63].

Laser speckle contrast imaging (LSCI) commonly visualizes blood vessels, similar to LDI, by capturing intravascular blood flow information. LSCI employs a charge-coupled device (CCD) camera to detect the speckle pattern and subsequently relates it to a blood flow model to estimate blood flow. LSCI also uses near-infrared light, typically around 785 nm, allowing it to penetrate depths of approximately 300 µm. It has effectively differentiated ischemic and non-ischemic areas in patients with diabetes [64].

Hyperspectral imaging (HSI) operates by utilizing light across a range of wavelengths, typically between 400 and 1000 nm, [65] to capture multiple images of the same skin area. This process effectively records the spectrum of each pixel, allowing for the assignment of a 'tissue/molecular label' to each pixel by comparing its spectrum to established spectra of different tissues and molecules. Consequently, biomolecules such as HbO_2, Hb, and water [66] can be accurately distinguished at a resolution of 100 µm. Typically, hyperspectral cameras are positioned at a distance of 25 to 30 cm above the skin region under examination, maintaining the integrity of the skin's surface and perfusion due to their non-contact nature [67]. It has shown potential in assessing skin perfusion and oxygenation in diabetes and predicting DFU healing. Notably, HSI has revealed diminished perfusion and oxygenation in the skin of patients with diabetes [68].

In addition to its fundamental role in monitoring diabetic retinopathy, optical coherence tomography (OCT) proves to be a valuable tool for tracking skin microvasculature and its irregularities in individuals with diabetes. This technique enables the visualization and quantification of microvascular changes in the skin, shedding light on parameters like microvascular density, diameter, and flow rate [69].

A non-invasive optoacoustic imaging method, RSOM offers detailed cross-sectional images of the skin's layers. Operating with green light (532 nm), RSOM takes approximately 60 s to capture an image. This technique enables the distinction between epidermal and dermal layers and provides insight into various structures within the dermal papillary region and reticular dermis [70]. In particular, RSOM's ability to offer detailed images of skin microarchitecture and its correlation with diabetes severity through multiple biomarkers has been demonstrated [71].

These modalities are often combined with functional tests like post-occlusive reactive hyperemia (PORH), thermal stimuli, and iontophoresis to evaluate skin microvascular responses. This evolving field offers researchers and clinicians valuable tools for improving the management of diabetes-related microangiopathy.

In the next section (1.5), we will provide a more detailed description of the optoacoustic phenomenon and the standard technologies/imaging setups that employ it in biomedical applications.

1.5 | Optoacoustic phenomenon and imaging technologies

The term “optoacoustic” – also known as “photoacoustic” – phenomenon is used to describe a complex but well-defined chain of physical processes that lead to the conversion of electromagnetic energy in the form of light into mechanical energy in the form of acoustic/sound/pressure waves within an object, material, or biological tissue (Fig. 1.2). More specifically, the amplitude/intensity of the light, which is emitted into the tissue under examination, should fluctuate over time to induce the generation of sound waves. The light fluctuation might be either periodical or in the form of pulses. Current systems used in the biomedical field employ lasers, which provide light pulses as output. Each pulse, which is usually very short in duration (on the scale of 10^{-9} s), is emitted within the tissues, travels, and gets absorbed by them, causing a local meager increase of temperature and, thus, a thermo-elastic expansion. Considering that i) the light pulse, the temperature increase induced by the energy it carries, and the subsequent thermo-elastic expansion are very short/fast and ii) this sequence of events is rapidly repeated at rates of 25-100 Hz, the produced local vibrations and propagated sound waves are characterized by high frequencies which lie in the range of ultrasound. These ultrasound waves are detected by appropriate detectors and converted into voltage signals that are finally reconstructed into images. The molecules that absorb the light pulses based on their optical or optoacoustic properties are called chromophores and can be endogenous (e.g., hemoglobin) or exogenous (e.g., injected agents), as thoroughly discussed in section (1.7).

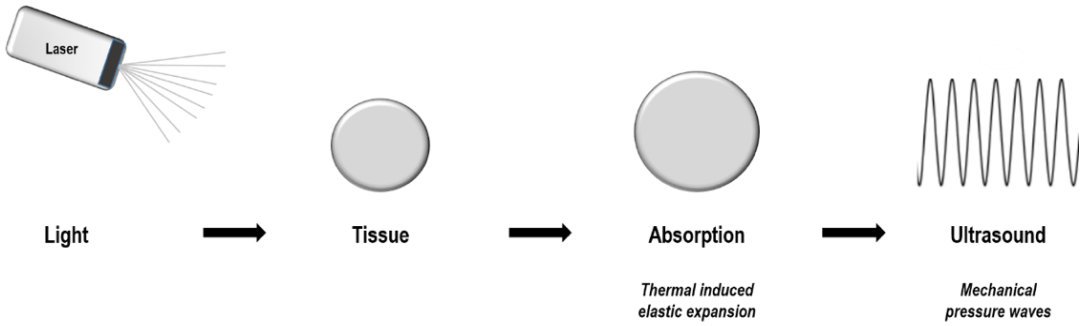

Fig. 1.2 | The optoacoustic or photoacoustic effect. The illumination of the tissue with light pulses results in light absorption by specific chromophores. With the absorption of light, a thermally-induced elastic expansion of the tissue is produced. The resulting local, fast, and transient “mechanical stress” leads to the production of ultrasound waves, which are finally recorded by tailored detectors and translated into images with specific algorithms.

The optoacoustic phenomenon is mathematically described by means of the equation below (Eq. 1.1), which refers to the optoacoustic pressure wave produced upon tissue illumination:

$$\left(\frac{1}{v_{ac}}\frac{\partial^2}{\partial t^2}-\nabla^2\right)P=\frac{\beta}{C_p}\frac{\partial}{\partial t}(\alpha I(\alpha)) \qquad \text{Eq. 1.1}$$

where ***P*** is defined as the pressure derived from the production of the optoacoustic wave, v_{ac} refers to the propagation speed of sound in tissue, ***β*** is volumetric thermal expansion coefficient that illustrates the changes induced tissue volume change as a result of a temperature change locally, C_p is the necessary thermal energy for the production of the expected local temperature change and $\alpha I(\alpha)$, where α is defined as the absorption coefficient of the light expressed in cm^{-1}, reflecting light absorption during the propagation in biological tissues.

The majority of the optoacoustic systems used for biomedical imaging and sensing applications operate a spectral range that is preferably in the visible or near-infrared spectral regions for the production of the acoustic waves that lie within the ultrasound region [72]. Light radiation transfers energy to the target material based primarily on its absorption spectrum.

Currently, there is a large variety of optoacoustic systems used for imaging biomedical applications that could be appropriately classified according to the spatial resolution and the penetration depth [73, 74]. For this reason, categories of systems (Fig. 1.3) based on the different spatial resolution and imaging depth are available. More specifically, there are microscopic (few μm resolution and less than 1 mm depth of imaging), mesoscopic (few tens of μm resolution and depth of imaging between 1 and 5 mm), and macroscopic systems (few tens to hundreds of μm resolution and more than 4 cm penetration depth). Due to this versatility, research could benefit from using the same principle to conduct imaging of anatomical and biological processes at the molecular level in three different scales: microscopic, mesoscopic, and macroscopic.

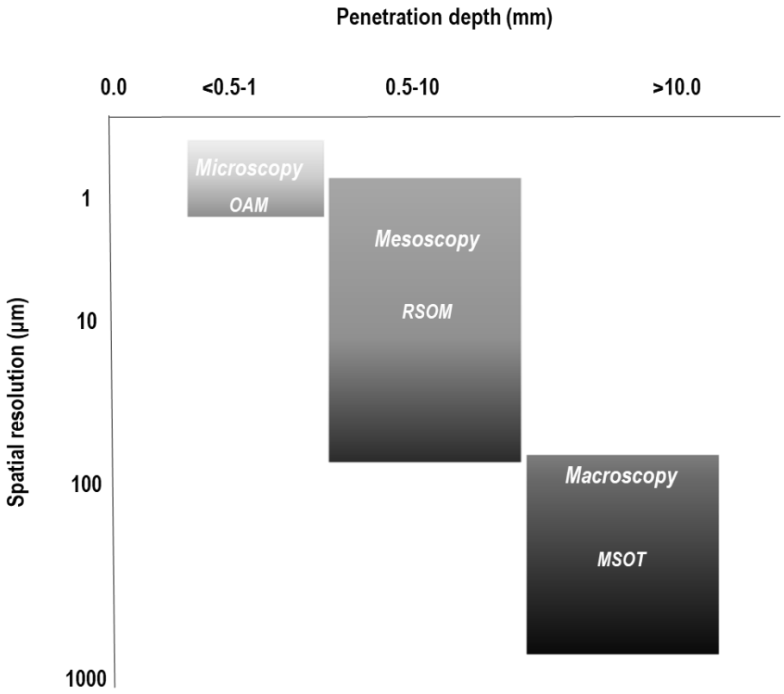

Fig. 1.3 | Common optoacoustic technologies. Categorization of techniques based on the optoacoustic phenomenon in accordance with penetration depth and spatial resolution. OAM refers to Optoacoustic Microscopy, RSOM to Raster Scan Optoacoustic Mesoscopy, and MSOT to Multispectral Optoacoustic Tomography.

Optoacoustic microscopy (OAM) has been implemented by means of numerous different setups. Their detailed description lies beyond the scope of the current thesis, which focuses on clinical optoacoustic applications for lipids and their metabolism in relevant diseases. Nevertheless, lipids have served as optoacoustic contrast sources in several studies, and thus, we provide herein some characteristic applications. For example, in [75], a newly developed technology named "mid-infrared optoacoustic microscopy (MiROM)" has been employed to image lipids along with proteins and carbohydrates in excised carotid plaque samples from patients who underwent carotid endarterectomy. By operating at the illumination range of 2932–2770 cm^{-1} and 1739–900 cm^{-1}, MiROM showed excellent capability in providing highly detailed intraplaque spatial maps (resolution of 2.5 µm) of the abovementioned molecules, offering label-free biochemical characterization of the samples. Also, in [76], the authors produced a plaque-mimicking biological phantom with excised human carotid plaque samples to be imaged by means of a customized system operating at the range of 500-1300 nm illumination wavelengths. Acquired data were then spectrally unmixed into comprehensive images/maps of lipids, methemoglobin, and collagen: all parameters associated with plaque instability and cause of events, such as stroke.

The primary representative of optoacoustic mesoscopic technologies is raster-scan optoacoustic mesoscopy (RSOM) (Fig. 1.4), achieving spatial resolution of about 7-10 µm. By offering this resolution, RSOM has already been implemented in various biomedical applications, such as microvascular skin imaging in health and disease (e.g., psoriasis) [77, 78].

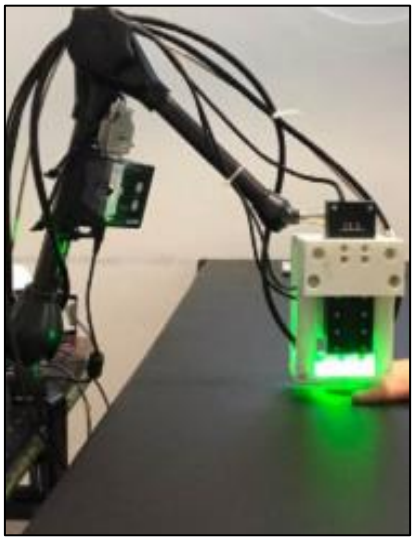

Fig. 1.4 | RSOM system. The RSOM system is designed for precise skin measurements. It comprises two fiber bundles for illumination, accompanied by a high-frequency ultrasound transducer that performs a raster scan across the skin's surface.

This optoacoustic imaging system has a specialized probe enabling precise two-dimensional visualization of microvessels. Designed for the detection of optoacoustic signals within human tissue, it achieves this by laser excitation. The laser emits low-energy pulses, measuring less than 3.75 µJ/mm² per pulse, well below the permissible limit of 20 mJ/cm² [79], with a concise duration of approximately five ns, and operates at a 1 kHz repetition rate. Each pulse corresponds to a wavelength spanning the visible to infrared light spectrum, ranging from 400 to 1400 nm. RSOM system possesses the capability to visualize the three-dimensional distribution of important biomolecules, including oxyhemoglobin, deoxyhemoglobin, water, and lipids, with high resolution around 20 µm laterally and 7 µm axially [71]. It achieves this remarkable precision even at depths of several millimeters within the tissue [80]. The body's endogenous biomolecules absorb laser pulses, inducing a brief and minimal tissue heating, leading to thermoelastic expansion at the molecular level and the generation of a slight pressure wave. This subtle pressure wave subsequently produces an ultrasound echo, detectable by an ultrasound sensor. The principle is based on directing

a laser pulse into the target tissue, yielding ultrasound generation that can be captured from the tissue. Subsequently, a computer processes this data to generate an image of the sound wave pattern, which undergoes distortion due to interactions with skin and microvessels.

In this technology, ultra-wideband transducers are employed to sense the ultrasound and, usually, monochromatic light source (e.g., the green light at 532 nm) to acquire volumetric images of the microvasculature of the whole tissue at depths of 1-2 mm (Fig. 1.5) [81]. Raw optoacoustic data is obtained by raster-scanning a small region of interest (ROI) over the skin (usually 2 x 4 mm^2). During the measurement, the monochromatic light source and the ultrasound transducer are moved mechanically over the examined area (commonly at steps of 10 μm), and ultrasound signals are recorded over multiple different predetermined measurement locations (one pulse of light per signal).

Ultimately, the final image is created by utilizing customized reconstruction algorithms that use the recorded signals as input to produce a volumetric image of the scanned region. Three-dimensional RSOM images were reconstructed over two frequency bands (10-40 MHz and 40-120 MHz). The reconstruction of low-frequency (LF) components (10-40 MHz) segmented larger vessels (40-150 μm), while in the high-frequency (HF) components (40-120 MHz), smaller vessels (<10-40 μm) are seen. The different-sized vessels are color-coded in the rendered RBG images (red channel: larger vessels, LF components; green channel: smaller vessels, HF components; blue channel: empty) so that finer vasculature is highlighted in the presence of larger vessels.

Current systems need less than a minute to acquire and produce an RSOM image, with newer implementations even faster [82]. Hence, RSOM emerges as an exceptional choice for rapid, label-free skin analysis in clinical settings.

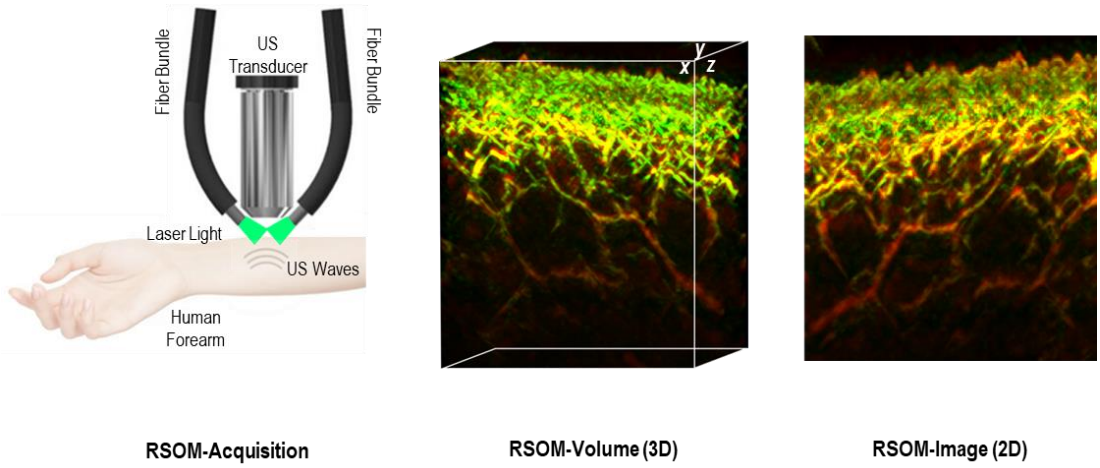

Fig. 1.5 | RSOM principle of operation. The RSOM system for skin measurements incorporates two fiber bundles for illumination and a high-frequency ultrasound transducer that raster scans over the skin surface. For every light pulse, several ultrasound waves are generated. These ultrasound signals are captured on the forearm of a healthy volunteer and then reconstructed to create a volumetric 3D RSOM image. The various colors denote different frequencies, with green representing high frequencies and red representing low frequencies. Finally, a tomographic 2D maximum intensity projection (MIP) along the Y-axis RSOM image is generated, with a scale bar indicating 500 µm.

Respectively, the most characteristic of the macroscopic optoacoustic imaging systems is the multispectral optoacoustic tomography (MSOT). MSOT is also known as optoacoustic or photoacoustic tomography (OAT, PAT). MSOT is closer to clinical translation than other optoacoustic imaging technologies. It has been used for imaging in both preclinical and clinical applications, giving potential possibilities for the conduction of translational studies [73, 83-85]. Current clinical systems are equipped with hand-held scanning probes with embedded illumination light sources operating at the NIR (see also section 1.3) and ultrasound detector arrays of hundreds of piezoelectric elements (e.g., n = 256 or 512). The spatial resolution of available systems ranges from 50-300 µm, and most of them operate in real-time with framerates of up to 100 Hz. MSOT takes advantage of the increased penetration depth of the near-infrared light in tissues to provide deep-tissue imaging (3-4 cm) of tissues with high optical contrast and ultrasound resolution. Hand-held probes include a wide variety of configurations, either two-dimensional (2D) arc-shaped (covering an angle of ≈140-170°) or three-dimensional hemisphere-shaped, which help the examination of different body regions. The capability of MSOT to transmit pulses of light at multiple different wavelengths (Fig. 1.6) allows the concurrent extraction of information about either endogenous (e.g., hemoglobin, lipids, water) or exogenous chromophores (e.g., injected contrast agents). Thus, interactions between various biological processes could be explored.

MSOT technology, known for its multidimensional role, is used more often in molecular imaging. Additionally, to the three spatial dimensions of width, height, and depth (3D) and the fourth dimension of time (4D), the MSOT technique records the spectral data of the scanned tissues, adding a new fifth dimension (5D). Moreover, further analysis in the frequency domain could provide different relative sizes of visualizations of the scanned objects, creating a new sixth dimension (6D) in an advanced way.

More specifically, the MSOT technique allows information extraction about different scales or orders of magnitude in the spatial domain. However, MSOT preserves robustness and its characteristics in both temporal and spectral domains. One of the significant limitations faced by all-optical imaging technologies is the limited penetration depth. MSOT technology overcomes this limitation by reaching a penetration depth of up to several centimeters, and it produces tomographic images of the illuminated volume.

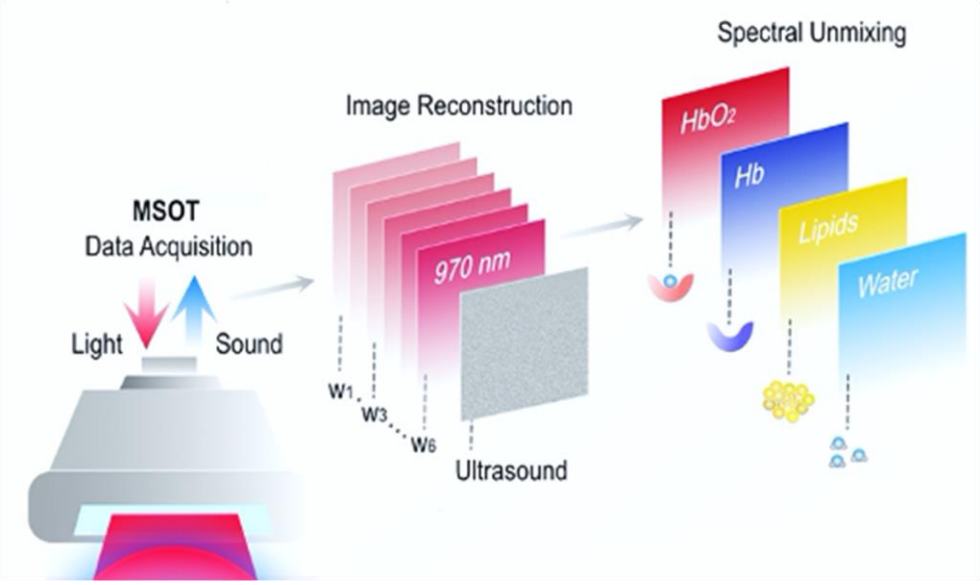

Fig. 1.6 | MSOT principle of operation. Pulses of light (indicated with red arrow), deriving from different wavelengths in the near-infrared region, illuminate tissue. Every light pulse is absorbed, and this process propagates the production of ultrasound waves (indicated with a blue arrow), which are finally reconstructed into an optoacoustic frame. For every optoacoustic frame, an ultrasound frame is recorded correspondingly. Eventually, all multispectral stacks of images recorded at different wavelengths are decomposed using the spectral unmixing step into images representing the spatial distribution of endogenous chromophores, such as the HbO_2 and Hb, lipids, and water.

In the work presented in the current thesis, MSOT was used to image lipids both in the bloodstream and within parenchymatous tissue, such as the human liver. Nevertheless, apart from MSOT, we have also employed RSOM to image the microvascular changes in the skin of

patients suffering from diabetes mellitus (Fig. 1.7), a common metabolic disorder, and its associated complications, including diabetic neuropathy as microvascular complication and atherosclerosis as macrovascular one compared to participants without diabetes [71].

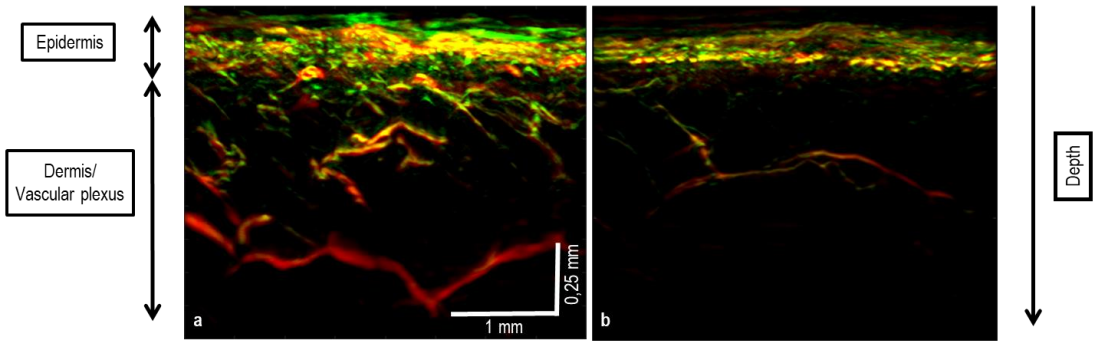

Fig. 1.7 | RSOM imaging of the skin microvasculature of the lower leg of healthy volunteers and patients with diabetes. a) Sectional MIP RSOM image of healthy skin of the lower extremity of a volunteer without diabetes, b) Sectional MIP RSOM image of skin from a patient diagnosed with type 2 diabetes mellitus. Scale bar = 500 µm.

In the following section (1.6), we will present a concise overview of the fundamental data processing workflow in clinical optoacoustics.

1.6 | Basic data processing workflow in clinical optoacoustics

Current data processing schemes for clinical optoacoustics are usually tailored to each technology. In general, the recorded ultrasound signals are first denoised, then reconstructed, and finally spectrally unmixed (in the case of multispectral imaging). The corresponding algorithmic development has been rushed over the last decades, allowing not only for real-time imaging but also real-time data processing, providing the user with a significant amount of information while scanning. For example, usual clinical MSOT systems, which operate with a single-pulse per frame principle (SPPF), "transform" the recorded voltage signals into tomographic images of the examined region with framerates of 25 Hz. As a reminder, the recorded voltage signals represent the sensed ultrasound waves by the ultrasound detectors (piezoelectric elements). Also, the sensed ultrasound waves represent the tissue absorption of light, as defined by the optoacoustic phenomenon. During scanning, for each laser pulse emitted and absorbed by the tissue chromophores, dozens of voltage/ultrasound signals are recorded, each corresponding to one ultrasound sensor (e.g., n=256 or 512, depending on the system). The recorded signals are reconstructed into images by means of dedicated reconstruction algorithms. Even if numerous different reconstruction algorithms have been developed [86], the major categories are the back-projection and model-based ones [72, 87, 88]. Back-projection reconstruction implementations may well be executed in real-time and, for this reason, are usually embedded in current MSOT systems to enable real-time imaging.

On the contrary, available model-based reconstruction implementations are generally slower than the back-projection ones, allowing only for their "offline" application on the acquired data. As already mentioned, one planar MSOT image is generated for every wavelength or illumination pulse after the reconstruction of the recorded signals. The sequence of the selected wavelengths (e.g., 28 wavelengths from 700 to 970 nm at steps of 10 nm) is repeated periodically during every MSOT measurement. Thus, for every group (e.g., 28) of illumination wavelengths, a "multispectral stack" consisting of a group of single-wavelength images is produced (Fig. 1.6). As a next step, each multispectral stack is used as an input for the process of spectral unmixing, or else the decomposition of the measured spectrum for each image/stack pixel into the previously defined spectrum endmembers, which are the known absorption spectra of endogenous chromophores (e.g., Hb, HbO_2, lipids, water, collagen) or injected dyes. Usually, the process of spectral unmixing occurs on a per-pixel basis. As a result, a new set of images is produced (e.g., five images for five different

endmembers/chromophores), where each pixel's intensity depends on the spectral signature and abundance of the known endmember spectrum in the measured absorption spectrum. As for the reconstruction step, several spectral unmixing techniques have been developed, with the majority of them allowing for only “offline” use [56, 89-91].

Nevertheless, current MSOT systems provide the option to achieve real-time hemoglobin unmixing (unmixing between Hb and HbO_2) during scanning. Of course, several data processing methods ranging from denoising schemes to motion and fluence correction algorithms have been developed [86, 92]. Available methods may act on the recorded ultrasound/voltage signals of the reconstructed or unmixed images. The absolute goal of all methods is the image quality and spectral unmixing improvement to further boost MSOT towards a more “quantitative” approach and, thus, its clinical translation.

As discussed, data processing schemes depend on system/data features. Thus, based on the fact that RSOM follows a non-real-time principle of operation with the usual RSOM systems being single-wavelength and offering superficial imaging (1-2 mm), RSOM data processing approaches focus mainly on denoising or motion correction aiming at improving image quality [93]. For example, in our pilot study, where the skin of patients with diabetes and the skin of participants without diabetes are examined using RSOM, a tailored motion correction algorithm was applied to the recorded RSOM data to enable the accurate extraction of skin microvascular features, such as the number and density of small vessels within the dermis [71]: features that seem to be diminished in diabetes leading probably to complications, such as skin ischemia and chronic ulcerations. Independently from the data processing schemes applied, optoacoustic imaging quality relies mainly on the spatial distribution of the sources of optoacoustic contrast, or else chromophores, employed.

In the subsequent section (1.7), we are going to provide a brief overview of the main sources of optoacoustic contrast for preclinical and clinical applications.

1.7 | Endogenous and exogenous sources of optoacoustic contrast

On the one hand, there are plenty of exogenous contrast agents that are already used in various preclinical or clinical optoacoustic applications [94]. For example, in [95], the authors incubated human carotid plaques for one hour with a contrast agent named MMPSense™ 680, a commercially available dye that binds to matrix metalloproteinases (MMPs), enzymes involved in inflammatory processes. By illuminating the excised and incubated plaques with light at the NIR (635-675 nm), the authors revealed not only morphological characteristics of the plaques but also achieved spatially-coregistered visualization of MMP-based inflammation: a feature showing plaque instability and increased risk for stroke [96]. Apart from ex vivo imaging of samples, exogenous contrast agents may well be injected in animal models to gain insights into disease pathophysiology. In [97], croconaine-based nanoparticles were intravenously injected in mice to explore the possibility of offering better diagnostics or image-guided surgery of brain tumors.

Moreover, it has been shown that MSOT is able to provide simultaneous imaging of both exogenous (e.g., apoptosis-targeting dyes) and endogenous (e.g., hemoglobin) contrast agents, providing in this way multi-aspect investigations of complex disease pathophysiology, such as the one of breast cancer [83]. In the clinic, indocyanine green (ICG), a fluorescent dye approved for human use, has been shown to have beneficial optoacoustic properties in several studies. ICG is usually injected intravenously, remains in the vascular bed for 3-5 min, allowing for imaging of the vasculature, and then seems to accumulate into inflammatory cells (e.g., macrophages) serving this way as an inflammation marker [73].

On the other hand, the strong presence of endogenous chromophores in biological tissues enables non-invasive and label-free anatomic, functional, and molecular imaging using MSOT [73]. The main endogenous light absorbers in human tissues are the oxy- and deoxyhemoglobins (HbO_2 and Hb), the lipids, and the water. Each light-absorbing molecule has a representative absorption spectrum at the NIR (Fig. 1.8), as measured and validated in the laboratory in previous experiments.

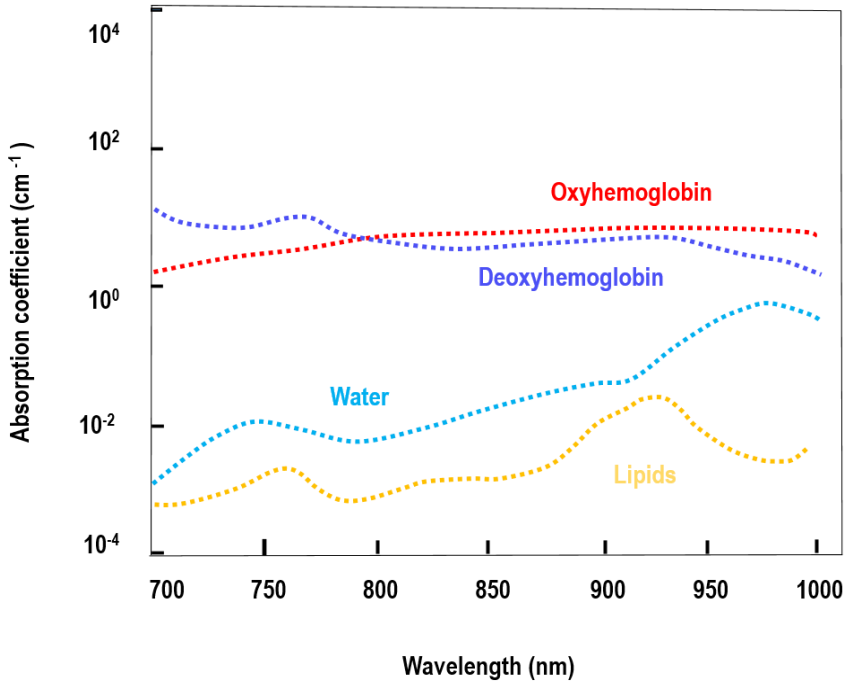

Fig. 1.8 | The primary endogenous chromophores and their absorption spectra in the NIR using MSOT technology. Both oxy- and deoxygenated hemoglobin (HbO_2 and Hb) remain the main light absorbers at the NIR despite the peak absorption of lipids at around 930 nm and the peak absorption of water at the 970 nm correspondingly. However, the measured spectra have a significantly different morphology, which facilitates the identification and unmixing (decomposition) of the multiple absorbers during the procedure of spectral unmixing.

The spectra of main endogenous chromophores in the NIR between 680-980 nm are of great importance. This very NIR represents the first optical window where the light penetrates deeper (3-4 cm) in tissue compared to the visible spectral region. As shown in the figure above (1.8), there are specific features of the chromophore spectra that enable their differentiation. In general, MSOT images acquired at 750 nm are considered more characteristic for the spatial distribution of Hb since at 750 nm, the absorption of Hb is higher than that of HbO_2. In analogy, MSOT images corresponding to the 850 nm are considered characteristic of the intratissue distribution of HbO_2.

Furthermore, the 'isosbestic point' of Hb and HbO_2, or else the wavelength where the NIR absorptions of HbO_2 and Hb are equal (800 nm), represents the distribution of the total hemoglobin (THb) within the examined tissues. Considering that hemoglobin is abundant in human tissues, MSOT images at 800 nm are considered to be representative of tissue morphology/anatomy. In other words, MSOT images at 750 nm, 800 nm, and 850 nm are

usually used in applications investigating the perfusion and oxygenation of blood and soft tissues, such as skeletal muscle and tumors [84, 98, 99].

Similarly, images acquired with MSOT at 970 nm correspond to tissue water content. For this reason, 970 nm-MSOT images are ideal for imaging the anatomy of high-water content tissues, such as the skeletal muscle [73]. Finally, the absorption of lipids is high at 930 nm, and thus, MSOT images recorded at 930 nm are typically used to represent lipids/fat. Based on this characteristic spectrum, lipids have been imaged in different applications with clinical relevance. For example, Karlas et al. demonstrated the capability of MSOT to differentiate between the liked and the lipid-rich plaque tissue in patients with carotid atherosclerosis.

1.8 | Limitations of optoacoustic imaging techniques

Clinical optoacoustic imaging does not come without limitations. First, the systems used in clinical research have a limited field of view (FOV). For example, current macroscopic tomographic systems, such as MSOT, are characterized by a FOV of 1-4 cm. This feature, in combination with the second limitation of the small penetration depth (1-4 cm depending on tissue type and system configuration), highlights a major drawback of such technologies, which only allows imaging of small regions of the body and superficial structures. Of course, by developing image stitching algorithms that can combine different FOVs acquired during an examination, larger areas of the body can be scanned and assessed with a single scan [100]. Regarding the limited penetration depth, even if it seems to be extraordinarily good compared to purely optical imaging technologies (effective imaging depths of several mm because of light scattering), it is still poor compared to other imaging techniques used in the clinics, such as CT and MRI (whole-body imaging). Despite this disadvantage, the use of optoacoustics in applications involving shallow tissues, such as the subcutaneous fat, and selected patients (e.g., non-obese patients) can still provide invaluable information for physiology studies and future disease diagnostics.

The generated ultrasound signals absorb light into tissue, traveling in all possible directions in 3D space. So, a detector, ideally in the shape of a sphere, should collect all signals that are produced by a particular object or source that absorbs light and give all the required information to the already used reconstruction algorithm. Nevertheless, in daily practice, the detector arrays used are more flexible and easier to use for practical reasons, on the one hand, limiting the input that is recorded and, on the other hand, decreasing the quality of the reconstructed data.

As mentioned, the illumination at several multiple wavelengths to achieve high quality of the spectra and increase the accuracy of the spectral unmixing process extends the duration of every multispectral stack, raising the possibility that the final product would be susceptible to motion artifacts. Specifically, the spectral unmixing step that takes place on a per-pixel basis is prone to motion artifacts deriving from exogenous and endogenous sources. For instance, motion from the breathing and heart, motion resulting from the vascular pulsation, various movements of patients occurring randomly, and quick movements of the expert MSOT operator’s hand can provoke apparent errors, especially in the spectral unmixing process. For this reason, specific MSOT scanning methodologies need to be defined

according to the anatomical region or application, and therefore development of schemes for correction of the motion is required.

Moreover, the currently used spectral unmixing methods rely on already-known spectra of specific chromophores, as measured under controlled conditions in the laboratory, to assign a chromophore signature to every pixel belonging to the unmixed image. However, the various phenomena characterizing the interaction between light and different tissue types (e.g., scattering and absorption) distort the perfectly defined laboratory-measured spectrum with increasing depth. This fact means that the whole process of spectral unmixing can be further challenging at increasing depths due to the “spectral coloring” phenomenon. Many advanced methods have been used in animal models in order to address this issue [101].

Nevertheless, although optoacoustic imaging is characterized by several limitations, its unique properties enable the visualization of different aspects of tissue physiology and disease pathophysiology. Thus, optoacoustics is of immense interest and utility not only for applied researchers and engineers but also for clinicians, promising a captivating and valuable field with a bright future ahead. In particular, optoacoustics of tissue metabolism and metabolic diseases has shown fast progress over the last years and is expected to develop further, aiming at entering the clinical practice and improving the diagnostics of future patients with relevant diseases.

2 | Multicompartmental non-invasive sensing of postprandial lipemia in humans with multispectral optoacoustic tomography

2.1 | Summary

The paper "Multicompartmental non-invasive sensing of postprandial lipemia in humans with multispectral optoacoustic tomography" is authored by Nikolina-Alexia Fasoula, Angelos Karlas, Michael Kallmayer, Anamaria Beatrice Milik, Jaroslav Pelisek, Hans-Henning Eckstein, Martin Klingenspor and Vasilis Ntziachristos. The version herein (Appendix A) is published in the *Molecular Metabolism* Journal.

Abnormal blood lipid profiles following food consumption have been linked to an increased risk for various cardiovascular and metabolic diseases. Currently, the current gold standard method for assessing lipid profiles involves frequent blood sampling over several hours after a meal. However, this approach is invasive and inconvenient for the examined subjects. To tackle this, non-invasive imaging techniques could provide a more convenient and direct means of monitoring postprandial lipemia in humans. In this study, we propose the use of multispectral optoacoustic tomography (MSOT) for imaging postprandial lipemia within the human vasculature and soft tissues, offering an alternative to invasive methods. In this pilot study, we employed a hand-held hybrid MSOT-Ultrasound (US) device to measure the postprandial response in four (N=4) healthy volunteers. Each subject underwent multiple scans using a hand-held hybrid MSOT-US device over a six-hour period following the oral consumption of a high-fat meal. We focused our measurements on four anatomical structures: the subcutaneous fat, the brachioradialis muscle, the cephalic vein, and the radial artery of the forearm. The tissues were illuminated using 28 different wavelengths in the near-infrared range. Our analysis specifically focused on the 930 nm, which exhibits the highest optoacoustic signal absorption by lipids. To accurately assess the changes in lipid content, regions of interest were identified under ultrasound guidance. This step allowed for delineating cross-sections of blood vessels, muscles, and subcutaneous fat regions. The lipid content was then calculated and plotted over time for each of these regions, providing a comprehensive multicompartmental analysis of postprandial lipemia. The results obtained from MSOT revealed an average approximate 1.5-fold increase in arterial lipids around 4 hours postprandially.

Additionally, there was a roughly 2-fold increase in venous lipids observed at 3 hours. We also observed an approximately 2-fold increase in muscle lipids detected after 3 hours and a roughly 1.5-fold increase in subcutaneous fat lipids observed around 4 hours following oral food intake. All changes were calculated with reference to a baseline measurement established for each subject, taking into account possible inter-individual variations. Our results demonstrate the remarkable capability of MSOT in providing non-invasive visualizations of lipid level fluctuations over time during postprandial tests, eliminating the need for contrast agents. Finally, by simultaneously imaging blood vessels and soft tissues, MSOT shows potential as a tool to explore probable "metabolic" interactions among different tissue types in future translational studies on cardiovascular and metabolic diseases.

Contribution:

NAF designed the study, performed the experiments, and wrote the manuscript.

2.2 | Publication

NA Fasoula*, A Karlas*, M Kallmayer, AB Milik, J Pelisek, HH Eckstein, M Klingenspor, and V Ntziachristos, "Multicompartmental non-invasive sensing of postprandial lipemia in humans with multispectral optoacoustic tomography", *Molecular Metabolism*, vol. 47, 2021 May; 101184.

3 | Non-invasive multispectral optoacoustic tomography resolves intrahepatic lipids in patients with hepatic steatosis

3.1 | Summary

The paper "Non-invasive multispectral optoacoustic tomography resolves intrahepatic lipids in patients with hepatic steatosis" is authored by Nikolina-Alexia Fasoula, Angelos Karlas, Olga Prokopchuk, Nikoletta Katsouli, Michail Bariotakis, Evangelos Liapis, Anna Goetz, Michael Kallmayer, Josefine Reber, Alexander Novotny, Helmut Friess, Marc Ringelhan, Roland Schmid, Hans-Henning Eckstein, Susanna Hofmann, and Vasilis Ntziachristos. The version herein (Appendix B) is published in the *Photoacoustics* Journal.

Hepatic steatosis is commonly benign and reversible during its early stages. However, if left undetected and untreated, it can progress to irreversible liver failure. Several non-invasive imaging techniques have already been employed to assess hepatic steatosis. However, currently available methods often lack direct molecular information and typically rely on contrast agents or bulky equipment. A promising alternative is multispectral optoacoustic tomography (MSOT), which enables the generation of tomographic images depicting the spatial distribution of lipids, solely relying on their characteristic light absorption at 930 nm. In this study, we demonstrate the effectiveness of MSOT in conjunction with a newly developed common analysis framework for detecting lipids in both mice and humans with and without hepatic steatosis**.** To induce obesity and hepatic steatosis, a group of n_1 = 5 B6 (Cg)-Tyr^{c-2J}/J mice was fed a high-fat diet (HFD), while an age-matched cohort of n_2 = 5 B6 (Cg)-Tyr^{c-2J}/J mice was kept on regular chow (CD) diet.

Additionally, n_3 =5 patients with previously diagnosed hepatic steatosis and n_4 = 5 healthy volunteers were included in the study. For each image, three distinct regions of interest (ROIs) were selected: i) the liver region, ii) the subcutaneous fat (SAT) region, and iii) the entire imaged tissue region. The third ROI included both the liver and SAT areas and was identified as the “background region” (BGR) for every image. Considering this, we derived a “normalized ratio spectrum” for each image/subject by plotting the normalized ROI/BGR ratios for the measured wavelengths. We then compared the mean of the ROI/BGR ratio at 930 nm, where lipids exhibit high absorption, between the two groups in both mice and humans. Our approach identified statistically significant differences between healthy and

diseased subjects based on MSOT-extracted spectral and intensity information. Specifically, we detected the characteristic near-infrared spectrum of lipids (prominent peak at 930 nm) within the liver region in diseased subjects (either mice or humans). The same peak was also detected in the corresponding subcutaneous fat regions, yet in both health and disease, as expected. This study represents the first known attempt to detect liver steatosis in both mice and humans based on a common and interplatform imaging and analysis framework, offering a unified translational solution that could aid in the detection and monitoring of the disease in both preclinical research and clinical settings.

Contribution:

NAF: Conceptualization, Methodology, Formal analysis, Investigation, Writing – original draft.

3.2 | Publication

NA Fasoula*, A Karlas*, O Prokopchuk, N Katsouli, M Bariotakis, E Liapis, A Goetz, M Kallmayer, J Reber, A Novotny, H Friess, M Ringelhan, R Schmid, HH Eckstein, S Hofmann, and V Ntziachristos, "Non-invasive multispectral optoacoustic tomography resolves intrahepatic lipids in patients with hepatic steatosis", *Photoacoustics*, vol. 29, 2023 February, 100454.

4 | Opening a window to skin biomarkers for diabetes stage with optoacoustic mesoscopy

4.1 | Summary

The paper "Opening a window to skin biomarkers for diabetes stage with optoacoustic mesoscopy" is authored by Hailong He, Nikolina-Alexia Fasoula, Angelos Karlas, Murad Omar, Juan Aguirre, Jessica Lutz, Michael Kallmayer, Martin Füchtenbusch, Hans-Henning Eckstein, Annete Ziegler, and Vasilis Ntziachristos. The version herein (Appendix C) is published in the *Light: Science and Application* Journal.

Diabetes-related complications, including diabetic neuropathy and atherosclerosis, are linked to the deterioration of the microvasculature in the skin. This fact highlights the importance of early detection of microvascular changes to identify patients at risk. By employing advanced imaging techniques to examine skin structure and microvasculature, we may be able to pinpoint sensitive metrics that can track not only the beginning and progression of diabetes but also its associated complications. Raster-scan optoacoustic mesoscopy (RSOM) offers unique capabilities for non-invasive imaging of skin microvasculature. In our study, we utilized the RSOM system to image the skin on the lower extremities over the distal pretibial region of 95 patients with diabetes and 48 healthy volunteers. To analyze the features extracted from the RSOM images in both participants with and without diabetes, we developed a new data processing pipeline that enables the automatic derivation of several metrics based on pathophysiological skin features and microvasculature within the dermis layer. In this pilot study, we present the possible correlations of label-free biomarkers extracted from RSOM images with the impact of both microvascular (neuropathy) and macrovascular (systemic atherosclerosis) diabetic complications on changes in skin microvasculature compared to participants without diabetes. Our findings demonstrated that biomarkers, such as skin epidermis thickness, blood volume, and vessel number, could significantly differentiate patients with diabetes and participants without diabetes.

Furthermore, our investigation unveiled statistically significant variations in these metrics among patients with varying degrees of severity of diabetic neuropathy and systemic atherosclerosis. In essence, the comprehensive RSOM imaging of all skin layers and their microvasculature can facilitate precise analysis of skin microanatomy and vasculature. This

approach may reveal novel quantitative biomarkers of the disease, offering a non-invasive and convenient means of diagnosis.

Contribution:

N.-A.F. designed the study, recruited the participants with and without diabetes, performed the experiments, collected the data, interpreted the results, and wrote the paper.

4.2 | Publication

H He*, **NA Fasoula***, A Karlas, M Omar, J Aguirre, J Lutz, M Kallmayer, M Füchtenbusch, HH Eckstein, A Ziegler, and V Ntziachristos, "Opening a window to skin biomarkers for diabetes stage with optoacoustic mesoscopy", *Light: Science & Applications* 12 (1), 231 (2023).

5 | Conclusions

5.1 | Conclusion and Outlook

In conclusion, the current studies presented different but interrelated examples highlighting the unique opportunity of imaging using optoacoustics to provide imaging of blood and lipids in health and disease. Our results display the exceptional potential of optoacoustics to provide imaging not only under static (e.g., hepatic steatosis, diabetes) but also dynamic (e.g., postprandial lipemia) conditions, opening up new possibilities for translational research and future clinical diagnostics for different metabolic diseases, such as obesity, non-alcoholic fatty liver disease, diabetes, and metabolic syndrome.

In **Chapter 1**, a comprehensive introduction is provided that includes the metabolism of lipids in humans, the role of lipids and adipose tissues in metabolic disorders, as well as a brief overview of the current techniques used for non-invasive imaging of adipose tissues. Moreover, a summary is included regarding diabetic microangiopathy of the skin and the modalities employed for its evaluation. Furthermore, we offered a thorough description of the optoacoustic phenomenon and available optoacoustic technologies/setups, as well as the steps followed in usual data processing schemes to achieve non-invasive and label-free imaging. The great capability of RSOM to provide detailed optoacoustic mesoscopy images of skin microvasculature is mentioned as well. Nevertheless, a short discussion regarding the main sources of optoacoustic contrast for preclinical and clinical applications is also included in this chapter. Finally, in **Chapter 1**, we thoroughly discuss the limitations of clinical optoacoustic imaging.

In the following chapter (**Chapter 2**), we examine the possibility of imaging postprandial lipemia in humans. To this end, we employed MSOT in an attempt to image the increase of triglyceride-rich lipoproteins in circulation following the consumption of fatty food. Typically, individuals eat three or more meals per day, each containing 20-70 g of fat [102], so that they spend approximately 18 hours a day in the postprandial state, at least concerning dietary fat metabolism. High blood lipid levels at the fasting or postprandial (non-fasting) state have been associated with an increased risk of developing cardiovascular (CVD) or metabolic diseases [103] [104], including obesity, hepatic steatosis, and diabetes. Thus, in this study, a high-fat meal was consumed in an attempt to simulate a typical Western diet meal. In this

work, clinical MSOT readouts showcase the great potential of the technology to be used as a non-invasive molecular imaging technique for the visualization of postprandial lipid fluctuations in blood vessels (radial artery and cephalic vein) and soft tissues (brachioradialis muscle and subcutaneous fat of the forearm). Our results showed that MSOT could accurately detect postprandial lipid dynamics in blood vessels and soft tissues non-invasively and without the need for contrast agents. Thus, MSOT provides the potential to study lipid metabolism under functional tests, offering another arrow in the quiver of both the translational and clinical researchers that could lead to novel diagnostic and prevention strategies.

Going one step further (**Chapter 3**), we explore the utility of MSOT as a label-free method for detecting the intrahepatic lipid content in healthy volunteers and patients with hepatic steatosis. To this end, we analyzed the spectral region around 930 nm, known for its distinctive lipid absorption properties. In its initial phases, hepatic steatosis is often benign and reversible. Nevertheless, if left unnoticed and unaddressed, it may advance to irreversible liver failure. While several non-invasive imaging techniques are available to assess hepatic steatosis, current methods frequently need more direct molecular information, relying on contrast agents or unwieldy equipment [105]. In this preliminary study, we applied MSOT to assess the liver and surrounding tissues of five patients with already diagnosed hepatic steatosis and five healthy volunteers. Our findings revealed significantly higher absorption levels at 930 nm in the liver of patients compared to healthy volunteers. At the same time, no notable differences were observed in subcutaneous adipose tissue between the two groups. To further support our findings in humans, we conducted corresponding MSOT measurements in mice subjected to a high-fat diet (HFD) and those on a regular chow diet (CD). The results of this preclinical sub-study confirmed our findings in humans. This study introduces MSOT as a promising non-invasive and portable technique for detecting and monitoring hepatic steatosis in both preclinical and clinical settings. The encouraging results presented here warrant further exploration through larger-scale studies.

In the last step and specifically in **Chapter 4**, we explore the capability of RSOM as a non-invasive and label-free technique for evaluating cutaneous changes in microvasculature in participants with and without diabetes. Diabetes mellitus impacts the microvasculature of various organs, including the skin, which provides the opportunity to detect diabetes-related systemic effects on the microvasculature [59]. However, traditional methods for assessing skin microvasculature, such as histological analysis, are not well-suited for disease

monitoring or application to large populations. To address this issue, we introduce RSOM as a tool in diabetes healthcare for assessing diabetes-related changes in dermal microvasculature and skin micro-anatomy and characterizing disease complications. We measured the pretibial region on the lower extremities of participants diagnosed with diabetes and healthy volunteers. We unveiled the relationship between RSOM-extracted biomarkers and the severity of the diabetes, as reflected in the presence of relevant vascular complications. These biomarkers encompassed the total number of microvessels and blood volume in the dermal layer, the epidermal thickness, and the optoacoustic signal density. This pilot study demonstrates the potential of RSOM as a promising point-of-care device for quantifying diabetes-related complications and offering an image-based indicator that could reflect the stage of the disease.

Thus, our work showcases the great capability of optoacoustic imaging for monitoring lipid fluctuations in human blood vessels and soft tissues following fatty food consumption over time, detecting hepatic steatosis in both mice and humans, and sensing the skin microangiopathy in patients with diabetes, rendering optoacoustics an ideal tool for preclinical and clinical metabolic applications.

In the future, our goal is to harness multispectral RSOM imaging to precisely quantify alterations in both oxygenated and deoxygenated hemoglobin. This approach would allow us to extract valuable insights into skin metabolism and oxygenation. Such measurements hold the potential to elucidate the underlying pathophysiology of chronic wounds, ultimately offering a means to predict and mitigate impaired wound-healing processes in individuals with diabetes mellitus. On the other hand, this idea can alleviate the significant economic burden and enhance the overall quality of life for those affected.

The next logical step involves conducting comprehensive preclinical and clinical studies to thoroughly evaluate the reproducibility of the measurements and implement a robust quality control mechanism. These studies would encompass metabolic studies focused on specific organs, such as skeletal muscle and adipose tissues, and their metabolism. Moreover, the substantial amount of acquired optoacoustic data necessitates an extended analysis period. To address this time-consuming challenge, continued progress in software development, probably along with artificial intelligence (AI) techniques, could facilitate the conduction of longitudinal preclinical and clinical studies in the spectrum of metabolic syndrome, including diseases such as diabetes mellitus, obesity, etc. Through this process, potential correlations between optoacoustic and other imaging modalities used in daily clinical routine could be

revealed, strengthening the position of optoacoustics as an additional method to the established diagnostic tools in clinical practice.

6 Bibliography

[1] S. Ahmed, P. Shah, and O. Ahmed, "Biochemistry, Lipids," in *StatPearls*. Treasure Island (FL): StatPearls Publishing
Copyright © 2023, StatPearls Publishing LLC., 2023.

[2] C. Ophardt, "Lipid Catabolism Summary," *Virtual ChemBook. Elmhurst College.,* 2003. [Online]. Available: http://chemistry.elmhurst.edu/vchembook/622overview.html.

[3] A. F. Hofmann and B. Borgstrom, "Physico-chemical state of lipids in intestinal content during their digestion and absorption," *Fed Proc,* vol. 21, pp. 43-50, Jan-Feb 1962. [Online]. Available: https://www.ncbi.nlm.nih.gov/pubmed/13908158.

[4] J. Iqbal and M. M. Hussain, "Intestinal lipid absorption," *Am J Physiol Endocrinol Metab,* vol. 296, no. 6, pp. E1183-94, Jun 2009, doi: 10.1152/ajpendo.90899.2008.

[5] K. R. Feingold, "Introduction to Lipids and Lipoproteins," in *Endotext*, K. R. Feingold *et al.* Eds. South Dartmouth (MA), 2000.

[6] C. Ophardt, "Overview of lipid function," *Virtual ChemBook. Elmhurst College. Available from: http://chemistry. elmhurst. edu/vchembook/620fattyacid. html,* 2003.

[7] Z. Song, A. M. Xiaoli, and F. Yang, "Regulation and Metabolic Significance of De Novo Lipogenesis in Adipose Tissues," *Nutrients,* vol. 10, no. 10, Sep 29 2018, doi: 10.3390/nu10101383.

[8] R. H. Wong and H. S. Sul, "Insulin signaling in fatty acid and fat synthesis: a transcriptional perspective," *Curr Opin Pharmacol,* vol. 10, no. 6, pp. 684-91, Dec 2010, doi: 10.1016/j.coph.2010.08.004.

[9] M. Bluher, "Adipose tissue dysfunction contributes to obesity related metabolic diseases," *Best Pract Res Clin Endocrinol Metab,* vol. 27, no. 2, pp. 163-77, Apr 2013, doi: 10.1016/j.beem.2013.02.005.

[10] A. Guilherme, J. V. Virbasius, V. Puri, and M. P. Czech, "Adipocyte dysfunctions linking obesity to insulin resistance and type 2 diabetes," *Nat Rev Mol Cell Biol,* vol. 9, no. 5, pp. 367-77, May 2008, doi: 10.1038/nrm2391.

[11] S. M. Grundy *et al.*, "Diagnosis and management of the metabolic syndrome: an American Heart Association/National Heart, Lung, and Blood Institute Scientific Statement," *Circulation,* vol. 112, no. 17, pp. 2735-52, Oct 25 2005, doi: 10.1161/CIRCULATIONAHA.105.169404.

[12] V. D. Dahik, E. Frisdal, and W. Le Goff, "Rewiring of Lipid Metabolism in Adipose Tissue Macrophages in Obesity: Impact on Insulin Resistance and Type 2 Diabetes," (in eng), *Int J Mol Sci,* vol. 21, no. 15, Jul 31 2020, doi: 10.3390/ijms21155505.

[13] K. R. Feingold, "Obesity and Dyslipidemia," in *Endotext*, K. R. Feingold *et al.* Eds. South Dartmouth (MA): MDText.com, Inc.
Copyright © 2000-2023, MDText.com, Inc., 2000.

[14] W. Tomeno *et al.*, "Complications of Non-Alcoholic Fatty Liver Disease in Extrahepatic Organs," (in eng), *Diagnostics (Basel),* vol. 10, no. 11, Nov 7 2020, doi: 10.3390/diagnostics10110912.

[15] J. Y. Kim, R. C. Hickner, R. L. Cortright, G. L. Dohm, and J. A. Houmard, "Lipid oxidation is reduced in obese human skeletal muscle," (in eng), *Am J Physiol Endocrinol Metab,* vol. 279, no. 5, pp. E1039-44, Nov 2000, doi: 10.1152/ajpendo.2000.279.5.E1039.

[16] L. A. Consitt, J. A. Bell, and J. A. Houmard, "Intramuscular lipid metabolism, insulin action, and obesity," (in eng), *IUBMB Life,* vol. 61, no. 1, pp. 47-55, Jan 2009, doi: 10.1002/iub.142.

[17] B. H. Goodpaster and D. Wolf, "Skeletal muscle lipid accumulation in obesity, insulin resistance, and type 2 diabetes," (in eng), *Pediatr Diabetes,* vol. 5, no. 4, pp. 219-26, Dec 2004, doi: 10.1111/j.1399-543X.2004.00071.x.

[18] K. G. Parhofer, "Interaction between Glucose and Lipid Metabolism: More than Diabetic Dyslipidemia," (in eng), *Diabetes Metab J,* vol. 39, no. 5, pp. 353-62, Oct 2015, doi: 10.4093/dmj.2015.39.5.353.

[19] A. A. Rivellese, O. Vaccaro, and L. Patti, "The pathophysiology of lipid metabolism and diabetes," *International Journal of Clinical Practice,* vol. 58, no. s142, pp. 32-35, 2004, doi: https://doi.org/10.1111/j.1368-504X.2004.00332.x.

[20] V. G. Athyros, M. Doumas, K. P. Imprialos, K. Stavropoulos, E. Georgianou, A. Katsimardou, and A. Karagiannis, "Diabetes and lipid metabolism," *Hormones,* vol. 17, no. 1, pp. 61-67, 2018/03/01 2018, doi: 10.1007/s42000-018-0014-8.

[21] J. J. Fuster, N. Ouchi, N. Gokce, and K. Walsh, "Obesity-Induced Changes in Adipose Tissue Microenvironment and Their Impact on Cardiovascular Disease," (in eng), *Circ Res,* vol. 118, no. 11, pp. 1786-807, May 27 2016, doi: 10.1161/circresaha.115.306885.

[22] M. S. Burhans, D. K. Hagman, J. N. Kuzma, K. A. Schmidt, and M. Kratz, "Contribution of Adipose Tissue Inflammation to the Development of Type 2 Diabetes Mellitus," (in eng), *Compr Physiol,* vol. 9, no. 1, pp. 1-58, Dec 13 2018, doi: 10.1002/cphy.c170040.

[23] G. R. Hajer, T. W. van Haeften, and F. L. Visseren, "Adipose tissue dysfunction in obesity, diabetes, and vascular diseases," (in eng), *European heart journal,* vol. 29, no. 24, pp. 2959-71, Dec 2008, doi: 10.1093/eurheartj/ehn387.

[24] R. Berry, C. D. Church, M. T. Gericke, E. Jeffery, L. Colman, and M. S. Rodeheffer, "Imaging of adipose tissue," (in eng), *Methods Enzymol,* vol. 537, pp. 47-73, 2014, doi: 10.1016/b978-0-12-411619-1.00004-5.

[25] A. Paulus, W. van Marken Lichtenbelt, F. M. Mottaghy, and M. Bauwens, "Brown adipose tissue and lipid metabolism imaging," *Methods,* vol. 130, pp. 105-113, 2017/11/01/ 2017, doi: https://doi.org/10.1016/j.ymeth.2017.05.001.

[26] W. Shen *et al.*, "Adipose tissue quantification by imaging methods: a proposed classification," (in eng), *Obes Res,* vol. 11, no. 1, pp. 5-16, Jan 2003, doi: 10.1038/oby.2003.3.

[27] P. Tandon, R. Wafer, and J. E. N. Minchin, "Adipose morphology and metabolic disease," (in eng), *J Exp Biol,* vol. 221, no. Pt Suppl 1, Mar 7 2018, doi: 10.1242/jeb.164970.

[28] S. S. Choe, J. Y. Huh, I. J. Hwang, J. I. Kim, and J. B. Kim, "Adipose Tissue Remodeling: Its Role in Energy Metabolism and Metabolic Disorders," (in eng), *Front Endocrinol (Lausanne),* vol. 7, p. 30, 2016, doi: 10.3389/fendo.2016.00030.

[29] X. Yang and U. Smith, "Adipose tissue distribution and risk of metabolic disease: does thiazolidinedione-induced adipose tissue redistribution provide a clue to the answer?," (in eng), *Diabetologia,* vol. 50, no. 6, pp. 1127-39, Jun 2007, doi: 10.1007/s00125-007-0640-1.

[30] S. Elattar and A. Satyanarayana, "Can Brown Fat Win the Battle Against White Fat?," (in eng), *J Cell Physiol,* vol. 230, no. 10, pp. 2311-7, Oct 2015, doi: 10.1002/jcp.24986.

[31] D. R. Wagner, "Ultrasound as a tool to assess body fat," (in eng), *J Obes,* vol. 2013, p. 280713, 2013, doi: 10.1155/2013/280713.

[32] P. Störchle, W. Müller, M. Sengeis, S. Lackner, S. Holasek, and A. Fürhapter-Rieger, "Measurement of mean subcutaneous fat thickness: eight standardised ultrasound sites compared to 216 randomly selected sites," *Scientific reports,* vol. 8, no. 1, p. 16268, 2018/11/02 2018, doi: 10.1038/s41598-018-34213-0.

[33] H. Angoorani, Z. Karimi, F. Naderi, and A. Mazaherinezhad, "Is ultrasound-measured abdominal fat thickness a reliable method for predicting metabolic diseases in obese and overweight women?," (in eng), *Med J Islam Repub Iran,* vol. 32, p. 78, 2018, doi: 10.14196/mjiri.32.78.

[34] A. Flynn *et al.*, "Contrast-Enhanced Ultrasound: A Novel Noninvasive, Nonionizing Method for the Detection of Brown Adipose Tissue in Humans," (in eng), *J Am Soc Echocardiogr,* vol. 28, no. 10, pp. 1247-54, Oct 2015, doi: 10.1016/j.echo.2015.06.014.

[35] W. Müller *et al.*, "Subcutaneous fat patterning in athletes: selection of appropriate sites and standardisation of a novel ultrasound measurement technique: ad hoc working group on body composition, health and performance, under the auspices of the IOC Medical Commission," (in eng), *Br J Sports Med,* vol. 50, no. 1, pp. 45-54, Jan 2016, doi: 10.1136/bjsports-2015-095641.

[36] H. H. Hu, K. S. Nayak, and M. I. Goran, "Assessment of abdominal adipose tissue and organ fat content by magnetic resonance imaging," (in eng), *Obes Rev,* vol. 12, no. 5, pp. e504-15, May 2011, doi: 10.1111/j.1467-789X.2010.00824.x.

[37] M. Wu, D. Junker, R. T. Branca, and D. C. Karampinos, "Magnetic Resonance Imaging Techniques for Brown Adipose Tissue Detection," (in eng), *Front Endocrinol (Lausanne),* vol. 11, p. 421, 2020, doi: 10.3389/fendo.2020.00421.

[38] D. Franz, J. Syväri, D. Weidlich, T. Baum, E. J. Rummeny, and D. C. Karampinos, "Magnetic Resonance Imaging of Adipose Tissue in Metabolic Dysfunction," (in eng), *Rofo,* vol. 190, no. 12, pp. 1121-1130, Dec 2018, doi: 10.1055/a-0612-8006. MR-Bildgebung von Fettgewebe bei Stoffwechselstörungen.

[39] E. Lin and A. Alessio, "What are the basic concepts of temporal, contrast, and spatial resolution in cardiac CT?," (in eng), *J Cardiovasc Comput Tomogr,* vol. 3, no. 6, pp. 403-8, Nov-Dec 2009, doi: 10.1016/j.jcct.2009.07.003.

[40] L. C. Pescatori, E. Savarino, G. Mauri, E. Silvestri, M. Cariati, F. Sardanelli, and L. M. Sconfienza, "Quantification of visceral adipose tissue by computed tomography and magnetic resonance imaging: reproducibility and accuracy," (in eng), *Radiol Bras,* vol. 52, no. 1, pp. 1-6, Jan-Feb 2019, doi: 10.1590/0100-3984.2017.0211.

[41] H. Prodhomme, J. Ognard, P. Robin, Z. Alavi, P. Y. Salaun, and D. Ben Salem, "Imaging and identification of brown adipose tissue on CT scan," (in eng), *Clinical physiology and functional imaging,* vol. 38, no. 2, pp. 186-191, Mar 2018, doi: 10.1111/cpf.12373.

[42] J. Frankl, A. Sherwood, D. J. Clegg, P. E. Scherer, and O. K. Öz, "Imaging Metabolically Active Fat: A Literature Review and Mechanistic Insights," (in eng), *Int J Mol Sci,* vol. 20, no. 21, Nov 5 2019, doi: 10.3390/ijms20215509.

[43] T. Watakabe *et al.*, "High Spatial Resolution Digital Positron Emission Tomography Images With Dedicated Source-to-background Algorithm for Radiotherapy Planning," (in eng), *Anticancer Res,* vol. 40, no. 5, pp. 2567-2572, May 2020, doi: 10.21873/anticanres.14227.

[44] C. R. Young, M. E. Kulon, A. M. Boustani, and D. Pucar, "Altered FDG Biodistribution in Subcutaneous White Fat on PET/CT Following l-Asparaginase Chemotherapy," (in eng), *Clin Nucl Med,* vol. 46, no. 3, pp. e179-e180, Mar 1 2021, doi: 10.1097/rlu.0000000000003340.

[45] S. C. Sampath, S. C. Sampath, M. A. Bredella, A. M. Cypess, and M. Torriani, "Imaging of Brown Adipose Tissue: State of the Art," (in eng), *Radiology,* vol. 280, no. 1, pp. 4-19, Jul 2016, doi: 10.1148/radiol.2016150390.

[46] J. Kullberg *et al.*, "Whole-body adipose tissue analysis: comparison of MRI, CT and dual energy X-ray absorptiometry," (in eng), *Br J Radiol,* vol. 82, no. 974, pp. 123-30, Feb 2009, doi: 10.1259/bjr/80083156.

[47] R. Scherzer *et al.*, "Comparison of dual-energy X-ray absorptiometry and magnetic resonance imaging-measured adipose tissue depots in HIV-infected and control subjects," (in eng), *Am J Clin Nutr,* vol. 88, no. 4, pp. 1088-96, Oct 2008, doi: 10.1093/ajcn/88.4.1088.

[48] M. Lubura, D. Hesse, N. Neumann, S. Scherneck, P. Wiedmer, and A. Schürmann, "Non-invasive quantification of white and brown adipose tissues and liver fat content by computed tomography in mice," (in eng), *PloS one,* vol. 7, no. 5, p. e37026, 2012, doi: 10.1371/journal.pone.0037026.

[49] M. Borga, J. West, J. D. Bell, N. C. Harvey, T. Romu, S. B. Heymsfield, and O. Dahlqvist Leinhard, "Advanced body composition assessment: from body mass index to body composition profiling," (in eng), *J Investig Med,* vol. 66, no. 5, pp. 1-9, Jun 2018, doi: 10.1136/jim-2018-000722.

[50] A. M. Coletta, A. H. Klopp, D. Fogelman, A. M. Parikh, Y. Li, N. Garg, and K. Basen-Engquist, "Dual-Energy X-Ray Absorptiometry Compared to Computed Tomography for Visceral Adiposity Assessment Among Gastrointestinal and Pancreatic Cancer Survivors," (in eng), *Scientific reports,* vol. 9, no. 1, p. 11500, Aug 8 2019, doi: 10.1038/s41598-019-48027-1.

[51] R. Meral *et al.*, ""Fat Shadows" From DXA for the Qualitative Assessment of Lipodystrophy: When a Picture Is Worth a Thousand Numbers," (in eng), *Diabetes Care,* vol. 41, no. 10, pp. 2255-2258, Oct 2018, doi: 10.2337/dc18-0978.

[52] J. Law, J. Chalmers, D. E. Morris, L. Robinson, H. Budge, and M. E. Symonds, "The use of infrared thermography in the measurement and characterization of brown adipose tissue

activation," (in eng), *Temperature (Austin),* vol. 5, no. 2, pp. 147-161, 2018, doi: 10.1080/23328940.2017.1397085.

[53] L. Sun *et al.*, "Brown Adipose Tissue: Multimodality Evaluation by PET, MRI, Infrared Thermography, and Whole-Body Calorimetry (TACTICAL-II)," (in eng), *Obesity (Silver Spring, Md.),* vol. 27, no. 9, pp. 1434-1442, Sep 2019, doi: 10.1002/oby.22560.

[54] J. Reber *et al.*, "Non-invasive Measurement of Brown Fat Metabolism Based on Optoacoustic Imaging of Hemoglobin Gradients," *Cell Metabolism,* vol. 27, no. 3, pp. 689-701.e4, 2018, doi: 10.1016/j.cmet.2018.02.002.

[55] A. Karlas, M. A. Pleitez, J. Aguirre, and V. Ntziachristos, "Optoacoustic imaging in endocrinology and metabolism," (in eng), *Nat Rev Endocrinol,* Apr 19 2021, doi: 10.1038/s41574-021-00482-5.

[56] A. Karlas *et al.*, "Multispectral optoacoustic tomography of lipid and hemoglobin contrast in human carotid atherosclerosis," *Photoacoustics,* vol. 23, p. 100283, 2021/09/01/ 2021, doi: https://doi.org/10.1016/j.pacs.2021.100283.

[57] N. A. Fasoula *et al.*, "Multicompartmental non-invasive sensing of postprandial lipemia in humans with multispectral optoacoustic tomography," *Mol Metab,* vol. 47, p. 101184, May 2021, doi: 10.1016/j.molmet.2021.101184.

[58] N. A. Fasoula *et al.*, "Non-invasive multispectral optoacoustic tomography resolves intrahepatic lipids in patients with hepatic steatosis," *Photoacoustics,* vol. 29, p. 100454, Feb 2023, doi: 10.1016/j.pacs.2023.100454.

[59] E. J. Barrett *et al.*, "Diabetic Microvascular Disease: An Endocrine Society Scientific Statement," *J Clin Endocrinol Metab,* vol. 102, no. 12, pp. 4343-4410, Dec 1 2017, doi: 10.1210/jc.2017-01922.

[60] M. Brownlee, "The Pathobiology of Diabetic Complications," *A Unifying Mechanism,* vol. 54, no. 6, pp. 1615-1625, 2005, doi: 10.2337/diabetes.54.6.1615.

[61] A. E. Caballero *et al.*, "Microvascular and macrovascular reactivity is reduced in subjects at risk for type 2 diabetes," (in English), *Diabetes,* vol. 48, no. 9, pp. 1856-1862, Sep 1999, doi: DOI 10.2337/diabetes.48.9.1856.

[62] A. J. Deegan and R. K. Wang, "Microvascular imaging of the skin," *Phys Med Biol,* vol. 64, no. 7, p. 07TR01, Mar 21 2019, doi: 10.1088/1361-6560/ab03f1.

[63] S. Tehrani, K. Bergen, L. Azizi, and G. Jörneskog, "Skin microvascular reactivity correlates to clinical microangiopathy in type 1 diabetes: A pilot study," (in English), *Diabetes Vasc Dis Re,* vol. 17, no. 3, May 2020, doi: Artn 1479164120928303 10.1177/1479164120928303.

[64] O. A. Mennes, J. J. van Netten, J. G. van Baal, R. H. J. A. Slart, and W. Steenbergen, "The Association between Foot and Ulcer Microcirculation Measured with Laser Speckle Contrast Imaging and Healing of Diabetic Foot Ulcers," (in English), *Journal of Clinical Medicine,* vol. 10, no. 17, Sep 2021, doi: ARTN 3844 10.3390/jcm10173844.

[65] A. Bjorgan, M. Milanic, and L. L. Randeberg, "Estimation of skin optical parameters for real-time hyperspectral imaging applications," *J Biomed Opt,* vol. 19, no. 6, p. 066003, Jun 2014, doi: 10.1117/1.JBO.19.6.066003.

[66] Y. Wu, Z. Xu, W. Yang, Z. Ning, and H. Dong, "Review on the Application of Hyperspectral Imaging Technology of the Exposed Cortex in Cerebral Surgery," *Front Bioeng Biotechnol,* vol. 10, p. 906728, 2022, doi: 10.3389/fbioe.2022.906728.

[67] Q. Yang, S. Sun, W. J. Jeffcoate, D. J. Clark, A. Musgove, F. L. Game, and S. P. Morgan, "Investigation of the Performance of Hyperspectral Imaging by Principal Component Analysis in the Prediction of Healing of Diabetic Foot Ulcers," (in English), *J Imaging,* vol. 4, no. 12, Dec 2018, doi: ARTN 144 10.3390/jimaging4120144.

[68] G. Saiko, P. Lombardi, Y. H. Au, D. Queen, D. Armstrong, and K. Harding, "Hyperspectral imaging in wound care: A systematic review," (in English), *Int Wound J,* vol. 17, no. 6, pp. 1840-1856, Dec 2020, doi: 10.1111/iwj.13474.

[69] R. Argarini *et al.*, "Optical coherence tomography: a novel imaging approach to visualize and quantify cutaneous microvascular structure and function in patients with diabetes," *BMJ Open Diabetes Res Care,* vol. 8, no. 1, Aug 2020, doi: 10.1136/bmjdrc-2020-001479.

[70] B. Hindelang *et al.*, "Enabling precision monitoring of psoriasis treatment by optoacoustic mesoscopy," (in English), *Sci Transl Med,* vol. 14, no. 644, May 11 2022, doi: ARTN eabm8059
10.1126/scitranslmed.abm8059.

[71] H. He *et al.*, "Opening a window to skin biomarkers for diabetes stage with optoacoustic mesoscopy," *Light Sci Appl,* vol. 12, no. 1, p. 231, Sep 18 2023, doi: 10.1038/s41377-023-01275-3.

[72] C. Lutzweiler and D. Razansky, "Optoacoustic imaging and tomography: reconstruction approaches and outstanding challenges in image performance and quantification.," (in en), *Sensors (Basel),* vol. 13, pp. 7345-84, 2013, doi: 10.3390/s130607345.

[73] A. Karlas *et al.*, "Cardiovascular optoacoustics: From mice to men - A review," (in eng), *Photoacoustics,* vol. 14, pp. 19-30, Jun 2019, doi: 10.1016/j.pacs.2019.03.001.

[74] A. Taruttis, G. M. van Dam, and V. Ntziachristos, "Mesoscopic and Macroscopic Optoacoustic Imaging of Cancer," *Cancer Research,* vol. 75, no. 8, pp. 1548-59, 2015.

[75] M. Visscher, M. A. Pleitez, K. Van Gaalen, I. M. Nieuwenhuizen-Bakker, V. Ntziachristos, and G. Van Soest, "Label-free analytic histology of carotid atherosclerosis by mid-infrared optoacoustic microscopy," (in eng), *Photoacoustics,* vol. 26, p. 100354, Jun 2022, doi: 10.1016/j.pacs.2022.100354.

[76] C. Cano, C. Matos, A. Gholampour, M. van Sambeek, R. Lopata, and M. Wu, "Blind spectral unmixing for characterization of plaque composition based on multispectral photoacoustic imaging," *Scientific reports,* vol. 13, no. 1, p. 4119, 2023/03/13 2023, doi: 10.1038/s41598-023-31343-y.

[77] M. Schwarz, M. Omar, A. Buehler, J. Aguirre, and V. Ntziachristos, "Implications of ultrasound frequency in optoacoustic mesoscopy of the skin," (in eng), *IEEE transactions on medical imaging,* vol. 34, no. 2, pp. 672-7, Feb 2015, doi: 10.1109/tmi.2014.2365239.

[78] J. Aguirre, M. Schwarz, N. Garzorz, M. Omar, A. Buehler, K. Eyerich, and V. Ntziachristos, "Precision assessment of label-free psoriasis biomarkers with ultra-broadband optoacoustic mesoscopy," *Nat Biomed Eng,* Article vol. 1, p. 0068, 05/10/online 2017. [Online]. Available: http://dx.doi.org/10.1038/s41551-017-0068.

[79] T. L. I. o. America., "American national standards for the safe use of lasers," in "ANSI Z136.1," 2000.

[80] M. Omar, D. Soliman, J. Gateau, and V. Ntziachristos, "Ultrawideband reflection-mode optoacoustic mesoscopy," *Opt Lett,* vol. 39, no. 13, pp. 3911-4, Jul 1 2014, doi: 10.1364/OL.39.003911.

[81] M. Omar, J. Gateau, and V. Ntziachristos, "Raster-scan optoacoustic mesoscopy in the 25-125 MHz range," *Opt Lett,* vol. 38, no. 14, pp. 2472-4, Jul 15 2013, doi: 10.1364/OL.38.002472.

[82] H. He *et al.*, "Fast raster-scan optoacoustic mesoscopy enables assessment of human melanoma microvasculature in vivo," *Nature Communications,* vol. 13, no. 1, p. 2803, 2022/05/19 2022, doi: 10.1038/s41467-022-30471-9.

[83] A. Karlas, A. Nunes, W. Driessen, E. Liapis, and J. Reber, "Multi-Aspect Optoacoustic Imaging of Breast Tumors under Chemotherapy with Exogenous and Endogenous Contrasts: Focus on Apoptosis and Hypoxia," (in eng), *Biomedicines,* vol. 9, no. 11, Nov 16 2021, doi: 10.3390/biomedicines9111696.

[84] A. Karlas *et al.*, "Multispectral Optoacoustic Tomography of Muscle Perfusion and Oxygenation under Arterial and Venous Occlusion - A Human Pilot Study," (in eng), *J Biophotonics,* p. e201960169, Mar 5 2020, doi: 10.1002/jbio.201960169.

[85] A. Karlas *et al.*, "Flow-mediated dilatation test using optoacoustic imaging: a proof-of-concept," *Biomed Optics Express,* vol. 8, no. 7, pp. 3395-3403, 2017/07/01 2017, doi: 10.1364/BOE.8.003395.

[86] I. Dimaridis, P. Sridharan, V. Ntziachristos, A. Karlas, and L. Hadjileontiadis, "Image Quality Improvement Techniques and Assessment Adequacy in Clinical Optoacoustic Imaging: A Systematic Review," (in eng), *Biosensors (Basel),* vol. 12, no. 10, Oct 20 2022, doi: 10.3390/bios12100901.

[87] A. Rosenthal, V. Ntziachristos, and D. Razansky, "Acoustic Inversion in Optoacoustic Tomography: A Review.," *Current medical imaging reviews,* vol. 9, pp. 318-336, 2013, doi: 10.2174/15734056113096660006.
[88] A. Rosenthal, V. Ntziachristos, and D. Razansky, "Model-based optoacoustic inversion with arbitrary-shape detectors," (in eng), *Medical physics,* vol. 38, no. 7, pp. 4285-95, Jul 2011, doi: 10.1118/1.3589141.
[89] I. Olefir, S. Tzoumas, C. Restivo, P. Mohajerani, L. Xing, and V. Ntziachristos, "Deep Learning-Based Spectral Unmixing for Optoacoustic Imaging of Tissue Oxygen Saturation," (in eng), *IEEE transactions on medical imaging,* vol. 39, no. 11, pp. 3643-3654, Nov 2020, doi: 10.1109/tmi.2020.3001750.
[90] I. Olefir, S. Tzoumas, H. Yang, and V. Ntziachristos, "A Bayesian Approach to Eigenspectra Optoacoustic Tomography," (in eng), *IEEE Trans Med Imaging,* vol. 37, no. 9, pp. 2070-2079, Sep 2018, doi: 10.1109/tmi.2018.2815760.
[91] S. Tzoumas and V. Ntziachristos, "Spectral unmixing techniques for optoacoustic imaging of tissue pathophysiology," (in eng), *Philos Trans A Math Phys Eng Sci,* vol. 375, no. 2107, Nov 28 2017, doi: 10.1098/rsta.2017.0262.
[92] G.-S. Jeng *et al.*, "Real-time spectroscopic photoacoustic/ultrasound (PAUS) scanning with simultaneous fluence compensation and motion correction for quantitative molecular imaging," *bioRxiv,* p. 2019.12.20.885251, 2019, doi: 10.1101/2019.12.20.885251.
[93] M. Schwarz, N. Garzorz-Stark, K. Eyerich, J. Aguirre, and V. Ntziachristos, "Motion correction in optoacoustic mesoscopy," (in eng), *Sci Rep,* vol. 7, no. 1, p. 10386, Sep 04 2017, doi: 10.1038/s41598-017-11277-y.
[94] S. Han, D. Lee, S. Kim, H. H. Kim, S. Jeong, and J. Kim, "Contrast Agents for Photoacoustic Imaging: A Review Focusing on the Wavelength Range," (in eng), *Biosensors (Basel),* vol. 12, no. 8, Aug 3 2022, doi: 10.3390/bios12080594.
[95] D. Razansky *et al.*, "Multispectral Optoacoustic Tomography of Matrix Metalloproteinase Activity in Vulnerable Human Carotid Plaques," in *Mol Imaging Biol*, vol. 14, no. 3), 2012, pp. 277-85.
[96] W. Olejarz, D. Łacheta, and G. Kubiak-Tomaszewska, "Matrix Metalloproteinases as Biomarkers of Atherosclerotic Plaque Instability," (in eng), *Int J Mol Sci,* vol. 21, no. 11, May 31 2020, doi: 10.3390/ijms21113946.
[97] N. Liu *et al.*, "Croconaine-based nanoparticles enable efficient optoacoustic imaging of murine brain tumors," *Photoacoustics,* vol. 22, p. 100263, 2021/06/01/ 2021, doi: https://doi.org/10.1016/j.pacs.2021.100263.
[98] A. Karlas *et al.*, "Multispectral optoacoustic tomography of peripheral arterial disease based on muscle hemoglobin gradients-a pilot clinical study," (in eng), *Ann Transl Med,* vol. 9, no. 1, p. 36, Jan 2021, doi: 10.21037/atm-20-3321.
[99] E. Liapis, U. Klemm, A. Karlas, J. Reber, and V. Ntziachristos, "Resolution of spatial and temporal heterogeneity in bevacizumab-treated breast tumors by eigenspectra multispectral optoacoustic tomography," (in eng), *Cancer Res,* Sep 29 2020, doi: 10.1158/0008-5472.can-20-1011.
[100] C. Lee *et al.*, "Panoramic volumetric clinical handheld photoacoustic and ultrasound imaging," *Photoacoustics,* vol. 31, p. 100512, Jun 2023, doi: 10.1016/j.pacs.2023.100512.
[101] S. Tzoumas *et al.*, "Eigenspectra optoacoustic tomography achieves quantitative blood oxygenation imaging deep in tissues.," *Nat Commun,* vol. 7, p. 12121, 2016, doi: 10.1038/ncomms12121.
[102] J. S. Cohn, J. R. McNamara, S. D. Cohn, J. M. Ordovas, and E. J. Schaefer, "Postprandial plasma lipoprotein changes in human subjects of different ages," *J Lipid Res,* vol. 29, no. 4, pp. 469-79, Apr 1988. [Online]. Available: https://www.ncbi.nlm.nih.gov/pubmed/3392464.
[103] J. R. Patsch *et al.*, "Relation of triglyceride metabolism and coronary artery disease. Studies in the postprandial state," *Arterioscler Thromb,* vol. 12, no. 11, pp. 1336-45, Nov 1992, doi: 10.1161/01.atv.12.11.1336.
[104] F. Karpe, "Postprandial lipoprotein metabolism and atherosclerosis," *J Intern Med,* vol. 246, no. 4, pp. 341-55, Oct 1999, doi: 10.1046/j.1365-2796.1999.00548.x.

[105] N. Tamaki, V. Ajmera, and R. Loomba, "Non-invasive methods for imaging hepatic steatosis and their clinical importance in NAFLD," (in English), *Nat Rev Endocrinol,* vol. 18, no. 1, pp. 55-66, Jan 2022, doi: 10.1038/s41574-021-00584-0.

Appendix A

Publication: Multicompartmental non-invasive sensing of postprandial lipemia in humans with multispectral optoacoustic tomography

Brief Communication

MOLECULAR METABOLISM

Multicompartmental non-invasive sensing of postprandial lipemia in humans with multispectral optoacoustic tomography

Nikolina-Alexia Fasoula [1,2,8], Angelos Karlas [1,2,3,8], Michael Kallmayer [3], Anamaria Beatrice Milik [1,2], Jaroslav Pelisek [3,4], Hans-Henning Eckstein [3], Martin Klingenspor [5,6,7], Vasilis Ntziachristos [1,2,*]

ABSTRACT

Objective: Postprandial lipid profiling (PLP), a risk indicator of cardiometabolic disease, is based on frequent blood sampling over several hours after a meal, an approach that is invasive and inconvenient. Non-invasive PLP may offer an alternative for disseminated human monitoring. Herein, we investigate the use of clinical multispectral optoacoustic tomography (MSOT) for non-invasive, label-free PLP via direct lipid-sensing in human vasculature and soft tissues.

Methods: Four ($n = 4$) subjects (3 females and 1 male, age: 28 ± 7 years) were enrolled in the current pilot study. We longitudinally measured the lipid signals in arteries, veins, skeletal muscles, and adipose tissues of all participants at 30-min intervals for 6 h after the oral consumption of a high-fat meal.

Results: Optoacoustic lipid-signal analysis showed on average a 63.4% intra-arterial increase at ~ 4 h postprandially, an 83.9% intra-venous increase at ~ 3 h, a 120.8% intra-muscular increase at ~ 3 h, and a 32.8% subcutaneous fat increase at ~ 4 h.

Conclusion: MSOT provides the potential to study lipid metabolism that could lead to novel diagnostics and prevention strategies by label-free, non-invasive detection of tissue biomarkers implicated in cardiometabolic diseases.

Keywords Cardiovascular risk; Fat; Hyperlipidemia; Lipid metabolism; Metabolic imaging; Photoacoustics

1. INTRODUCTION

High blood lipid levels in either fasting or postprandial states indicate high risk for developing cardiovascular (CVD) and metabolic diseases, such as coronary artery disease (CAD), stroke, peripheral arterial disease (PAD), obesity, diabetes, and non-alcoholic fatty liver disease (NAFLD) [1–7]. Although fasting blood lipid measurements have been successfully employed over the past decades for disease risk stratification [8,9], the postprandial blood lipid levels are often better predictors of acute complications, such as heart attack, stroke, or death [10]. For example, an analysis of the lipid profiles in 42,710 patients in the non-fasting state showed that the non-fasting levels of lipids predicted increased risk of cardiovascular events [9]. Furthermore, lipid analysis of 8,270 subjects provided strong evidence to support the routine use of postprandial lipid levels in clinical practice for accurate risk assessment of atherosclerotic CVD [11].

Assessment of fasting blood lipid concentrations is primarily done by single time-point blood sampling via venipuncture. Moreover, measurements of blood lipid dynamics can be carried out by several blood samplings after the consumption of a high-fat meal to yield more information on lipid metabolism (postprandial lipid profiling, PLP) [12]. In both cases, the acquisition of blood samples causes patient discomfort, consumes hospital time and resources, and is only appropriate for infrequent sampling. Importantly, these methods of sampling lipids only allow observations in the blood and not in different tissue types.

Current non-invasive methods for lipid measurements in humans include breath measurements and eye image analysis. Lipid metabolism produces volatile organic compounds (VOCs, such as 2-pentyl nitrate, carbon dioxide, methyl nitrate, and toluene), some of which are exhaled. In one study, these VOCs were exploited to quantify blood lipid levels [13]. Lipids can also accrue in the cornea after arriving through the blood stream of the limbal vessels under hyperlipidemic conditions. Processing of images taken from the human eye (RGB color representation) calculated the corneal lipid deposition by analyzing the grayscale intensity level within the region of lipid deposits [14]. Based

[1]Technical University of Munich, School of Medicine, Chair of Biological Imaging, Germany [2]Helmholtz Zentrum München, Neuherberg, Institute of Biological and Medical Imaging, Germany [3]Clinic of Vascular and Endovascular Surgery, Klinikum rechts der Isar, Munich, Germany [4]Department of Vascular Surgery, University Hospital Zurich, Zurich, Switzerland [5]Chair of Molecular Nutritional Medicine, TUM School of Life Sciences Weihenstephan, Technical University of Munich, Freising, Germany [6]EKFZ-Else Kröner-Fresenius Zentrum for Nutritional Medicine, Technical University of Munich, Freising, Germany [7]ZIEL-Institute for Food &Health, Technical University of Munich, Freising, Germany

[8] Equal contribution.

*Corresponding author. Technical University of Munich, School of Medicine, Chair of Biological Imaging, Germany. E-mail: v.ntziachristos@tum.de (V. Ntziachristos).

Received October 7, 2020 • Revision received February 1, 2021 • Accepted February 1, 2021 • Available online 5 February 2021

https://doi.org/10.1016/j.molmet.2021.101184

on these values and known lipid values in the blood, a regression model was developed and used to indirectly estimate the blood lipid levels from the extracted image parameters. Both non-invasive methods described above provide estimates of lipid concentration in blood based on mathematical models. However, neither of these methods offers a localized measurement of lipids in blood or tissues, nor direct correlation analysis with either measured VOCs or image intensities. For this reason, they have yet to be integrated into research protocols or clinical practice.

Novel techniques providing direct imaging of lipid distributions and dynamics in blood vessels and tissues could enable non-invasive tests that evaluate the risk for CVD and metabolic diseases, as well as the easy monitoring of nutritional and other metabolic conditions that are difficult to study. Here, we aimed to introduce a method that could go beyond the current state of the art in measuring postprandial lipid dynamics by satisfying three critical specifications. First, the method should be safe, non-invasive and portable, so that it can be seamlessly disseminated to studies of large populations. Second, it should be capable of recording lipid measurements in different tissue compartments, not only single-point bulk measurements, enabling differential studies of lipid circulation and uptake in tissues of interest. Third, it should be capable of frequent sampling to provide a detailed profile of highly resolved spatio-temporal lipid dynamics. Introducing such functionality into lipid research and medical care could significantly expand our knowledge of individual responses to nutritional challenges and offer new abilities for cardiovascular and metabolic risk assessment on a personalized basis.

To introduce this paradigm-shifting performance, we hypothesized that optoacoustic imaging, in particular multispectral optoacoustic tomography (MSOT), could offer a platform to obtain localized non-invasive sensing of lipid concentrations. MSOT acquires images of tissue molecules exhibiting optical absorption at multiple wavelengths in the near-infrared range (NIR) and resolves spectral information, revealing deoxygenated hemoglobin (Hb), oxygenated hemoglobin (HbO_2), and lipids among others (Figure 1) [15]. Thus, MSOT should enable the monitoring of lipid distributions by means of wavelength selection within different tissue compartments. Preliminary evidence demonstrated that MSOT can resolve blood vessels, skeletal muscle, and adipose tissues [16–22]. Furthermore, it was recently shown that MSOT can visualize oxidative metabolism by monitoring the rate of conversion of oxygenated hemoglobin to deoxygenated hemoglobin, revealing oxygen utilization by tissue [16,23,24]. More specifically, observations in animals were corroborated with measurements of oxidative metabolism during brown fat activation in humans and mice [16,23,24]. However, it is currently unknown whether MSOT can resolve lipid dynamics in response to nutritional inputs. Therefore, we employed MSOT to visualize vasculature and other soft tissue compartments in the 700–970 nm spectral window. Then, using observations at 930 nm, a wavelength in which lipids exhibit an absorption peak in the near-infrared [25], we investigated whether we could resolve lipid-specific signals over time in different tissue compartments in response to oral fat intake. MSOT is a safe modality that uses light, does not require labels for imaging lipids and offers high resolution ($<$300 μm) and large fields of view ($>$4 cm) while reaching depths of 3–4 cm in living tissue. We demonstrate in this study that these capabilities combine to afford a novel tool for the non-invasive study of lipid dynamics.

2. MATERIALS AND METHODS

2.1. Study design and experimental protocol

Four (n = 4) subjects (3 females and 1 male, age: 28 ± 7 years) with body mass indices (BMI in kg/m^2) of 28 (subject 1), 31 (subject 2), 23 (subject 3), and 21 (subject 4) were enrolled in the current pilot study.

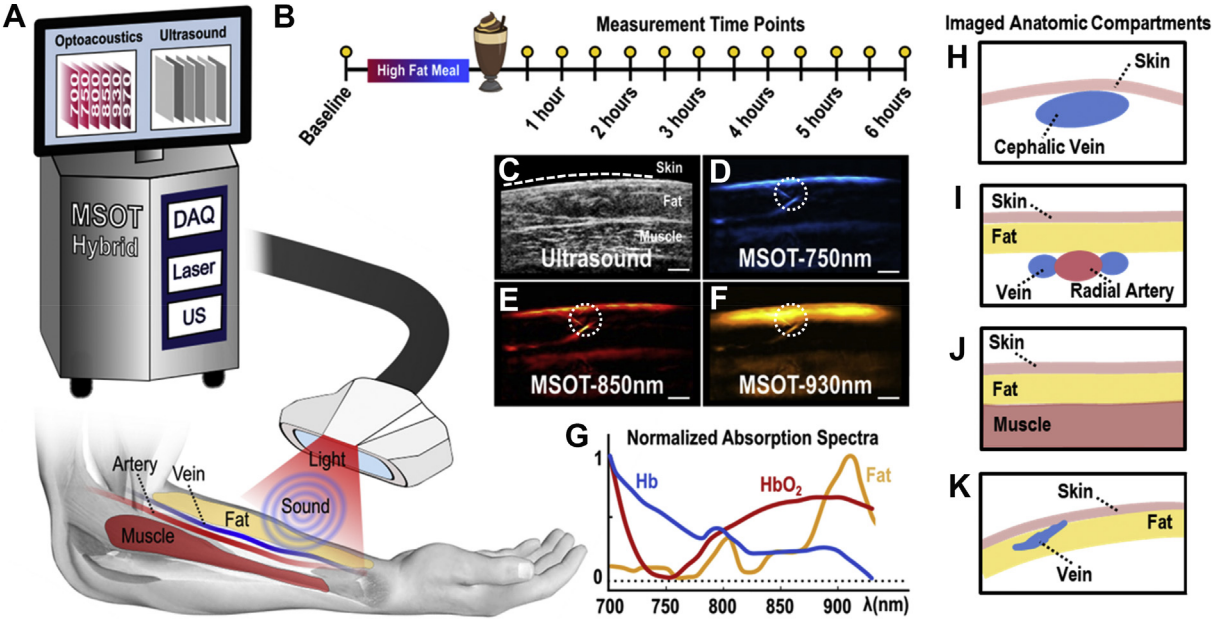

Figure 1: MSOT principle of operation and study design. (A) Configuration of the clinical hybrid MSOT/US system. (B) Postprandial lipemia measurement protocol. (C) Exemplary ultrasound image where the skin line (white dashed line), the subcutaneous fat and the skeletal muscle areas are shown. (D–F) MSOT images corresponding to the ultrasound image in (C). The dotted white circles show a small vessel detail within the subcutaneous fat region, demonstrating the excellent resolution performance of clinical MSOT technology. (D) MSOT image at 750 nm, representing mainly the distribution of deoxygenated Hb. (E) MSOT image at 850 nm, representing mainly the distribution of oxygenated Hb. (F) MSOT image at 930 nm, representing mainly the spatial distribution of lipids. Scale bars are 0.5 cm. (G) Absorption spectra in the near-infrared range (NIR) for Hb, HbO_2 and fat/lipids. (H–K) Schematic diagrams of imaged anatomic compartments in the human forearm. (H) Cephalic vein. (I) Radial artery. (J) Skeletal muscle. (K) Subcutaneous fat.

All volunteers were non-smokers and had no history of cardiovascular or metabolic disease. They were kindly requested to avoid consuming caffeine, food, and alcohol for at least 12 h before the planned measurements. Signed informed consent was obtained from all participants prior to study enrollment. The study was approved by the ethics committee of the medical faculty of the Technical University Munich (Protocol No 349/20 S).

Measurements were conducted in a normal examination room at a temperature of 23 °C. After a 12-h overnight fast, participants ingested an oral fat load within 5 min. The consistency of the fatty meal was 350 ml of pasteurized heavy cream, 15 ml of fat-free milk, 15 ml of chocolate syrup, and 1 tablespoon of granulated sugar. This fat load contained 117 g of fat (70 g saturated fat, 467 mg cholesterol), 41.5 g of carbohydrate, and 0.5 g of protein and provided 1,242 calories (86.4% from fat, 13.4% from carbohydrates, 0.2% from protein) [26]. The high-fat liquid meal was assigned to simulate the fat content of a typical high-fat meal.

A scanning probe was repeatedly placed in the same positions over the radial artery, the cephalic vein, and the brachioradialis muscle of the dominant forearm, guided by stable skin markers (Figure 1A). Recordings of these regions were taken post-fasting and then every 30 min and for 6 h after consumption of the fatty meal (13 measurements in total), which was determined to be a suitable timespan to assess postprandial responses (Figure 1B). The fourth participant felt some light gastric disturbances; hence, we decided to acquire less measurements and stop the experiment at 5 h after the oral loading (5 measurements in total). Each anatomic compartment was scanned for 10 s.

Apart from prior anatomical knowledge, the arteries were initially identified from their pulsation, the veins from their compressibility with the hand-held probe, and the subcutaneous fat and the skeletal muscles by their characteristic textures in traditional ultrasound (US) (Figure 1C). The identification of the different tissues and anatomical compartments was further facilitated by means of their MSOT appearance: the blood vessels and skeletal muscles were characterized by an increased absorption at the 750 nm and 850 nm, compared to the absorption at 930 nm, due to the strong presence of the Hb and HbO_2 in these tissue compartments and the prominent absorption of both at these NIR-wavelengths [19]. Correspondingly, the subcutaneous fat tissue was characterized by an absorption peak at 930 nm where lipids absorb the most in the NIR (Figure 1D–G).

2.2. MSOT data acquisition

Measurements were conducted using a hybrid clinical MSOT/US (Acuity©, iThera Medical GmbH, Munich Germany). For ultrasound detection, the hand-held probe (Figure 1A) was equipped with 256 piezoelectric elements with a central frequency of 4 MHz arranged in an arc of 145°. Illumination was achieved through an optical fiber, mounted on the same hand-held probe. Light was emitted in the form of short pulses (10 ns in duration), at a rate of 25 Hz. For each pulse, almost 15 mJ of energy were delivered over a rectangle area of around 1×4 cm, ensuring compliance with the safety limits of laser use for medical applications [27]. For multispectral image acquisition, we employed 28 different light wavelengths (from 700 to 970 nm at steps of 10 nm). Thus, the recording of one 'multispectral stack', or a full set of 28 single-wavelength optoacoustic images, lasted 1 s. Co-registered US images were recorded in parallel to the MSOT images at frame rate of 8 Hz.

As previously shown, MSOT images acquired at 750 nm reveal primarily Hb contrast, whereas images at 850 nm reveal contrast primarily from HbO_2 [19]. MSOT images at the 930 nm show mainly tissue lipid distribution [16,20,25]. Thus, observed differences in the informational content, or else the appearance of different tissues, in the abovementioned single-wavelength MSOT images (Figure 1D–F) are based on: i) the different features of the known absorption spectra of Hb, HbO_2 and lipids in the NIR (Figure 1G) [25] and ii) the content of Hb, HbO_2 and lipids in the different tissues of each anatomic compartment.

The appearance of different tissues in the MSOT images (Figure 1D–F) showed good spatial correspondence to the co-registered US images (Figure 1C), but with additional functional and molecular contrast. Thus, illumination at 930 nm (Figure 1F) highlights the subcutaneous fat region, which mainly contains lipids and is therefore characterized by much stronger light absorption or else optoacoustic image intensity, compared to adjacent blood vessels and muscles. The dotted white circles in Figure 1D–F mark a small blood vessel in the subcutaneous fat region, highlighting the details that can be recorded by means of clinical MSOT, which achieves a spatial resolution of less than 300 μm. Figure 1H–K shows the anatomical compartments, which were selected for analysis in MSOT images recorded at 930 nm to sense postprandial lipid dynamics in a variety of tissues: i) venous and arterial blood, the gold standard tissues employed for quantifying lipid dynamics in clinical practice, ii) skeletal muscle, which promotes the easy intra-tissue distribution of lipids via its high vascularization and the high-contrast blood lipid imaging due to its low lipid content under normal conditions (best-case scenario) and iii) subcutaneous fat, which is poorly vascularized compared to muscle, and provides a low-contrast environment for postprandial lipemia imaging due to its high lipid content (worst-case scenario).

2.3. Data processing and analysis

Acquired MSOT data were reconstructed using a model-based reconstruction method [28]. The blood vessels (radial artery and cephalic vein) and the soft tissues of the forearm (subcutaneous fat and muscle) were first identified in consensus between two clinicians with experience in clinical MSOT and ultrasound imaging. The identification was based on anatomical knowledge, ultrasound guidance, and the characteristic MSOT appearance for each tissue. For each subject, a set of characteristic 930 nm-frames for all measurement time points was selected. Next, precise regions of interest (ROIs) within the arterial or venous lumen, the subcutaneous fat, and the muscle regions were manually segmented in consensus with two independent clinicians with experience in clinical MSOT and ultrasound imaging. The agreement between the two groups of ROIs was high, as indicated by the Cohen's Kappa value (mean 0.945, interquartile range 0.921–0.969), supporting the reliability of the segmentation process. Finally, the mean intensity values of the pixels belonging to the manually-segmented ROIs were used to plot the time course of the MSOT-extracted lipid signals within each compartment during the lipemia challenge (*see Results*). Lipid signal calculations took place on the recorded 930-nm images, without the application of any filtering or denoising. Calculated values were reported as means or means ± standard deviation.

3. RESULTS

We applied MSOT to study postprandial lipid dynamics in the blood of the cephalic vein (Figure 2A–D) and the radial artery (Figure 2E–H), as well as, in soft tissues (skeletal muscle, Figure 3A–D and subcutaneous fat, Figure 3E–H). Figure 2A illustrates a series of characteristic MSOT images of a cross-section of the cephalic vein (subject #1) acquired at 930 nm that correspond to four time points: before oral

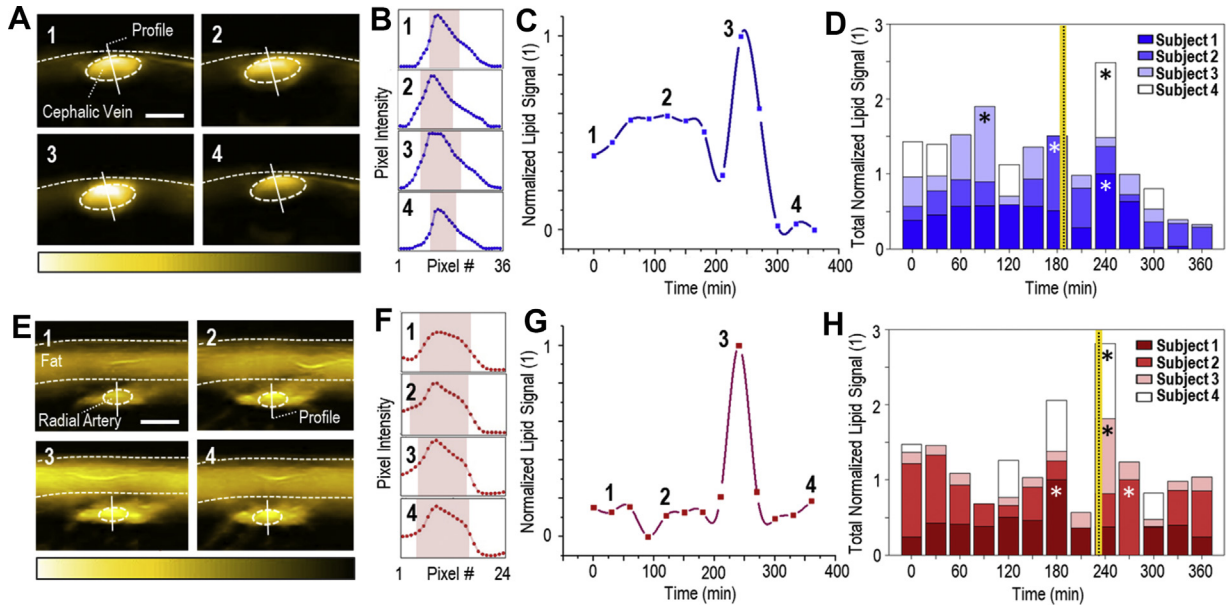

Figure 2: MSOT imaging of postprandial lipid dynamics in the blood of veins and arteries. (A) A series of cross-sectional MSOT images of the cephalic vein recorded at 930 nm, which correspond to the four time points indicated in (C) (subject 1). White dashed line: skin surface. White dashed ellipse: cephalic vein. Scale bars: 0.4 cm. (B) Pixel-intensity cross-sections along the corresponding profile lines in the image series of Figure 2A. The red bands show the pixel range at 50% of the maximum pixel-intensity value along the profile line. (C) Normalized mean lipid signal within the cephalic vein for subject 1 during the whole postprandial lipemia test. The first time point corresponds to the fasting state. (D) MSOT-extracted lipid dynamics for the cephalic veins of all four subjects. The asterisks indicate the time points of the maximum-recorded value for each subject. The vertical yellow-black line indicates the average time point (among all subjects) after oral loading for the maximum-recorded lipid signal within the vein. (E) Cross-sectional MSOT images (at 930 nm) of the radial artery for the four time points of (G) (subject 3). Upper white dashed line: skin surface. Lower white dashed line: lower limit of the subcutaneous fat region. White dashed ellipse: radial artery. Scale bars: 0.3 cm. (F) Pixel-intensity cross-sections along the profile lines of Figure 2E-image series. Red bands: pixel range at 50% of the maximum pixel-value along the profile line. (G) Postprandial lipid dynamics (normalized) within the radial artery for subject 3. (H) MSOT-extracted lipid dynamics for the radial arteries of all subjects. Asterisks: time point of the maximum-recorded value for each subject. The vertical black-yellow line indicates the average recorded time point for the maximum lipid signal within the artery to be recorded.

loading (1), and 120 min (2), 240 min (3), and 330 min (4) after oral loading. The 3rd image (240 min postprandially) corresponds to the time point of the maximum intravenous lipid content. We also analyzed the pixel intensities along the profile lines of the previous image series to gain insights into the contrast between the lipid signal detected inside the current ROI and that of adjacent structures (Figure 2B), that may be also affected during postprandial lipemia. Our results show that both the spatial and temporal fluctuations in lipid signals inside the structures of interest are clearly higher compared to adjacent structures, proving that the observed phenomena are not caused by random fluctuations of the 930-nm signal over the whole image, but by a postprandial increase in the venous blood.

Figure 2C illustrates the changes in the mean lipid signals within the cephalic vein over the whole duration of the experiment for subject #1. Plotted mean values were normalized against the maximum mean value (at 240 min), with the numbered data points corresponding to the MSOT images in Figure 2A. The first time point of Figure 2C represents the baseline state. The lipid signal in the cephalic vein of subject #1 reached its highest value (+32.1% compared to subject's baseline) 240 min after the consumption of the meal (Figure 2C, point 3). Figure 2D shows the normalized lipid signals recorded within the cephalic veins of all subjects for each time point. For Subject #2, the highest value was recorded at 180 min postprandially (+170% compared to the subject's baseline). Subject #3 shows a maximum lipid value of +95.1% compared to baseline at 90 min after meal consumption. The highest MSOT-measured lipid signal in the cephalic vein of Subject #4 is observed at 240 min postprandially (+38.5% compared to subject's baseline). In summary, a mean maximum increase of +83.9% is reported among the four subjects. The intravenous lipid signal reaches its maximum value on average 187.5 min (3 h) after the oral loading. All percentages were extracted from the measured, and not the normalized, optoacoustic signal values. A detailed description of the maximum optoacoustically-extracted lipid values for all subjects and measured anatomic compartments is provided in Table 1.

In brief, the outcomes of the radial artery are similar (Figure 2E–H), with the highest intra-arterial lipid value being recorded at 232.5 min (4 h) after the oral loading, on average. The mean maximum increase observed is 63.4%, relative to the baseline. Furthermore, soft tissues also exhibited a prominent peak in postprandial lipids (Figure 3). An average time span of 180 min is needed for the lipid signal to reach its maximum within the skeletal muscle, which corresponds to an increase of 120.8% relative to baseline (Figure 3A–D). Finally, for the subcutaneous fat, the mean maximum increase is 32.8%, detected on average 217.5 min (4 h) after the oral loading (Figure 3E–H).

To further investigate the observed variability of the postprandial time points of the maximum-recorded lipid signal, we performed a more elaborated statistical analysis with reference to the: i) different anatomic compartments examined and ii) different BMIs of the subjects. Even considering the small sample size, we observed that the anatomic compartment with the lowest standard deviation of the recorded maximum-value time points was the radial artery (232.5 ± 37.7 min). Furthermore, we observed that the two subjects (subjects 1 and 2) characterized as overweight (BMI $>$ 25 kg/m^2) showed lower standard deviations (subject 1: 28.7 min, subject 2:

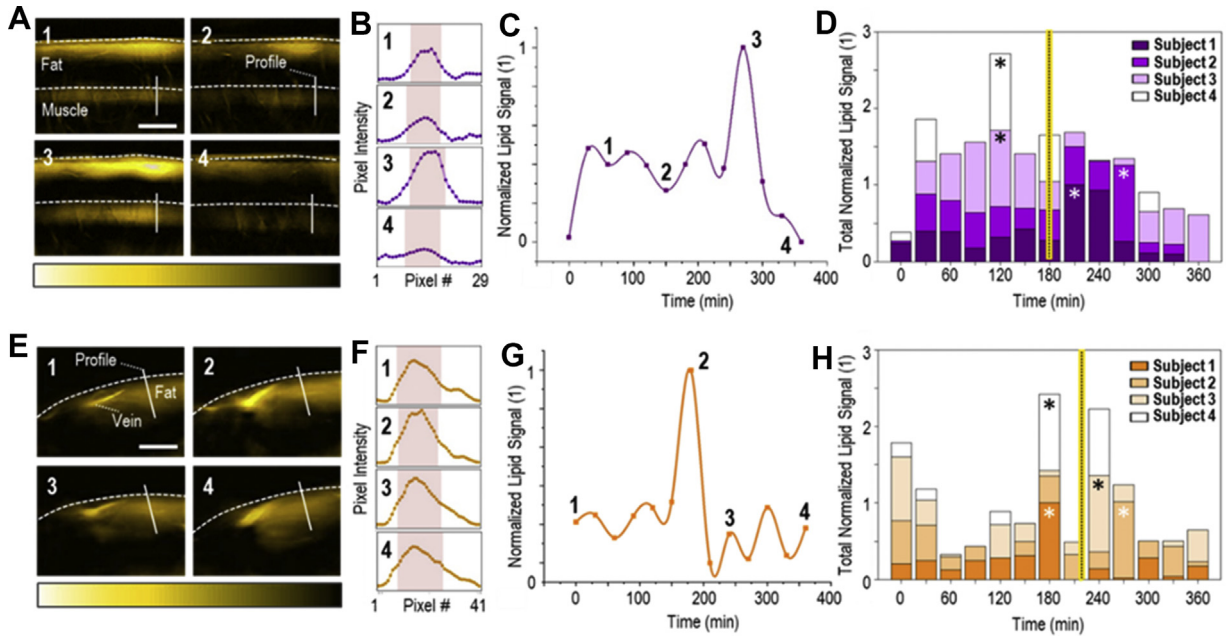

Figure 3: MSOT imaging of lipid dynamics in skeletal muscle and subcutaneous fat. (A) A series of cross-sectional MSOT images of the brachioradialis muscle recorded at 930 nm, which correspond to the four time points indicated in (C) (subject 2). Upper white dashed line: skin surface. Lower white dashed line: upper limit of the muscle region. Scale bars: 1 cm. (B) Pixel-intensity cross-sections along the corresponding profile lines in the image series of Figure 3A. The red bands show the pixel range at 50% of the maximum pixel-intensity value along the profile line. (C) Normalized mean lipid signal within the muscle for subject 2 during the whole postprandial lipemia test. The first time point corresponds to the fasting state. (D) MSOT-extracted lipid dynamics for the brachioradialis muscles of all four subjects. The asterisks indicate the time points of the maximum-recorded value for each subject. The vertical yellow-black line indicates the average time point (among all subjects) after oral loading for the maximum lipid signal within the muscle to be recorded. (E) Cross-sectional MSOT images (at 930 nm) of the forearm subcutaneous fat for the four time points of (G) (subject 1). Upper white dashed line: skin surface. Scale bars: 0.5 cm. (F) Pixel-intensity cross-sections along the profile lines of Figure 3E-image series. Red bands: pixel range at 50% of the maximum pixel-value along the profile line. (G) Postprandial lipid dynamics (normalized) within the subcutaneous fat region for subject 1. (H) MSOT-extracted lipid dynamics for the subcutaneous fat of all subjects. Asterisks: time point of the maximum-recorded value for each subject. The vertical black-yellow line indicates the average recorded time point for the maximum lipid signal within the subcutaneous fat to be recorded.

45 min, subject 3: 78.9 min, subject 4: 57.4 min) of the maximum-value time points throughout the examined anatomic compartments.

4. DISCUSSION

Postprandial lipemia is a dynamic condition characterized by an increase in blood lipid levels after the consumption of a meal compared with relatively stable fasting conditions. Pathological postprandial lipid profiles, in particular prolonged high lipid levels in blood, have been associated with serious diseases, such as diabetes, obesity, and CVD [29]. Thus far, fluctuations of lipid levels in the blood stream have been monitored either by traditional blood sampling, or with non-invasive, but indirect, methods. We have demonstrated herein that a hand-held MSOT can non-invasively visualize and quantify lipid fluctuations in human blood vessels and soft tissues for several hours after the ingestion of a high-fat meal. This technique offers two key advantages over other non-invasive methods for *in vivo* lipid measurements: i) it provides direct lipid-specific molecular information in blood vessels and soft tissues without the need for injected contrast agents; and ii) it has excellent spatial resolution of less than 300 μm for detailed tomographic imaging of *in vivo* lipid distributions over time.

The results of our pilot study demonstrate that MSOT can provide time-resolved data on lipid levels during the postprandial period. Light absorption by lipids reaches its peak in the NIR at 930 nm, and signals recorded by MSOT in tissue upon illumination at this wavelength have been strongly associated with lipid content [25]. Our recordings showed a clear increase in signal intensities within the segmented anatomical compartments of interest (cephalic vein, radial artery, brachioradialis muscle, and subcutaneous fat) approximately 3–4 h on average after the subjects consumed a fatty meal.

Furthermore, MSOT provides direct molecular imaging of lipid dynamics within different anatomic compartments, most importantly within blood, the gold standard for biochemical lipid analysis in clinical settings. Other image-based methods, such as eye image analysis [14], provide an indirect estimation of the circulating lipids based on the lipid deposits on the cornea. The presented analysis of the recorded color images is based on the mean grayscale intensity within the segmented corneal ROI: a feature that may be affected by the ambient light and hinder the image-based differential diagnosis of corneal lipid depositions from other conditions, such as the limbus sign, which indicates calcium and not lipid deposits in the cornea [30]. Nevertheless, the segmentation approach that has been used for the iris outer boundary by means of circle detection [14] could indeed be used for the automatic segmentation of blood vessels in MSOT images [31], a development which is expected to significantly facilitate the analysis process, especially for large datasets. Such an implementation could take place via a more generalized approach by searching for elliptical objects, which largely resemble the shape of vascular cross-sections in tomographic images. Moreover, an ellipse fitting approach for tracking the wall dynamics in the radial artery has already been applied on MSOT data, with good results [18]. Finally, more elaborate statistical and multidimensional image analysis approaches could be applied to both techniques to reveal possibly correlations between the

Table 1 — Postprandial time points of the maximum-recorded lipid signal within the segmented anatomic compartments (cephalic vein, radial artery, skeletal muscle, and subcutaneous fat) for all subjects, as compared to the baseline.

Anatomic Compartment	Subject #	Time of Peak (min)	Relative Increase (%)
Cephalic Vein	1	240	32.1
	2	180	170
	3	90	95.1
	4	240	38.5
	Means	**187.5**	**83.9**
Radial Artery	1	180	46.4
	2	270	0.9
	3	240	69.3
	4	240	136.9
	Means	**232.5**	**63.4**
Skeletal Muscle	1	210	49
	2	270	170.8
	3	120	145.5
	4	120	117.7
	Means	**180**	**120.8**
Subcutaneous Fat	1	180	39.7
	2	270	25
	3	240	11.3
	4	180	55.2
	Means	**217.5**	**32.8**

features extracted in MSOT images and the ones extracted in eye images with regard to postprandial lipemia or relevant conditions, such as the hypercholesterolemia.

The results agree with known postprandial lipid patterns recorded by blood collection [29] and demonstrate the unique capability of MSOT to provide direct and non-invasive monitoring of in *vivo* lipid level fluctuations in the postprandial state without the need for contrast agents. Moreover, although we only acquired data every 30 min for the current study, the high temporal resolution of MSOT (25 Hz) would enable the non-invasive investigation of faster phenomena of lipid kinetics to be explored in future studies.

MSOT also provided high-resolution visualizations of lipids in blood vessels and soft tissues simultaneously, which is enabled by its 2- to 4-cm depth-penetration and approximately 4-cm horizontal field of view. Thus, using MSOT, we were able to detect tissue variations in the occurrence of the highest average postprandial signals. The most intense signals in the cephalic vein and the skeletal muscle were recorded at ~3 h, while the corresponding signals in the radial artery and the subcutaneous fat were recorded at ~ 4 h. To our knowledge, such rich and direct information on lipid dynamics has not been provided before in the literature. The ability to image both the blood circulation (arteries and veins) and soft tissues (adipose tissue and muscle) during dynamic phenomena, such as the postprandial lipemia, may reveal metabolic interactions among the involved compartments and tissue components. Thus, MSOT could ideally help recognize paths that regulate the crosstalk between cardiovascular and metabolic components of human physiology and pathophysiology of diseases, such as obesity, hypertension, and diabetes [32].

The current study introduces MSOT as a powerful tool for the non-invasive monitoring of *in vivo* blood lipid dynamics during the postprandial state. Our results open up new possibilities in the diagnostics and risk assessment of CVD and metabolic disease, especially when the high portability and low complexity of hand-held MSOT is expected to further facilitate its future disseminated use. Furthermore, the unique capability of MSOT technology to provide real-time and label-free visualizations of intra-vascular, intra-muscular, and intra-subcutaneous fat lipid maps renders it an ideal tool for basic and clinical research in the cardio-metabolic field.

The imaging depth of MSOT (2—4 cm) is excellent compared to other optical techniques, but is limited compared to traditional clinical modalities, such as ultrasonography. Nevertheless, in our study, we were able to access key blood vessels and soft tissues within these depth constraints and provide rich information on lipid dynamics in agreement with literature. The consideration of novel light fluence correction models that compensate for intensity attenuation due to scattering and absorption is expected to further improve the precision of MSOT imaging deeper in tissue and widen the range of clinical applications. Furthermore, the development of phantoms and advanced spectral unmixing algorithms [33] will facilitate the direct quantification of lipid concentrations deep within muscle or other soft tissues, rather than only their relative fluctuations. Our aim here was to demonstrate a proof-of-concept via a human pilot study with a small number of healthy participants. More extended studies including larger cohorts of healthy volunteers and patients, and simultaneous blood analyses are needed to further refine the application MSOT to the non-invasive monitoring of lipids.

Most individuals consume at least three meals per day, and each meal is usually consumed before the postprandially high blood lipid levels return to baseline. Consequently, individuals are in a postprandial state for approximately 18 h per day. Thus, the thorough investigation of *in vivo* lipid dynamics with novel methods may give new insights in several fields of basic and clinical cardio-metabolic research. It has been already shown that MSOT can provide precise anatomic, functional and molecular imaging of the vasculature and other soft tissues, such as adipose tissue and skeletal muscles [15,16,18,19]. This unique set of capabilities may facilitate the exploration of hidden mechanisms of cardio-metabolic crosstalk by enabling multifaceted investigations of common cardiovascular and metabolic diseases, such as atherosclerosis, diabetes, and lipid disorders. Further studies will advance hand-held MSOT toward its clinical translation with implications for objective diagnostics and therapy evaluation under patient- and operator-friendly conditions.

5. CONCLUSION

Clinical hand-held MSOT provides great potential to study lipid metabolism in the postprandial state. This unique feature could lead to novel diagnostics and prevention strategies by the label-free and non-invasive detection of lipid-related tissue biomarkers implicated in several cardiometabolic diseases.

AUTHOR CONTRIBUTIONS

Study design: A.K., N.A.F. and V.N.; Measurements: A.K., N.A.F., A.B.M.; Manuscript preparation: all authors; Supervision: J.P., H.H.E., Mi. K., Ma.K., and V.N.

CONFLICT OF INTEREST

V. Ntziachristos has stock/stock options in iThera Medical GmbH. All other authors have no conflicts of interest to declare.

ACKNOWLEDGEMENTS

This project has received funding from the European Research Council (ERC) under the European Union's Horizon 2020 research and innovation program under grant agreement No 694968 (PREMSOT) and was supported by the DZHK (German Centre for Cardiovascular Research) and by the BMBF (German Ministry of Education and

Research) and by the Helmholtz Zentrum München, funding program "Physician Scientists for Groundbreaking Projects". We thank Dr. Robert Wilson for his attentive reading and improvements of the manuscript.

REFERENCES

[1] Castelli, W.P., Anderson, K., Wilson, P.W., Levy, D., et al., 1992. Lipids and risk of coronary heart disease. The Framingham Study. Annals of Epidemiology 2(1—2):23—28.

[2] Higgins, V., Adeli, K., 2017. Postprandial dyslipidemia: pathophysiology and cardiovascular disease risk assessment. EJIFCC. p. 168—84.

[3] Kats, D., Sharrett, R.A., Ginsberg, H.N., Nambi, V., Ballantyne, C.M., Hoogeveen, R.C., et al., 2017. Postprandial lipemia and the risk of coronary heart disease and stroke: the Atherosclerosis Risk in Communities (ARIC) Study. BMJ open diabetes res care.

[4] Aday, A.W., Sharrett, R.A., Ginsberg, H.N., Nambi, V., Ballantyne, C.M., Hoogeveen, R.C., 2018. Lipoprotein particle profiles, standard lipids, and peripheral artery disease incidence.

[5] Klop, B., Elte, J.W.F., Castro Cabezas, M., 2013. Dyslipidemia in obesity: mechanisms and potential targets. Nutrients 5(4):1218—1240.

[6] Pastromas, S., Terzi, A.B., Tousoulis, D., Koulouris, S., et al., 2008. Postprandial lipemia: an under-recognized atherogenic factor in patients with diabetes mellitus. International Journal of Cardiology 126(1):3—12.

[7] Matikainen, N., Mänttäri, S., Westerbacka, J., Vehkavaara, S., Lundbom, N., Yki-Järvinen, H., et al., 2019. Postprandial lipemia associates with liver fat content. Journal of Clinical Endocrinology & Metabolism 92(8):3052—3059.

[8] Nordestgaard, B.G., Langsted, A., Mora, S., Kolovou, G., Baum, H., Bruckert, E., et al., 2016. Fasting is not routinely required for determination of a lipid profile: clinical and laboratory implications including flagging at desirable concentration cut-points-a joint consensus statement from the European Atherosclerosis Society and European Federation of Clinical Chemistry and Laboratory Medicine. European Heart Journal 37(25):1944—1958.

[9] Langsted, A., Freiberg, J.J., Nordestgaard, B.G., 2008. Fasting and nonfasting lipid levels: influence of normal food intake on lipids, lipoproteins, apolipoproteins, and cardiovascular risk prediction. Circulation 118(20): 2047—2056.

[10] Langsted, A., Nordestgaard, B.G., 2019. Nonfasting versus fasting lipid profile for cardiovascular risk prediction. Pathology 51(2):131—141.

[11] Mora, S., Chang, C.L., Moorthy, M.V., Sever, P.S., et al., 2019. Association of nonfasting vs fasting lipid levels with risk of major coronary events in the anglo-scandinavian cardiac outcomes trial-lipid lowering arm. JAMA Intern Med 179(7):898—905.

[12] National Clinical Guideline, C., 2014. National institute for health and clinical excellence: guidance. Lipid modification: cardiovascular risk assessment and the modification of blood lipids for the primary and secondary prevention of cardiovascular disease. London: National Institute for Health and Care Excellence (UK)Copyright (c) National Clinical Guideline Centre, 2014.

[13] Minh, T.D.C., Oliver, S.R., Flores, R.L., Ngo, J., Meinardi, S., Carlson, M.K., et al., 2012. Noninvasive measurement of plasma triglycerides and free fatty acids from exhaled breath. J Diabetes Sci Technol 6(1):86—101.

[14] Mahesh, S., Gunasundari, R., Ezhilvathani, N., 2016. Non-invasive measurement of cholesterol levels using eye image analysis. International conference on advances in computational intelligence and communication. CIC).

[15] Taruttis, A., Ntziachristos, V., 2015. Advances in real-time multispectral optoacoustic imaging and its applications. Nature Photonics 9:219—227.

[16] Reber, J., Willershäuser, M., Karlas, A., Paul-Yuan, K., Diot, G., Franz, D., et al., 2018. Non-invasive measurement of Brown fat metabolism based on optoacoustic imaging of hemoglobin gradients. Cell Metabolism 27(3):689—701 e4.

[17] Buehler, A., Diot, G., Volz, T., Kohlmeyer, J., Ntziachristos, V., et al., 2017. Imaging of fatty tumors: appearance of subcutaneous lipomas in optoacoustic images. Journal of Biophotonics 10(8):983—989.

[18] Karlas, A., Reber, J., Diot, G., Bozhko, D., Anastasopoulou, M., Ibrahim, T., et al., 2017. Flow-mediated dilatation test using optoacoustic imaging: a proof-of-concept. Biomedical Optics Express 8(7):3395—3403.

[19] Karlas, A., Kallmayer, M., Fasoula, N.A., Liapis, E., Bariotakis, M., Krönke, M., et al., 2020. Multispectral optoacoustic tomography of muscle perfusion and oxygenation under arterial and venous occlusion - a human pilot study. Journal of Biophotonics 13(6):e201960169.

[20] Yang, H., Jüstel, D., Prakash, J., Karlas, A., Helfen, A., Masthoff, M., et al., 2020. Soft ultrasound priors in optoacoustic reconstruction: improving clinical vascular imaging. Photoacoustics 19:100172.

[21] Chowdhury, K.B., Prakash, J., Karlas, A., Jüstel, D., Ntziachristos, V., et al., 2020. A synthetic total impulse response characterization method for correction of hand-held optoacoustic images. IEEE Transactions on Medical Imaging 39(6):3218—3230.

[22] Karlas, A., Masthoff, M., Kallmayer, M., Helfen, A., Bariotakis, M., Fasoula, N.A., et al., 2020. Multispectral optoacoustic tomography of peripheral arterial disease based on muscle hemoglobin gradients—a pilot clinical study. Annals of Translational Medicine 9(1):36 [Publish ahead of print].

[23] Karlas, A., Reber, J., Liapis, E., Paul-Yuan, K., Ntziachristos, V., et al., 2019. Multispectral optoacoustic tomography of Brown adipose tissue. Handbook of Experimental Pharmacology 251:325—336.

[24] Li, Y., Schnabl, K., Gabler, S.M., Willershäuser, M., Reber, J., Karlas, A., et al., 2018. Secretin-activated Brown fat mediates prandial thermogenesis to induce satiation. Cell 175(6):1561—1574 e12.

[25] Karlas, A., Fasoula, N.A., Paul-Yuan, K., Reber, J., Kallmayer, M., Bozhko, D., et al., 2019. Cardiovascular optoacoustics: from mice to men - a review. Photoacoustics 14:19—30.

[26] Umpaichitra, V., Banerji, M.A., Castells, S., 2004. Postprandial hyperlipidemia after a fat loading test in minority adolescents with type 2 diabetes mellitus and obesity. Journal of Pediatric Endocrinology & Metabolism 17(6):853—864.

[27] America, T.L.I.o., 2000. American national standards for the safe use of lasers. In: ANSI Z136.1.

[28] Rosenthal, A., Ntziachristos, V., Razansky, D., 2011. Model-based optoacoustic inversion with arbitrary-shape detectors. Medical Physics 38(7):4285—4295.

[29] Lambert, J.E., Parks, E.J., 2012. Postprandial metabolism of meal triglyceride in humans*,**. Biochimica et Biophysica Acta 1821(5):721—726.

[30] Munjal, A., Kaufman, E.J., 2020. Arcus senilis. StatPearls. Treasure Island (FL: StatPearls Publishing LLC.

[31] Chlis, N.K., Karlas, A., Fasoula, N.A., Kallmayer, M., Eckstein, H.H., Theis, F.J., et al., 2020. A sparse deep learning approach for automatic segmentation of human vasculature in multispectral optoacoustic tomography. Photoacoustics 20:100203.

[32] Jordan, J., Birkenfeld, A.L., 2016. Cardiometabolic crosstalk in obesity-associated arterial hypertension. Reviews in Endocrine & Metabolic Disorders 17(1):19—28.

[33] Tzoumas, S., Nunes, A., Olefir, I., Stangl, S., Symvoulidis, P., Glasl, S., et al., 2016. Eigenspectra optoacoustic tomography achieves quantitative blood oxygenation imaging deep in tissues. Nature Communications 7:12121.

Appendix B

Publication: Non-invasive multispectral optoacoustic tomography resolves intrahepatic lipids in patients with hepatic steatosis

The version herein has been published in the journal "Photoacoustics" [58].

Photoacoustics 29 (2023) 100454

Contents lists available at ScienceDirect

Photoacoustics

journal homepage: www.elsevier.com/locate/pacs

Non-invasive multispectral optoacoustic tomography resolves intrahepatic lipids in patients with hepatic steatosis

Nikolina-Alexia Fasoula [a,b,1], Angelos Karlas [a,b,c,d,1], Olga Prokopchuk [e], Nikoletta Katsouli [a,b], Michail Bariotakis [a,b], Evangelos Liapis [a,b], Anna Goetz [f], Michael Kallmayer [c], Josefine Reber [a,b], Alexander Novotny [e], Helmut Friess [e], Marc Ringelhan [g], Roland Schmid [g], Hans-Henning Eckstein [c,d], Susanna Hofmann [f,h], Vasilis Ntziachristos [a,b,d,*]

[a] Chair of Biological Imaging at the Central Institute for Translational Cancer Research (TranslaTUM), School of Medicine, Technical University of Munich, Germany
[b] Institute of Biological and Medical Imaging, Helmholtz Zentrum München, Neuherberg, Germany
[c] Department for Vascular and Endovascular Surgery, Klinikum rechts der Isar, Technical University of Munich, Munich, Germany
[d] DZHK (German Centre for Cardiovascular Research), partner Site Munich Heart Alliance, Munich, Germany
[e] Department of Visceral Surgery, Klinikum rechts der Isar, Munich, Germany
[f] Institute for Diabetes and Regeneration Research, Helmholtz Zentrum München, Neuherberg, Germany
[g] Department of Internal Medicine II, Klinikum rechts der Isar, Technical University of Munich, Munich, Germany
[h] Department of Internal Medicine IV, Klinikum der Ludwig Maximilian University of Munich, Munich, Germany

ARTICLE INFO

Keywords:
Photoacoustics
MSOT
Lipid imaging
Non-alcoholic fatty liver disease
NAFLD
Molecular imaging
Metabolism

ABSTRACT

Hepatic steatosis is characterized by intrahepatic lipid accumulation and may lead to irreversible liver damage if untreated. Here, we investigate whether multispectral optoacoustic tomography (MSOT) can offer label-free detection of liver lipid content to enable non-invasive characterization of hepatic steatosis by analyzing the spectral region around 930 nm, where lipids characteristically absorb. In a pilot study, we apply MSOT to measure liver and surrounding tissues in five patients with liver steatosis and five healthy volunteers, revealing significantly higher absorptions at 930 nm in the patients, while no significant difference was observed in the subcutaneous adipose tissue of the two groups. We further corroborated the human observations with corresponding MSOT measurements in high fat diet (HFD) - and regular chow diet (CD)-fed mice. This study introduces MSOT as a potential non-invasive and portable technique for detecting/monitoring hepatic steatosis in clinical settings, providing justification for larger studies.

1. Introduction

Hepatic steatosis is a benign condition associated with chronic inflammation and may lead to non-alcoholic steatohepatitis (NASH), fibrosis [1–3], cirrhosis, or liver cancer [4,5]. There is therefore a need to swiftly assess steatosis to prompt early interventions, such as dietary and lifestyle changes or drug treatments, as well as to assess the efficacy of these interventions [6].

Today, monitoring of hepatic steatosis is primarily based on liver biopsies [7], which are analyzed for lipid content [3,8]. However, biopsies are limited by their invasive nature, pain, and overall patient inconvenience and are not appropriate for disseminated observations or longitudinal monitoring. Moreover, biopsies are prone to sampling errors, may lead to complications, such as hemorrhages [8], and come with considerable cost when considering the time and infrastructure required for a diagnostic test. With steatosis becoming more prevalent worldwide as obesity rates increase, there is a clear need for non-invasive lipid assessment in liver [6].

Imaging techniques have been considered for the non-invasive assessment of liver lipid content [9,10]. X-ray computed tomography (CT) can resolve and quantify intrahepatic lipids and allow for staging of hepatic steatosis but is characterized by low sensitivity in mild cases [11] and uses ionizing radiation that limits frequent monitoring. Magnetic resonance (MR) imaging and spectroscopy techniques offer higher sensitivity and specificity in assessing hepatic steatosis, without using ionizing radiation [11–13]. Conversely, MR techniques require

* Correspondence to: Chair of Biological Imaging, Technical University of Munich, School of Medicine, Ismaninger Str. 22, Munich, Bavaria DE 81675, Germany.
E-mail address: bioimaging.translatum@tum.de (V. Ntziachristos).
[1] These authors contributed equally to this work.

https://doi.org/10.1016/j.pacs.2023.100454
Received 21 July 2022; Received in revised form 12 January 2023; Accepted 18 January 2023
Available online 20 January 2023

expensive and low-throughput infrastructure that is not appropriate for disseminated use.

Ultrasound (US) based techniques have been considered as a portable and low-cost alternative for assessing lipid content. While conventional ultrasonography is not sensitive to lipids [9], indirect measurements of mechanical properties using ultrasound elastography (USE) have shown potential to provide a surrogate marker for steatosis, as they associate with stiffness changes due to lipid accumulation [9,10,13–15]. In particular, controlled attenuation parameter ultrasound (CAP-US) has been studied for diagnosing hepatic steatosis, achieving detection sensitivity in the 80% range, but possibly with performance that is operator - dependent [16,17]. Nevertheless, stiffness is not a parameter that is lipid specific and may be affected also by other pathologies, limiting the wide application of CAP-US in the general population.

Optoacoustic imaging resolves optical contrast in tissue with resolutions that are similar to ultrasonography. Multispectral optoacoustic tomography (MSOT) is a portable and non-invasive technique that has been employed to visualize hemodynamics, tissue oxygenation, and inflammation in humans and animals using illumination wavelengths between 700 and 900 nm [18–26]. Nevertheless, recent observations indicate that in vivo visualization of lipids is possible with MSOT by illumination on or around 930 nm [21,23,26–28], where lipids exhibit a characteristic strong absorption peak. Since previous publication has already presented a histological validation of MSOT imaging of hepatic steatosis in mice [29], extending lipid-detection with MSOT to the human liver could significantly impact the monitoring and management of hepatic steatosis in humans by potentially allowing frequent, non-invasive assessment of the liver's lipid content. However, reliable detection of lipids in the liver would require penetration depths of a few centimeters, despite the organ being surrounded by deformable tissues.

Here, we present a pilot study to examine whether MSOT can detect lipids at such depths within the human liver by their strong absorption around 930 nm. To this end, we employed a hybrid MSOT–US modality and developed an imaging protocol and data analysis methodology that leverages the availability of ultrasound images co-registered with optoacoustic images to offer image-guided recording of multispectral data from the liver. This feature allows for accurate comparisons of the absorption spectra in the near infrared (NIR, 700–970 nm) between subjects, from the liver and the overlying subcutaneous fat (SAT). A particular feature of the data analysis protocol used herein is the use of the SAT spectrum as a reference spectrum to account for system variations and depth-dependent attenuation effects on the spectra collected from the liver, thereby increasing the accuracy of the observation.

To further investigate the accuracy and validity of the approach, we conducted a control study in animals, using mice with induced steatosis and healthy mice. The goal of the animal study was to validate the spectral features obtained from different depths in humans using signals from more shallow depths, i.e., using measurements that are not affected by the signal dependence of the optoacoustic measurement to depth, due to light attenuation. In both human and animal studies we observed strong optoacoustic signals at 930 nm for the lipid-rich tissue compartments, such as SAT, confirming that the 930 nm peak can be used for examining lipid content in human liver and that depth dependent attenuation did not significantly affect the spectral appearance of the data collected. In contrast, the 930 nm peak was not prominent in the livers of healthy mice and healthy volunteers. Therefore, the investigation gives preliminary support to MSOT detecting elevated lipid levels in the livers of patients with hepatic steatosis, setting the stage for larger clinical studies.

2. Methods

2.1. Human imaging

Five patients with previously diagnosed liver steatosis ($n_1 = 5$, 3 males and 2 females, mean age 58, range 46–61, mean BMI= 27.5 kg/m^2, range 21.5–32) were included in this pilot study. Liver steatosis in the patients was diagnosed using ultrasound imaging, CT, and visual inspection of the liver during an open abdominal surgery. Two out of the five patients had grade 2 liver steatosis while the other three patients had grade 3.

Two out of five patients were overweight (BMI $>$ 25 kg/m^2) and two of them had class I obesity (BMI $>$ 30 kg/m^2). Three patients had a history of hyperlipidemia, two patients had a history of hypertension, and one patient had type 2 diabetes.

Both diagnosis and grading of liver steatosis was performed using ultrasound features that include liver brightness, contrast differences between the liver and the kidney, ultrasound appearance of the intrahepatic vessels, liver parenchyma and diaphragm [30,31]. Since ultrasonography provides nowadays accurate detection of moderate to severe hepatic steatosis [30], an additional biopsy was not necessary. Moreover, in one out of five patients, hepatic steatosis was primarily diagnosed during open abdominal surgery (esophagectomy for adenocarcinoma of the esophagogastric junction) and described macroscopically as severe liver steatosis. In the other four patients included, hepatic steatosis was primarily diagnosed by a primary care physician and validated after inclusion in this study. In two patients, liver steatosis was additionally described in CT.

Additionally, five healthy volunteers ($n_2 = 5$, 3 males and 2 females, mean age 31, range 24–38 mean BMI= 20.5 kg/m^2, range 19.7–21.6), were recruited as control subjects. All volunteers were non-smokers and had no history of cardiovascular or metabolic disease. Participants signed an informed consent form prior to enrollment in the study, which was approved by the ethics committee of the medical faculty of the Technical University of Munich (Protocol No 520/19 S).

Optoacoustic scans took place in a quiet room with a normal room temperature (≈23 °C). Subjects were asked not to consume any food, alcohol, or caffeine for 8 h before the MSOT examination. Both participants and examiners wore laser safety goggles. All participants were asked to lie in a supine position. For both patients and healthy volunteers, the hand-held scanning probe was placed over the right hypochondriac region in a transversal position identified by anatomic knowledge under real-time ultrasound imaging (Fig. 1). Each scan lasted for approximately 60 s. The total duration of the MSOT examinations was approximately 5 min (patient and system preparation included), comparable to standard ultrasound examinations. This hand-held MSOT is capable of imaging up to depths of approximately 3–4 cm, which is sufficient to reach the liver.

2.2. Animal imaging

The Government of Upper Bavaria approved all procedures involving animal experiments. To induce substantial obesity and steatosis, mice ($n_3 = 5$ B6 (Cg)-Tyr$^{c\text{-}2\,J}$/J, 3 males and 2 females; Charles River, River Laboratories, Wilmington, MA, USA) were fed with a high-fat, high-sugar diet (HFD) comprising 58% kcal from fat (D12331; Research Diets, New Brunswick, NJ, USA) for 20 weeks. Another age-matched cohort of mice ($n_4 = 5$ B6 (Cg)-Tyr$^{c\text{-}2\,J}$/J, 2 males and 3 females) were fed a regular chow diet (CD) as a control. The mice were housed on a 12:12–h light–dark cycle at 22 °C with free access to water and food.

All animals were anesthetized by inhalation of 2% isoflurane (Zoetis GmbH, Berlin, Germany) delivered in combination with oxygen. Animals were positioned in the MSOT machine according to a standard measurement protocol [20]; after being placed into a thin and transparent polyethylene membrane, the mice were submerged in a water bath of 34 °C. The water ensures acoustic coupling and a stable body temperature. In vivo scans were conducted using an MSOT device tailored for small animal imaging described below [20]. Each mouse MSOT scan lasted for approximately 11 min recording data at many different positions along the long axis of the animal over the thorax and abdomen regions.

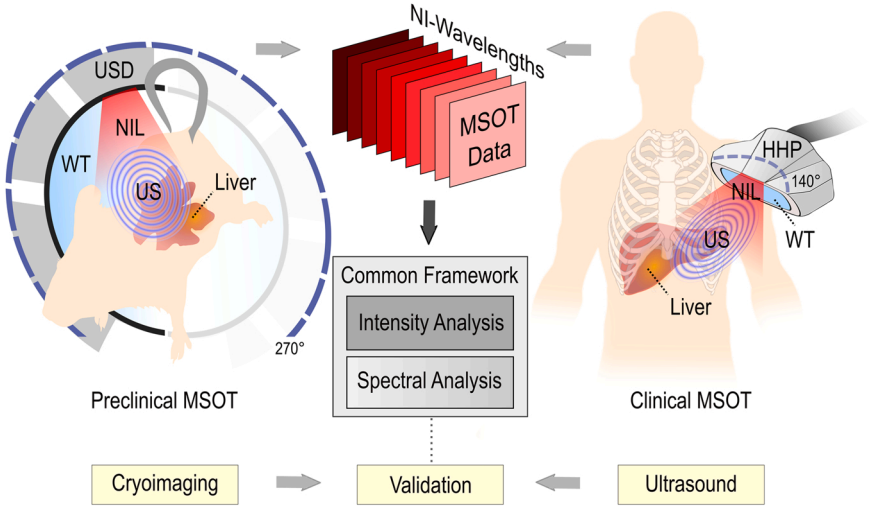

Fig. 1. MSOT principle of operation and common analysis framework. Left: Preclinical MSOT imaging of the liver and validation by cryoimaging. Right: Clinical MSOT imaging of the liver and validation by ultrasound. The common analysis framework includes the intensity and spectral analysis. USD: Ultrasound detector, NIL: Near-infrared light, US: Ultrasound, WT: Water tank, HHP: Hand-held probe, NI: Near-infrared. The coverage angle in preclinical MSOT is 270° and in hand-held clinical MSOT 140°.

MSOT recordings were anatomically validated via cryoimaging, which was carried out after euthanizing the animals and freezing them to − 50 °C. The mice were next embedded in optimal cutting temperature compound (O.C.T, Tissue Teck, Sakura Finetek, USA) and transversely cryosliced at steps of 50 μm along their long axis using a customized cryoimaging system. The latter consisted of a commercial cryotome (CM 1950, Leica microsystems, Germany) equipped with a CCD camera (AndorLucaR© CCD camera (DL-604 M, Andor Technology, Belfast, UK), which recorded one RGB color image of the mouse cross-section after each slicing step. Acquired images were further processed (denoising, contrast enhancement, and geometric transformation) for visualization purposes.

2.3. Hand-held MSOT/US and mouse MSOT systems

MSOT scans of patients were conducted using a clinical hand-held MSOT-Ultrasound system (MSOT Acuity Echo©, iThera Medical GmbH, Munich, Germany) equipped with a handheld scanning probe. Briefly, the custom-built hand-held MSOT system is capable of acquiring real time optoacoustic images at a frame rate of 25 Hz and co-registered US images at a frame rate of approximately 9 Hz. The hand-held probe is enclosed within a light-weight 3D-printed casing and is equipped with 256 piezoelectric elements with a central frequency of 4 MHz arranged in an arc of 145° for ultrasound detection. The cavity between the half-arc detector and specimen was filled with heavy water (D_2O), which absorbs less light in the near-infrared range compared to normal water, while providing ideal coupling with the ultrasound transducer. Illumination was delivered in the form of short light pulses (approximately 10 ns in duration), at a rate of 25 Hz. For each pulse, almost 15 mJ of energy were delivered over a rectangular area of around 1 × 4 cm, which is well below the safety limits of laser use for medical applications [32]. For multispectral imaging, we acquired images at 28 different wavelengths (from 700 to 970 nm, 10 nm steps). While the 900–970 nm region was used to detect lipids, the spectral information in the 700–900 nm range was useful for identifying strongly absorbing structures such as large vessels that might obscure tissues of interest.

Live mice were scanned using a small animal MSOT device (inVision© 256-TF, iThera Medical GmbH, Munich, Germany). Technical details of the device have been described elsewhere [20]. In brief, mice were illuminated with near-infrared light pulses of 29 different wavelengths (680–960 nm at steps of 10 nm) at a repetition rate of 10 Hz and with pulse energy of approximately 80 mJ. A fiber bundle splitting configuration with multiple outputs ensured homogenous ring-shaped line illumination around the mouse body (Fig. 1). The ultrasound waves produced upon pulsed illumination were recorded by means of a 256-element-array of piezoelectric ultrasound detectors, covering an angle of 270° around the animal. A moving stage mechanism enabled the acquisition of full-thickness tomographic images of the mouse body at several positions along its long axis. Each scan included the recording (and averaging) of 10 frames at each of 23 different positions along the animal.

The employed human and mouse MSOT systems are based on the same principle of operation (single-pulse-per-frame, SPPF) providing tomographic images of the examined anatomic regions. As described above, the delivery of illumination and ultrasound detector arrays differ between the two setups, providing high adaptability and flexibility to the user depending upon application. In specific, the mouse system employs mechanical stages for scanning different parts of the animal while the hand-held configuration of the human system enables the examination of different body regions.

All acquired optoacoustic datasets were reconstructed using a model-based reconstruction algorithm developed in previous work [33] with non-negativity constraint, as usual in such studies.

2.4. Optoacoustic data analysis

The two systems employed herein share the engine and, after image acquisition, a common methodology was applied for data analysis in both humans and mice. Our analysis included the 29 wavelengths from 680 to 960 nm at steps of 10 nm for the mouse dataset and the 28 wavelengths from 700 to 970 nm at steps of 10 nm for the clinical dataset. A single characteristic set of 29 or 28 single-wavelength images, known as a ‘multispectral stack’, was selected for each mouse or human subject for further analysis. The selection criteria were an absence of motion and high image quality. Three different regions of interest (ROIs) based on the anatomical location in the co-registered ultrasound images were manually delineated for each multispectral stack: i) the liver region, ii) the subcutaneous fat (SAT) region, and iii) the entire imaged tissue region. The latter ROI included both the liver and SAT regions and was taken as the ‘background region’ (BGR) for each recorded image. The ROIs in the mouse data were manually segmented in consultation with two biologists with extensive experience in MSOT mouse imaging. The ROIs in the human data were manually segmented using both ultrasound data and in consultation with two clinicians with experience in clinical MSOT imaging.

As a next step, we adjusted the measured optoacoustic signals within the liver to account for differences arising from either i) exogenous factors, such as normal fluctuations of the laser energy per pulse or ii) subject-dependent factors, such as variations in the thickness, type, and perfusion of tissue layers in the scanned region. This adjustment was

accomplished by first calculating the mean pixel intensity within the liver ROI and the BGR for the selected 29 (mouse) or 28 (human) single-wavelength images of all subjects. Then, the ROI/BGR ratio of the calculated mean values was extracted for each single-wavelength image. The extracted ratios were normalized against the maximum ratio value of each selected multispectral stack in order to fall within the range of [0,1]. By plotting the normalized ROI/BGR ratios for the measured wavelengths, we calculated for each subject a 'normalized ratio spectrum' in the NIR, which provided a common reference for all subjects and yielded comparable results. Next, the per-subject normalized ratio spectra were used to estimate the 'mean' normalized ratio spectra within the SAT and liver ROIs for the healthy and steatosis group in both mice and humans.

Furthermore, we compared the mean of the ROI/BGR ratio at 930 nm between the two groups (healthy and steatosis) in mice and humans to investigate possible correlations between the preclinical and clinical MSOT data of hepatic steatosis. This wavelength was chosen because it is where lipid absorption is highest in the NIR. The mean of the ROI/BGR ratio at 930 nm in healthy subjects and the same mean value in subjects with hepatic steatosis were compared using unpaired t-tests, since samples conformed to a normal distribution, as indicated by Shapiro-Wilk tests.

To further evaluate and quantify the capability of MSOT to detect liver steatosis at high, usual for human imaging, depths of several centimeters (> 2–3 cm) we performed a SNR analysis with increasing depth in the human MSOT data. To this end, the manually segmented liver regions in the 930 nm-MSOT images were further divided in 5 mm-thick horizontal segments and the SNR was calculated within the SAT segment and the resulted 5 mm-thick liver segments for all subjects (patients and healthy volunteers). The SNR for each segment at the various depths was calculated as the mean optoacoustic signal of the segment divided by the standard deviation of the noise, or else the signal measured within the region above the skin line in each image which corresponds to the water tank of the hand-held MSOT probe.

Data processing and statistical analysis, including the creation of figures, was performed with MATLAB (R2019a, MathWorks, 2019, Inc., Massachusetts, United States) and R (version 3.6.0, R Core Team, 2019, Vienna, Austria). The results are reported as the mean ± standard error of the mean. We also report p-values and effect sizes of the relative statistical tests.

3. Results

We first conducted targeted human MSOT measurements to explore the capability of MSOT to resolve lipids at the depths of the human liver in patients with previously diagnosed hepatic steatosis. Fig. 2 depicts MSOT imaging and subsequent analysis of the livers of five patients and five healthy volunteers. Fig. 2a shows an exemplary US frame recorded over the hypochondriac region of a healthy volunteer. The corresponding and coregistered MSOT image at 930 nm is provided in Fig. 2b. Likewise, Fig. 2c-d show the US and MSOT images of the same anatomic region of a patient with diagnosed hepatic steatosis. Both the SAT and liver regions are clearly delineated (dashed line/manually) in both the healthy volunteer and the patient based on the local anatomy. Two differences are apparent between the patient and the healthy volunteer: i) the lipid signal is stronger within the delineated liver region of the 'steatosis' patient compared to the healthy volunteer and ii) the SAT layer is thicker in the 'steatosis' patient.

To explore the capability of MSOT to detect lipids in human soft tissues, we analysed the high-lipid-content SAT layer. Fig. 2e-h summarize our analysis for the SAT regions of the patients and healthy volunteers. The exemplary normalized ratio spectra of both a healthy volunteer and a patient with liver steatosis feature prominent absorption-peaks at 930 nm (Fig. 2e-f). The similarity in the spectra of the SAT layers between the two groups is further apparent in the statistical analyses of the normalized ratio spectra (Fig. 2g). Furthermore,

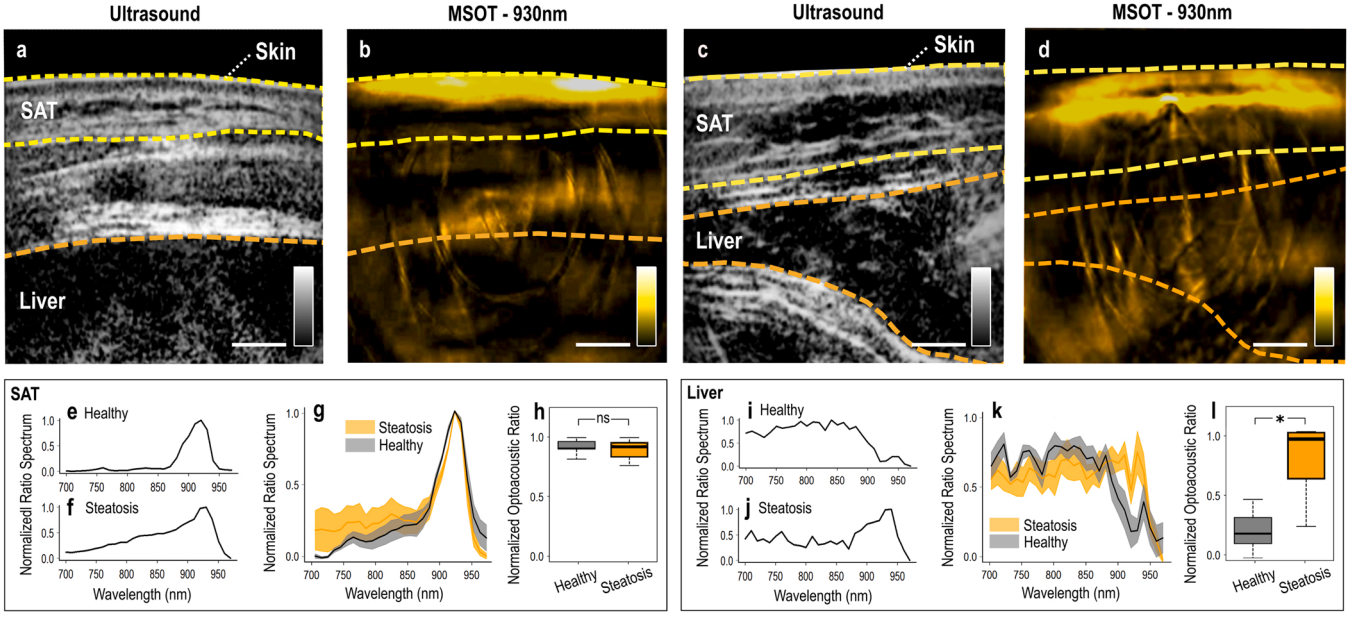

Fig. 2. Human hand-held MSOT imaging and data analysis. (a) US image over the hypochondriac region of a healthy volunteer. (b) MSOT image recorded at 930 nm of the hypochondriac region of the same healthy volunteer. (c) US image of the liver of a patient with liver steatosis. (d) 930 nm-MSOT image of the same region of the patient. In (a)-(d): The dashed yellow lines delineate the skin/SAT layers and the dashed orange lines the liver region. (e-f) Normalized ROI/BGR ratio spectrum within the SAT region for a healthy volunteer and a patient with steatosis. (g) Mean (± standard error of the mean) normalized ROI/BGR ratio spectra for the whole cohort of healthy subjects (gray) and patients (orange). (h) Normalized ROI/BGR mean pixel intensity ratio at 930 nm within the SAT region for healthy volunteers (gray) and patients (orange). (i-j) Normalized ROI/BGR ratio spectrum within the liver region of a healthy volunteer (gray) and a patient (orange). (k) Mean (± standard error of the mean) normalized ROI/BGR ratio spectra for the whole cohort of healthy volunteers (gray) and patients (orange). (l) Normalized ROI/BGR mean pixel intensity ratio at 930 nm within the liver region of healthy subjects (gray) and patients with liver steatosis (orange). ns = non statistically significant, *$p < 0.05$.

the normalized ROI/BGR ratios within the SAT region for the whole groups of healthy volunteers and hepatic steatosis patients are not significantly different (Fig. 2h; healthy volunteers 0.92 ± 0.031 vs. steatosis patients 0.9 ± 0.043, p-value $= 0.6746$, Cohen's d $= 0.27$). Thus, as expected, MSOT is able to detect high levels of lipid signals within the SAT region in both healthy volunteers and patients with hepatic steatosis.

As a next step, we used the same principle and analysis to investigate the capability of MSOT to detect lipids within the liver region in patients with diagnosed hepatic steatosis. Fig. 2i-l illustrate the spectral analysis of the MSOT measurements of the liver regions for both healthy volunteers and patients. Comparison of exemplary normalized ratio spectra reveals higher absorption at 930 nm in the liver of the steatosis patient compared to that of the healthy volunteer, corresponding to the greater lipid content of the steatotic liver (Fig. 2i-j). Fig. 2k depicts the mean normalized ratio spectra for the whole 'healthy' and 'steatosis' human groups; the lipid-peak at 930 nm is again prominent. Moreover, the ROI/BGR ratio at 930 nm within the liver region was significantly higher in the liver steatosis group compared to the group of healthy volunteers (0.762 ± 0.146 vs. 0.219 ± 0.081, p-value $= 0.011$, Cohen's d $= 2.07$).

To confirm the capability of MSOT to resolve lipids at imaging depths of several centimeters, we analysed the effect of depth on the SNR of the signal at 930 nm from the human MSOT data (Fig. 3). Our results show a steep SNR-decrease of the 83% from the SAT (0.4 cm depth) to the first liver segment (2.5 cm depth) and a subsequent mean decrease of 24.3% for every 5 mm along the liver segments. In total, we observe an average decrease of $\approx 15\%$ for every centimeter of depth, with a recorded SNR of 4.97 at a depth of 3.4 cm within the liver (Fig. 3a). However, the SNR at 3.4 cm is sufficient to distinguish the lipid signal from the background noise, demonstrating that MSOT is capable of detecting lipid-specific optoacoustic signals at the average depths of the human liver.

To go beyond bulk tissue analyses and gain insight into the measured OA signal within the liver at the single-pixel level, we conducted an additional statistical analysis of the pixels from the liver areas for both healthy volunteers and patients with liver steatosis. Plotting the density of OA signal intensities at 930 nm for all pixels inside the liver ROI revealed divergent distributions of OA signal intensities between the healthy volunteers and patients (Fig. 3b). In particular, the distribution within the steatosis group featured a notable tail towards higher signal intensities, suggesting the association of this subset of pixels with areas of increased lipid content. Finally, based on the presented histogram, a threshold was selected at the point of intersection between the two curves, and the proportion of pixels above this threshold was calculated for each subject. The proportion of pixels above the selected threshold was found to be significantly higher (the respective proportions test yielded a p-value < 0.001) in the patient group compared to the healthy volunteers (Fig. 3c).

To further validate the efficacy of our method for detecting hepatic steatosis in humans, we performed experiments in mice, where signal attenuation due to tissue absorption is minimal because of the shallower imaging depths. Scanned mice were either CD-fed (controls) or HFD-fed (expected to develop hepatic steatosis). Fig. 4 shows images and analyses from MSOT measurements of the mice livers and the surrounding SAT regions. Fig. 4a-d compare exemplary cryoimages and MSOT images for both a control CD-fed mouse (Fig. 4a-b) and an HFD-fed mouse with liver steatosis (Fig. 4c-d). The MSOT images shown were recorded at 930 nm, where lipids absorption is the highest. Dashed orange lines delineate the liver while dashed yellow lines delineate the SAT regions. A clear difference is visible in the size of the two mice, with the HFD-fed mouse being larger in cross-sectional diameter than the CD-fed one. This increase in size is mainly the result of an increase in the size of the SAT layer, rather than the liver. However, the optoacoustic signal intensity within the liver is visually higher in the liver of the HFD-fed mouse compared to the CD-fed control.

Spectral analysis did not indicate a significant difference in the lipid content of the SAT regions between the HFD-fed and CD-fed mice (Fig. 4e-h). Fig. 4e-f display characteristic normalized ratio spectra (680–960 nm) from the SAT regions of a 'healthy' mouse (Fig. 4e) and a 'steatosis' (Fig. 4f) mouse. The spectra are qualitatively similar, with both containing a prominent absorption peak at 930 nm, as expected for the high-lipid-content SAT region. Fig. 4g shows the mean normalized ratio spectra for the whole mouse cohort of $n_4 = 5$ CD-fed healthy controls (black line) and $n_3 = 5$ HFD-fed steatosis (yellow line) mice, where the peak at 930 nm is again prominent for both groups. Finally, Fig. 4h depicts the statistical analysis for the normalized ROI/BGR intensity-based ratio at 930 nm within the SAT region. The difference between the 'liver steatosis' and the 'healthy' mice groups were, as expected, not significant (0.724 ± 0.136 for HFD-fed mice vs. 0.705 ± 0.133 for CD-fed mice, p-value $= 0.923$, Cohen's d $= 0.06$).

A similar analysis of the MSOT data from the liver region (Fig. 4i-l) reveals significant lipid accumulation in the livers of the HFD-fed mice compared to the CD-fed mice. Fig. 4i-j show exemplary normalized ratio spectra of a 'healthy' CD-fed and a 'steatosis' HFD-fed mouse. A strong peak indicative of lipid is visible at 930 nm in the 'steatosis' case, whereas no such peak is present in the 'healthy' case. Note that both spectra are characterized by higher absorption levels in the range

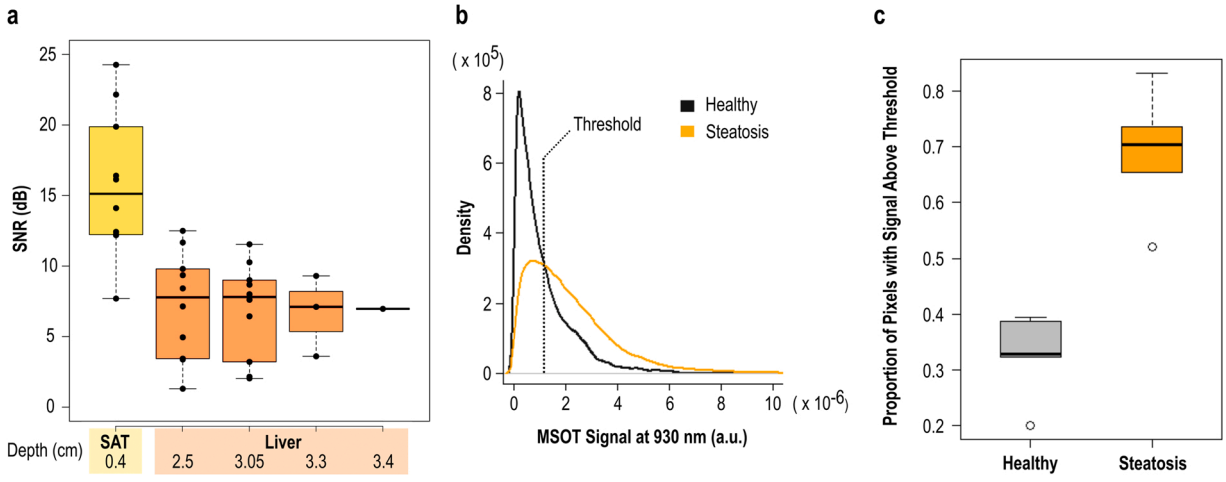

Fig. 3. Depth analysis and pixel statistics of human data. (a) SNR in dB with increasing depth in human MSOT images at 930 nm. Each box represents the SNR for the SAT or liver segments at the noted depth for all corresponding subjects. The depths (in cm) refer to the centroid of each SAT or liver segment. (b) Density curves (histogram) for the measured optoacoustic signals at 930 nm for all pixels inside the liver ROIs of all subjects. The dashed line represents the selected threshold. (c) Proportion of pixels with optoacoustic signal above the threshold for each of the two groups (healthy volunteers vs. patients with liver steatosis, p-value < 0.001).

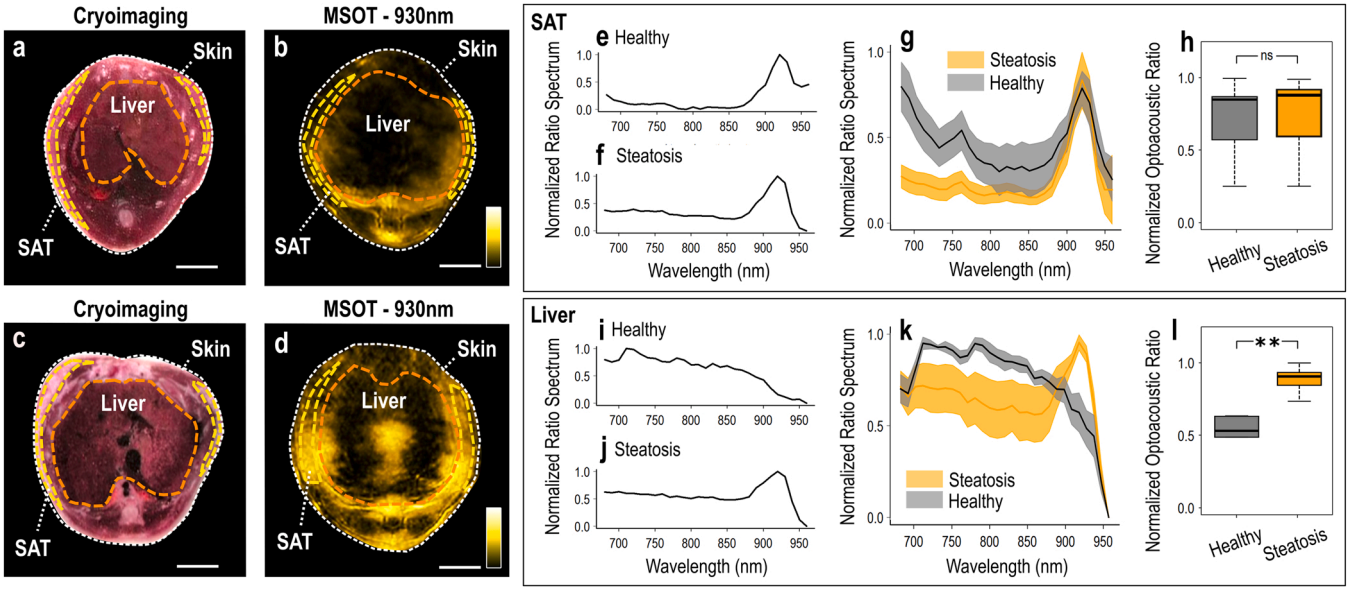

Fig. 4. Mouse MSOT imaging and data analysis. (a) Cryoimage of a CD-fed mouse. (b) MSOT image recorded at 930 nm of the same mouse. (c) Cryoimage of an HFD-mouse. (d) 930 nm-MSOT image of the same mouse as in (c). The dashed white line marks the skin surface; the dashed yellow lines delineate the subcutaneous fat (SAT) region and the dashed orange lines the liver region. (e-f) Normalized ROI/BGR ratio spectrum within the SAT region for a CD-fed (e) and an HFD-mouse (f). (g) Mean (± standard error of the mean) normalized ROI/BGR ratio spectra for the whole cohort of the CD-fed (gray) and the HFD-fed (orange) mice. (h) Normalized ROI/BGR mean pixel intensity ratio at 930 nm within the SAT region for CD-fed (gray) and HFD-fed (orange) mice. (i-j) Normalized ROI/BGR ratio spectrum within the liver region of a CD-fed (i) and an HFD-mouse (j). (k) Mean (± standard error of the mean) normalized ROI/BGR ratio spectra for the whole cohort of the CD-fed (gray) and the HFD-fed (orange) mice. (l) Normalized ROI/BGR mean pixel intensity ratio at 930 nm within the liver region of CD-fed (gray) and HFD-fed (orange) mice. ns = non statistically significant, **$p < 0.01$.

680–900 nm, compared to the spectra from the SAT regions (Fig. 4e-f), due to the much higher blood content of liver tissue compared to SAT. Fig. 4k displays the mean normalized ratio spectra for both groups of mice. Again, the peak at 930 nm is observed for the 'steatosis' group, but not for the 'healthy' control group. Fig. 4l illustrates the mean normalized ROI/BGR ratio at 930 nm for the liver region. In contrast to the SAT region, the difference between the two mouse groups in the liver region at 930 nm is statistically significant (0.886 ± 0.044 for HFD-fed mice vs. 0.484 ± 0.097 for CD-fed, p-value = 0.005, Cohen's d = 2.39).

4. Discussion

Hepatic steatosis is a significant health problem that may lead to severe liver disease and frequently coexists with other conditions, such as obesity, type 2 diabetes, and cardiovascular disorders [34]. Non-invasive imaging can provide rich information about the pathophysiology of the disease and enable early diagnosis, but available methods come with limitations (e.g., ionizing radiation, low sensitivity, bulky equipment, varying diagnostic cut-off values) that hinder their disseminated use in research and clinical settings. Here, we demonstrated that non-invasive and label-free MSOT can detect significant differences in the spectral content of the liver in patients with steatosis and the liver of healthy volunteers, which manifest as stronger absorption around 930 nm in the liver of patients with steatosis due to the accumulation of lipids. These results suggest potential clinical and research applications of MSOT for hepatic steatosis and other disorders involving lipids.

Following previous publications on imaging lipids in the bloodstream [27] or the supraclavicular region [20], our results support the capability of MSOT to detect lipids in deeper soft tissues, such as the liver, non-invasively and without the need for exogenous contrast agents. First, by conducting targeted calculations within the SAT region of mice and humans, we showcased that MSOT indeed enables the detection of lipids based purely on the recorded spectral information from the NIR, in which lipids absorb strongly at ~930 nm. The localization of the SAT region is validated via cryoimaging for the mouse data and via US for the human data. Second, we employ the same principle to detect lipids within the visualized liver region. Thus, MSOT provides not only localized tissue-specific lipid detection, but also detailed (spatial resolution of ≈ 100–300 μm) maps of lipid distributions within different tissues, organs, and anatomic compartments (e.g., SAT region and liver) in a single scan. The ability to resolve lipids in the liver and other soft tissues could be useful for detecting possible signs of distorted pathways of metabolism.

We demonstrated that the abovementioned unique capability of MSOT to detect lipids extends to depths necessary to analyse the human liver. We observed qualitative differences in the visual appearance and the spectral signatures of the livers of patients with steatosis compared to their healthy counterparts, with the steatotic livers being larger and featuring higher absorption at 930 nm (Fig. 2c-d, i-k). These observations in humans agreed well with the mouse data (Fig. 4c-d, i-k)), despite the much greater depth of the human liver. This qualitative observation of the spectra was confirmed by statistical analysis, which showed that absorption at 930 nm in the livers of both the preclinical and clinical steatosis groups was significantly higher than for the healthy groups (Figs. 4l and 2l; 0.886 ± 0.044 (diseased) vs. 0.484 ± 0.097 (healthy) with p-value = 0.005 in mice and 0.762 ± 0.146 (diseased) vs. 0.219 ± 0.081 (healthy) with p-value = 0.011 in humans). In other words, MSOT can provide both qualitative information about the consistency of liver tissue and semi-quantitative insights into its lipid-content. Thus, MSOT could be used not only for the detection of lipids, and thereby liver steatosis, but also for a rough estimation of the severity of the disease. Of course, more studies are needed in order to be able to provide an absolute quantification of lipids or other optoacoustically measured chromophores within the measured deep tissues.

Nevertheless, MSOT does not come without limitations. As discussed, MSOT reaches depths of approximately 3–4 cm, which is unattainable by other optical methods and sufficient for small animal imaging [35]. However, the achieved depth is poor compared to traditional techniques used for clinical liver imaging (e.g. US, CT, MRI) and

cannot ensure full-depth imaging of the liver, especially in obese patients. Further development of light delivery systems or light fluence correction schemes may alleviate the effects of light attenuation and increase imaging and spectral unmixing quality with increasing depths. Moreover, spectral unmixing is currently done on a per-pixel basis and the quality is highly dependent on intrinsic (e.g., breathing, arterial pulsation) or extrinsic (e.g. hand movements during scanning) motion. For these reasons, novel motion correction schemes and spectral unmixing algorithms have been developed in order to enable the precise visualizations of chromophores in deep tissues [36–38]. Finally, some steps of the MSOT data analysis process (e.g., segmentation, interpretation) might be time-consuming or labor-intensive, especially in the case of large (e.g., hundreds or thousands of images) or noisy datasets. Therefore, several automatic segmentation or image improvement techniques have been developed, even if herein, due to the small number of participants and the high data quality, we opted for a manual segmentation approach [39,40].

However, the grading of hepatic steatosis is not routine; it is mainly performed using histology, i.e., using the NAFLD Activity Score (NAS), or sometimes by means of MRI or FibroScan©. In our patient cohort, no liver biopsies were performed and, thus, no histological assessments are available. Future studies are needed in order to explore the capability of MSOT to assess hepatic steatosis at different stages, as well as investigate possible correlations of MSOT with other imaging modalities or histology.

While the current preliminary translational study is the first to successfully apply hand-held MSOT imaging for the detection of hepatic steatosis in humans, it includes only a limited number of subjects. Furthermore, even if hand-held MSOT technology reaches unprecedented depths of several centimeters compared to other light-based imaging approaches (e.g., fluorescence imaging), it cannot provide full-depth imaging of the human liver (≈ 8–10 cm), especially in obese patients. Future targeted and more extended studies will seek to i) assess the specificity, sensitivity and accuracy of MSOT technology for the assessment of hepatic steatosis, ii) investigate the possible differences among different types of fatty liver disease, and iii) further advance MSOT towards clinical translation for liver diagnostics. Our recordings were further supported by corresponding mouse data and MSOT provided the expected results in the scanned anatomic compartments, as validated by cryoimaging and medical US imaging. Thus, the proposed MSOT-based method generates new possibilities for investigating the pathophysiology of hepatic steatosis and demonstrates translational potential with possible implications for future clinical diagnostics of the disease in selected patients.

Funding

This project has received funding from the European Research Council (ERC) under the European Union's Horizon 2020 research and innovation programme under grant agreement No 694968 (PREMSOT) and was supported by the DZHK (German Centre for Cardiovascular Research; FKZ 81Z0600104), the Helmholtz Zentrum München funding program "Physician Scientists for Groundbreaking Projects" and by a Clinical Leave Stipend from the German Center of Infection Research (DZIF, grant TI07.001).

CRediT authorship contribution statement

Nikolina-Alexia Fasoula: Conceptualization, Methodology, Formal analysis, Investigation, Writing – original draft. **Angelos Karlas:** Conceptualization, Methodology, Formal analysis, Investigation, Writing – original draft, Visualization, Funding acquisition. **Olga Prokopchuk:** Methodology, Investigation, Writing – original draft, Funding acquisition. **Nikoletta Katsouli:** Methodology, Formal analysis, Visualization. **Michail Bariotakis:** Methodology, Formal analysis, Writing – original draft, Visualization. **Evangelos Liapis:** Methodology, Writing – original draft. **Anna Goetz:** Methodology. **Michael Kallmayer:** Methodology, Writing – review & editing. **Josefine Reber:** Methodology, Investigation, Writing – original draft. **Alexander Novotny:** Writing – original draft. **Helmut Friess:** Supervision. **Marc Ringelhan:** Writing – original draft. **Roland Schmid:** Supervision. **Hans-Henning Eckstein:** Supervision. **Susanna Hofmann:** Writing – review & editing, Supervision. **Vasilis Ntziachristos:** Conceptualization, Writing – review & editing, Supervision, Funding acquisition.

Declaration of Competing Interest

V.N. is a founder and equity owner of sThesis GmbH, iThera Medical GmbH, Spear UG, and i3 Inc. All other authors declare that they have no competing interests.

Data availability

Data will be made available on request.

Acknowledgments

We thank Dr. Robert Wilson, Dr. Gabriella Leung and Dr. Serene Lee for their attentive reading and improvements of the manuscript.

References

[1] Z.M. Younossi, A.B. Koenig, D. Abdelatif, Y. Fazel, L. Henry, M. Wymer, Global epidemiology of nonalcoholic fatty liver disease-meta-analytic assessment of prevalence, incidence, and outcomes, Hepatology 64 (2016) 73–84.
[2] N. Chalasani, Z. Younossi, J.E. Lavine, M. Charlton, K. Cusi, M. Rinella, S. A. Harrison, E.M. Brunt, A.J. Sanyal, The diagnosis and management of nonalcoholic fatty liver disease: practice guidance from the American Association for the Study of Liver Diseases, Hepatology 67 (2018) 328–357.
[3] N.T. Gunn, M.L. Shiffman, The use of liver biopsy in nonalcoholic fatty liver disease: when to biopsy and in whom, Clin. Liver Dis. 22 (2018) 109–119.
[4] P.O. Schulz, F.G. Ferreira, F. Nascimento Mde, A. Vieira, M.A. Ribeiro, A.I. David, L.A. Szutan, Association of nonalcoholic fatty liver disease and liver cancer, World J. Gastroenterol. 21 (2015) 913–918.
[5] J.K. Peng, N. Hepgul, I.J. Higginson, W. Gao, Symptom prevalence and quality of life of patients with end-stage liver disease: a systematic review and meta-analysis, Palliat. Med. 33 (2019) 24–36.
[6] K.-H. Chuah, W.-K. Chan, Quantification of liver fat in NAFLD: available modalities and clinical significance, Curr. Hepatol. Rep. 18 (2019) 492–502.
[7] J.K. Gaidos, B.E. Hillner, A.J. Sanyal, A decision analysis study of the value of a liver biopsy in nonalcoholic steatohepatitis, Liver Int. Off. J. Int. Assoc. Study Liver 28 (2008) 650–658.
[8] I.L. Nalbantoglu, E.M. Brunt, Role of liver biopsy in nonalcoholic fatty liver disease, World J. Gastroenterol. 20 (2014) 9026–9037.
[9] Q. Li, M. Dhyani, J.R. Grajo, C. Sirlin, A.E. Samir, Current status of imaging in nonalcoholic fatty liver disease, World J. Hepatol. 10 (2018) 530–542.
[10] A. Raizner, N. Shillingford, P.D. Mitchell, S. Harney, R. Raza, J. Serino, M. M. Jonas, C.K. Lee, Hepatic inflammation may influence liver stiffness measurements by transient elastography in children and young adults, J. Pediatr. Gastroenterol. Nutr. 64 (2017) 512–517.
[11] Y.N. Zhang, K.J. Fowler, G. Hamilton, J.Y. Cui, E.Z. Sy, M. Balanay, J.C. Hooker, N. Szeverenyi, C.B. Sirlin, Liver fat imaging-a clinical overview of ultrasound, CT, and MR imaging, 20170959-20170959, Br. J. Radiol. 91 (2018), 20170959-20170959.
[12] L.S. Szczepaniak, E.E. Babcock, F. Schick, R.L. Dobbins, A. Garg, D.K. Burns, J. D. McGarry, D.T. Stein, Measurement of intracellular triglyceride stores by H spectroscopy: validation in vivo, Am. J. Physiol. 276 (1999) E977–E989.
[13] J. Chen, J.A. Talwalkar, M. Yin, K.J. Glaser, S.O. Sanderson, R.L. Ehman, Early detection of nonalcoholic steatohepatitis in patients with nonalcoholic fatty liver disease by using MR elastography, Radiology 259 (2011) 749–756.
[14] T. Karlas, D. Petroff, M. Sasso, J.G. Fan, Y.Q. Mi, V. de Lédinghen, M. Kumar, M. Lupsor-Platon, K.H. Han, A.C. Cardoso, G. Ferraioli, W.K. Chan, V.W. Wong, R. P. Myers, K. Chayama, M. Friedrich-Rust, M. Beaugrand, F. Shen, J.B. Hiriart, S. K. Sarin, R. Badea, K.S. Jung, P. Marcellin, C. Filice, S. Mahadeva, G.L. Wong, P. Crotty, K. Masaki, J. Bojunga, P. Bedossa, V. Keim, J. Wiegand, Individual patient data meta-analysis of controlled attenuation parameter (CAP) technology for assessing steatosis, J. Hepatol. 66 (2017) 1022–1030.
[15] T.G. Cotter, M. Rinella, Nonalcoholic fatty liver disease 2020: the state of the disease, Gastroenterology 158 (2020) 1851–1864.
[16] A.M. Pirmoazen, A. Khurana, A. El Kaffas, A. Kamaya, Quantitative ultrasound approaches for diagnosis and monitoring hepatic steatosis in nonalcoholic fatty liver disease, Theranostics 10 (2020) 4277–4289.
[17] K. Pu, Y. Wang, S. Bai, H. Wei, Y. Zhou, J. Fan, L. Qiao, Diagnostic accuracy of controlled attenuation parameter (CAP) as a non-invasive test for steatosis in

suspected non-alcoholic fatty liver disease: a systematic review and meta-analysis, BMC Gastroenterol. 19 (2019) 51.
[18] F. Knieling, C. Neufert, A. Hartmann, J. Claussen, A. Urich, C. Egger, M. Vetter, S. Fischer, L. Pfeifer, A. Hagel, C. Kielisch, R.S. Gortz, D. Wildner, M. Engel, J. Rother, W. Uter, J. Siebler, R. Atreya, W. Rascher, D. Strobel, M.F. Neurath, M. J. Waldner, Multispectral optoacoustic tomography for assessment of Crohn's disease activity, N. Engl. J. Med. 376 (2017) 1292–1294.
[19] A.P. Regensburger, L.M. Fonteyne, J. Jungert, A.L. Wagner, T. Gerhalter, A. M. Nagel, R. Heiss, F. Flenkenthaler, M. Qurashi, M.F. Neurath, N. Klymiuk, E. Kemter, T. Frohlich, M. Uder, J. Woelfle, W. Rascher, R. Trollmann, E. Wolf, M. J. Waldner, F. Knieling, Detection of collagens by multispectral optoacoustic tomography as an imaging biomarker for Duchenne muscular dystrophy, Nat. Med. 25 (2019) 1905–1915.
[20] J. Reber, M. Willershäuser, A. Karlas, K. Paul-Yuan, G. Diot, D. Franz, T. Fromme, S.V. Ovsepian, N. Bézière, E. Dubikovskaya, D.C. Karampinos, C. Holzapfel, H. Hauner, M. Klingenspor, V. Ntziachristos, Non-invasive measurement of brown fat metabolism based on optoacoustic imaging of hemoglobin gradients, e684, Cell Metab. 27 (2018) 689–701. e684.
[21] Y. Li, K. Schnabl, S.M. Gabler, M. Willershauser, J. Reber, A. Karlas, S. Laurila, M. Lahesmaa, U. D. M, A. Bast-Habersbrunner, K.A. Virtanen, T. Fromme, F. Bolze, L.S. O'Farrell, J. Alsina-Fernandez, T. Coskun, V. Ntziachristos, P. Nuutila, M. Klingenspor, Secretin-activated brown fat mediates prandial thermogenesis to induce satiation, e1512, Cell 175 (2018) 1561–1574. e1512.
[22] A. Karlas, N.A. Fasoula, K. Paul-Yuan, J. Reber, M. Kallmayer, D. Bozhko, M. Seeger, H.H. Eckstein, M. Wildgruber, V. Ntziachristos, Cardiovascular optoacoustics: from mice to men - a review, Photoacoustics 14 (2019) 19–30.
[23] A. Karlas, M. Kallmayer, M. Bariotakis, N.A. Fasoula, E. Liapis, F. Hyafil, J. Pelisek, M. Wildgruber, H.H. Eckstein, V. Ntziachristos, Multispectral optoacoustic tomography of lipid and hemoglobin contrast in human carotid atherosclerosis, Photoacoustics 23 (2021), 100283.
[24] A. Karlas, M. Kallmayer, N.A. Fasoula, E. Liapis, M. Bariotakis, M. Kronke, M. Anastasopoulou, J. Reber, H.H. Eckstein, V. Ntziachristos, Multispectral optoacoustic tomography of muscle perfusion and oxygenation under arterial and venous occlusion - a human pilot study, J. Biophotonics (2020), e201960169.
[25] A. Karlas, M. Masthoff, M. Kallmayer, A. Helfen, M. Bariotakis, N.A. Fasoula, M. Schäfers, M. Seidensticker, H.-H. Eckstein, V. Ntziachristos, M. Wildgruber, Multispectral optoacoustic tomography of peripheral arterial disease based on muscle hemoglobin gradients—a pilot clinical study, Ann. Transl. Med. (2020) (Publish ahead of print).
[26] A. Karlas, M.A. Pleitez, J. Aguirre, V. Ntziachristos, Optoacoustic imaging in endocrinology and metabolism, Nat. Rev. Endocrinol. (2021).
[27] N.-A. Fasoula, A. Karlas, M. Kallmayer, A.B. Milik, J. Pelisek, H.-H. Eckstein, M. Klingenspor, V. Ntziachristos, Multicompartmental non-invasive sensing of postprandial lipemia in humans with multispectral optoacoustic tomography, Mol. Metab. (2021), 101184.
[28] A. Karlas, J. Reber, E. Liapis, K. Paul-Yuan, V. Ntziachristos, Multispectral optoacoustic tomography of brown adipose tissue, Handb. Exp. Pharmacol. 251 (2019) 325–336.
[29] S. Huang, A. Blutke, A. Feuchtinger, U. Klemm, R. Zachariah Tom, S.M. Hofmann, A.C. Stiel, V. Ntziachristos, Functional multispectral optoacoustic tomography imaging of hepatic steatosis development in mice, EMBO Mol. Med. 13 (2021), e13490.
[30] R. Hernaez, M. Lazo, S. Bonekamp, I. Kamel, F.L. Brancati, E. Guallar, J.M. Clark, Diagnostic accuracy and reliability of ultrasonography for the detection of fatty liver: a meta-analysis, Hepatology 54 (2011) 1082–1090.
[31] G. Ferraioli, L.B. Soares Monteiro, Ultrasound-based techniques for the diagnosis of liver steatosis, World J. Gastroenterol. 25 (2019) 6053–6062.
[32] T.L.I.O. America, American National Standards for the Safe Use of Lasers, ANSI Z136.1, 2000.
[33] A. Rosenthal, V. Ntziachristos, D. Razansky, Model-based optoacoustic inversion with arbitrary-shape detectors, Med Phys. 38 (2011) 4285–4295.
[34] E. Vanni, A. Marengo, L. Mezzabotta, E. Bugianesi, Systemic complications of nonalcoholic fatty liver disease: when the liver is not an innocent bystander, Semin. Liver Dis. 35 (2015) 236–249.
[35] V. Ntziachristos, Going deeper than microscopy: the optical imaging frontier in biology, Nat. Methods 7 (2010) 603–614.
[36] M. Kim, G.-S. Jeng, M. O'Donnell, I. Pelivanov, Correction of wavelength-dependent laser fluence in swept-beam spectroscopic photoacoustic imaging with a hand-held probe, Photoacoustics 19 (2020), 100192.
[37] S. Tzoumas, A. Nunes, I. Olefir, S. Stangl, P. Symvoulidis, S. Glasl, C. Bayer, G. Multhoff, V. Ntziachristos, Eigenspectra optoacoustic tomography achieves quantitative blood oxygenation imaging deep in tissues, Nat. Commun. 7 (2016) 12121.
[38] A. Ron, N. Davoudi, X.L. Deán-Ben, D. Razansky, Self-gated respiratory motion rejection for optoacoustic tomography, Appl. Sci. 9 (2019) 2737.
[39] N.K. Chlis, A. Karlas, N.A. Fasoula, M. Kallmayer, H.H. Eckstein, F.J. Theis, V. Ntziachristos, C. Marr, A sparse deep learning approach for automatic segmentation of human vasculature in multispectral optoacoustic tomography, Photoacoustics 20 (2020), 100203.
[40] I. Dimaridis, P. Sridharan, V. Ntziachristos, A. Karlas, L. Hadjileontiadis, Image quality improvement techniques and assessment adequacy in clinical optoacoustic imaging: a systematic review, Biosensors 12 (2022).

Nikolina-Alexia Fasoula studied Medicine (M.D.) at the University of Thessaly in Larisa, Greece. She holds a Master of Science in Human Genetics (M.Sc.) from the Department of Medicine, University of Thessaly in Larisa, Greece. Her Master thesis was in "Host genetics and gut microbiome interactions in metabolic diseases". She is currently doing her PhD (Dr. rer. nat.) in Experimental Medicine at the Technical University of Munich, Germany. She is a student in the interdisciplinary Clinical Bioengineering Group. Her main research interests are in the areas of cardiometabolic and optoacoustic imaging/sensing.

Angelos Karlas studied Medicine (M.D.) and Electrical and Computer Engineering (Dipl.-Ing.) at the Aristotle University of Thessaloniki, Greece. He holds a Master of Science in Medical Informatics (M.Sc.) from the same university and a Master of Research (M. Res., DIC) in Medical Robotics and Image-Guided Interventions from Imperial College London, UK. He is currently working as clinical resident at the Department for Vascular and Endovascular Surgery at the 'rechts der Isar' University Hospital in Munich, Germany. He is also the 'Tenure-Track' Group Leader of the Clinical Bioengineering Group at the Helmholtz Center Munich, Germany. He completed his PhD (Dr. rer. nat.) in Experimental Medicine at the Technical University of Munich, Germany. His main research interests are in the areas of vasometabolic and optoacoustic imaging/sensing, AI-based biomarkers and image-guided vascular interventions.

Vasilis Ntziachristos received his PhD in electrical engineering from the University of Pennsylvania, USA, followed by a postdoctoral position at the Center for Molecular Imaging Research at Harvard Medical School. Afterwards, he became an Instructor and following an Assistant Professor and Director at the Laboratory for Bio-Optics and Molecular Imaging at Harvard University and Massachusetts General Hospital, Boston, USA. Currently, he is the Director of the Institute for Biological and Medical Imaging at the Helmholtz Zentrum in Munich, Germany, as well as a Professor of Electrical Engineering, Professor of Medicine and Chair for Biological Imaging at the Technical University Munich. His work focuses on novel innovative optical and optoacoustic imaging modalities for studying biological processes and dis-eases as well as the translation of these findings into the clinic.

Appendix C

Publication: Opening a window to skin biomarkers for diabetes stage with optoacoustic mesoscopy

The version herein has been published in the journal "Light: Science and Applications" [71].

Official journal of the CIOMP 2047-7538
www.nature.com/lsa

ARTICLE Open Access

Opening a window to skin biomarkers for diabetes stage with optoacoustic mesoscopy

Hailong He[1,2], Nikolina-Alexia Fasoula[1,2], Angelos Karlas[1,2,3,4], Murad Omar[1,2], Juan Aguirre[1,2], Jessica Lutz[5,6], Michael Kallmayer[3], Martin Füchtenbusch[5,6], Hans-Henning Eckstein[3,4], Annette Ziegler[6,7] and Vasilis Ntziachristos[1,2,4]✉

Abstract

Being the largest and most accessible organ of the human body, the skin could offer a window to diabetes-related complications on the microvasculature. However, skin microvasculature is typically assessed by histological analysis, which is not suited for applications to large populations or longitudinal studies. We introduce ultra-wideband raster-scan optoacoustic mesoscopy (RSOM) for precise, non-invasive assessment of diabetes-related changes in the dermal microvasculature and skin micro-anatomy, resolved with unprecedented sensitivity and detail without the need for contrast agents. Providing unique imaging contrast, we explored a possible role for RSOM as an investigational tool in diabetes healthcare and offer the first comprehensive study investigating the relationship between different diabetes complications and microvascular features in vivo. We applied RSOM to scan the pretibial area of 95 participants with diabetes mellitus and 48 age-matched volunteers without diabetes, grouped according to disease complications, and extracted six label-free optoacoustic biomarkers of human skin, including dermal microvasculature density and epidermal parameters, based on a novel image-processing pipeline. We then correlated these biomarkers to disease severity and found statistically significant effects on microvasculature parameters as a function of diabetes complications. We discuss how label-free RSOM biomarkers can lead to a quantitative assessment of the systemic effects of diabetes and its complications, complementing the qualitative assessment allowed by current clinical metrics, possibly leading to a precise scoring system that captures the gradual evolution of the disease.

Introduction

Diabetes mellitus is a complex metabolic disease with increasing worldwide prevalence, leading to several health complications and aggravating healthcare costs[1,2]. The disease affects the macro- and the microvasculature of several organs, including the heart, brain, lower limbs, retinas, peripheral nerves, kidneys, and skin[1–4]. In the skin, diabetes-induced microvasculature alterations indicate an adverse disease prognosis, as they compromise tissue perfusion and oxygenation, as well as skin integrity, which can lead to cutaneous infections[3,5–8], neuropathy with loss of sensation, ulcerations, and other comorbidities[3,5–7]. These microvascular changes may also indicate cardiovascular complications such as coronary artery disease (CAD), carotid artery disease, and peripheral arterial disease (PAD)[9–11] and occur early in the development of diabetes[3,4,12]. Therefore, assessment of skin microvasculature could lead to a novel means of monitoring diabetes onset and the progression of associated vascular complications, allowing quantification of the true burden of the disease on the vascular system rather than disease course predictions offered by risk factors.

Currently, the characterization of diabetes stage and its complications in patients relies on the assessment of clinical symptoms and signs. In many instances, questionnaires

Correspondence: Vasilis Ntziachristos (bioimaging.translatum@tum.de)
[1]Institute of Biological and Medical Imaging, Helmholtz Zentrum München, Neuherberg, Germany
[2]Chair of Biological Imaging at the Central Institute for Translational Cancer Research (TranslaTUM), School of Medicine, Technical University of Munich, Munich, Germany
Full list of author information is available at the end of the article
These authors contributed equally: Hailong He, Nikolina-Alexia Fasoula

and scoring systems are employed to assess the presence and quality of peripheral neuropathy symptoms and signs such as neuropathic pain, decreased perception of light touches or muscle weakness, and can be combined with clinical tests assessing pathophysiological parameters[5,6]. Such assessments may offer subjective readings, are time-consuming, and generally evaluate the progression of the disease and its complications at infrequent intervals, during which diabetes has advanced significantly enough to yield large pathophysiological changes that present as clinical symptoms relating to loss of function of different organs and/or pain.

Disease manifestations in the skin microvasculature could serve as a means to observe the multi-systemic effects of diabetes and its complications in a quantitative fashion and possibly lead to finer and more detailed information in the course of the disease based on gradual changes that are not perceivable as clinical symptoms. Skin as the largest and most easily accessible organ could serve as a window for diabetes microangiopathy and staging of the disease. However, routine assessment of epidermal features and dermal microvasculature requires a method appropriate for safe, longitudinal, direct, and non-invasive measurements. Located under the highly-scattering epidermis, dermal vasculature is not generally accessible to optical microscopy methods, such as confocal or two-photon microscopy[13,14]. Other methods, such as high-frequency ultrasound[15–18], hyperspectral imaging[19,20], nailfold capillaroscopy[21,22], and optical coherence tomography (OCT)[23,24], have various advantages. However, in general, these technologies do not provide sufficient resolution, contrast, and/or penetration depth to visualize skin microvasculature and hence application has mostly been restricted to differentiating patients with diabetes from healthy subjects[23,24]. Although certain methods have demonstrated microvascular variations between individuals with and without diabetes, to the best of our knowledge, none of these methods have been utilized to classify disease progression or its complications or employed to examine the correlation between microvascular imaging biomarkers and diabetic complications. Such information is an important goal for an imaging method, as it would address a current gap in diabetes research associated with disease staging. Currently, only crude, and infrequent assessments of disease complications known to affect the quality of delivered healthcare are done[25,26], as elaborated in the discussion section of this paper.

It has been demonstrated that OCT angiography (OCTA) and ultra-wideband raster scan optoacoustic mesoscopy (UWB-RSOM) both have the potential to indirectly detect vasculature by capturing small signal variations resulting from micro-flows, thereby presenting non-invasive approaches for evaluating cutaneous changes in human skin microvasculature[23,27–33]. In this work, we have chosen to focus on UWB-RSOM due to certain key features. UWB-RSOM is a notably robust method for visualizing deep dermal microvasculature features (up to 1.5 mm deep) and this ability will enable our search to identify novel biomarkers of skin microangiopathy in diabetes. Furthermore, RSOM offers detection with an enhanced signal-to-noise ratio due to the generation of optoacoustic signals within blood vessels primarily. This phenomenon allows for optimal microvascular imaging of the skin, while retaining high contrast due to the relatively high absorption of hemoglobin at the wavelength of 532 nm[28,34–39]. Furthermore, it was important to obtain highly detailed cross-sectional images of human skin at high penetration depth because these images would offer valuable information for diagnosis, treatment monitoring, and translational research from understanding skin physiology and pathology and indeed UWB-RSOM can provide such images to a depth of ~1.5 mm.

We therefore employed UWB-RSOM to evaluate the effect of diabetes on skin, offering the first in vivo insights on the relation of dermal and epidermal features and diabetes complications. To this end, we performed measurements on 143 subjects including healthy individuals without diabetes and participants with diabetes. The diabetic group comprised of participants with previously diagnosed diabetes and no other symptoms, participants with diabetes and peripheral neuropathy and participants with diabetes and macrovascular atherosclerotic complications. We were specifically interested in exploring how diabetes progressed, as evidenced in this study by the presence of different complications, effects on different dermal and microvascular components and whether it could be correlated to any of the calculated skin features. We postulated that we could employ image analysis techniques to detect and quantify RSOM skin features associated with the stage of diabetes mellitus, and this would be an improvement to the currently done characterization based on clinical symptoms and comorbidities.

Results

RSOM imaging and biomarker computation

To enable quantitative analysis of diabetic skin microvascular features, we collected RSOM measurements from 95 participants with diabetes and 48 volunteers without diabetes and developed an imaging analysis pipeline to compute skin biomarkers (Fig. 1). RSOM illuminated the surface of the skin over the pretibial area at 532 nm and scanned with an ultrasound transducer with bandwidth from 10 MHz to 120 MHz and central frequency of 50 MHz over a $4 \times 2\ mm^2$ field of view (FOV, Fig. 1a, see RSOM imaging system in

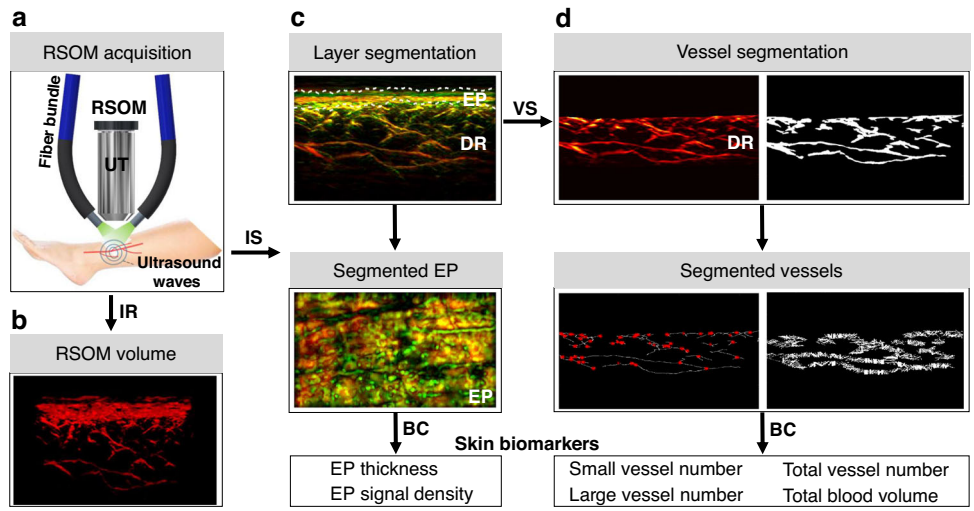

Fig. 1 Computation pipeline of skin biomarkers from RSOM images. a Schematic of the RSOM system employed for skin measurements, comprising two fiber bundles for illumination and a high frequency ultrasound transducer (UT) that was raster scanned over the skin surface. RSOM signals are recorded on the pretibial area of the lower extremities of both healthy volunteers and participants with diabetes, after which volumetric image reconstruction (IR) is performed. **b** A reconstructed RSOM volume image. The volumetric RSOM image is segmented (IS) to identify the epidermis layer and dermal vasculature, which are used to subsequently compute biomarkers. **c** Segmentation of the cross-sectional RSOM image into the epidermis (EP) and dermis (DR) layers of the skin (white dashed lines). The EP thickness and EP signal density biomarkers were computed from the segmented EP layers in the RSOM images. **d** Vessel segmentation of the segmented DR layer of the skin. The numbers of vessel branches and vessel diameters were automatically calculated; the red dots indicate positions of vessel branches. The segmented vessels in the DR were used to calculate the vessel numbers and total blood volume biomarkers. IR image reconstruction, IS image segmentation, VS vessel segmentation, BC biomarker computation, scale bar = 500 µm

"Methods" section). Three-dimensional RSOM images (Fig. 1b, see image reconstruction in "Methods" section) were reconstructed over two frequency bands within the 120 MHz bandwidth employed. Band-selected reconstructions implicitly segmented vessels of different sizes; larger vessels (40–150 µm) are seen in the 10–40 MHz band, whereby smaller vessels (<10–40 µm) are seen in the 40–120 MHz band. Vessels seen in the two different bands are color-coded in the rendered images (red: larger vessels; green: smaller vessels) so that finer vasculature is highlighted in the presence of larger vessels (Fig. 1c). To quantify the differences observed by visual inspection of the RSOM images, as well as to extract relevant label-free RSOM biomarkers, we developed and validated a RSOM image analysis pipeline including two segmentation methods (see layer and vasculature segmentation section in "Methods" section). Briefly, a layer segmentation algorithm based on graph theory and dynamic programming[40] identified and separated the epidermis and dermis, as visually marked on the images (Fig. 1c, white dashed lines; see layer segmentation section in "Methods" section and Fig. S2). The second method employed a vessel segmentation algorithm[41] to identify and quantify vascular structures in the dermis layer (Fig. 1d; see vessel segmentation section in "Methods" section and Fig. S3). Quantification included the computation of the vessel number and the diameter of the different vessels identified. Validation of the segmentation approach was performed by comparing the RSOM computed biomarkers of mice skin with histological analysis (see validation section in "Methods" section and Figs. S2 and S4).

Based on this RSOM image analysis pipeline, we computed and differentially analyzed six RSOM image features (see biomarker computation section in "Methods" section): (1) the total number of small vessels (with diameters <40 µm; 40–120 MHz band) in the dermal layer; (2) the total number of large vessels (with diameters >40 µm; 10–40 MHz band) in the dermal layer; (3) the total vessel number in the dermal layer; (4) the total blood volume in the dermal layer, computed as ratio of the total number of volume elements (voxels) occupied by the segmented vessels over the total number of voxels in the image; (5) the epidermal thickness, and (6) the epidermal signal density. The selection of small vs. large vessels based on the 40 µm cut-off value was explained (see "Methods" section) and a more detailed analysis based on a finer vessel classification is shown in Fig. S5.

Skin microvasculature differences between healthy volunteers and participants with diabetes

We first analyzed RSOM skin images of the lower extremities (distal pretibial area) of 95 participants with

Table 1 Characteristics of study participants

	Participants with diabetes mellitus (DM) (95)	Participants with DM and no complications (45)	Participants with DM, neuropathy and no ASCVD (25)	Participants with DM, neuropathy and ASCVD (25)	Healthy volunteers (48)	*P*-value
Age (years)	68 ± 12	63 ± 19	70 ± 10	76 ± 7	64 ± 13	ns
Disease duration (years)	20 ± 16	12 ± 11	27 ± 17	23 ± 16	0	ns
Sex (male/female)	42/56	24/19	9/18	6/19	27/21	n/a
BMI (kg/m^2)	27 ± 8	27 ± 6	30 ± 8	28 ± 4	26 ± 7	ns
Diabetes type (1/2)	21/74	7/36	11/14	3/22	n/a	n/a
NSS	4 ± 4	0	4 ± 4	7 ± 2	n/a	n/a
NDS	4 ± 4	0	4 ± 4	6 ± 3	n/a	n/a
HbA1c[a] (%)	7.1 ± 1.1	7.1 ± 1.6	7.2 ± 0.7	6.9 ± 0.9	n/a	n/a

Data is presented as the mean ± SD unless stated otherwise. Participants with diabetes ($n = 95$) were further divided into three subgroups: Participants with DM and no complications [$n = 45$, participants with diabetes, but without neuropathy and without atherosclerotic cardiovascular disease (ASCVD)]; Participants with DM, neuropathy, and no ASCVD ($n = 25$, participants with diabetic neuropathy and without ASCVD); Participants with DM, neuropathy and ASCVD [$n = 25$, participants with diabetic neuropathy and ASCVD/PAD]

DM diabetes mellitus, *ASCVD* atherosclerotic cardiovascular disease, *PAD* peripheral arterial disease, *BMI* Body Mass Index, *NSS* Neuropathy Symptom Score, *NDS* Neuropathy Disability Score, *HbA1c* glycated hemoglobin, *ns* not statistically significant, *n/a* not applicable

[a]HbA1c values were not recorded for the 27 participants with diabetes and without complications

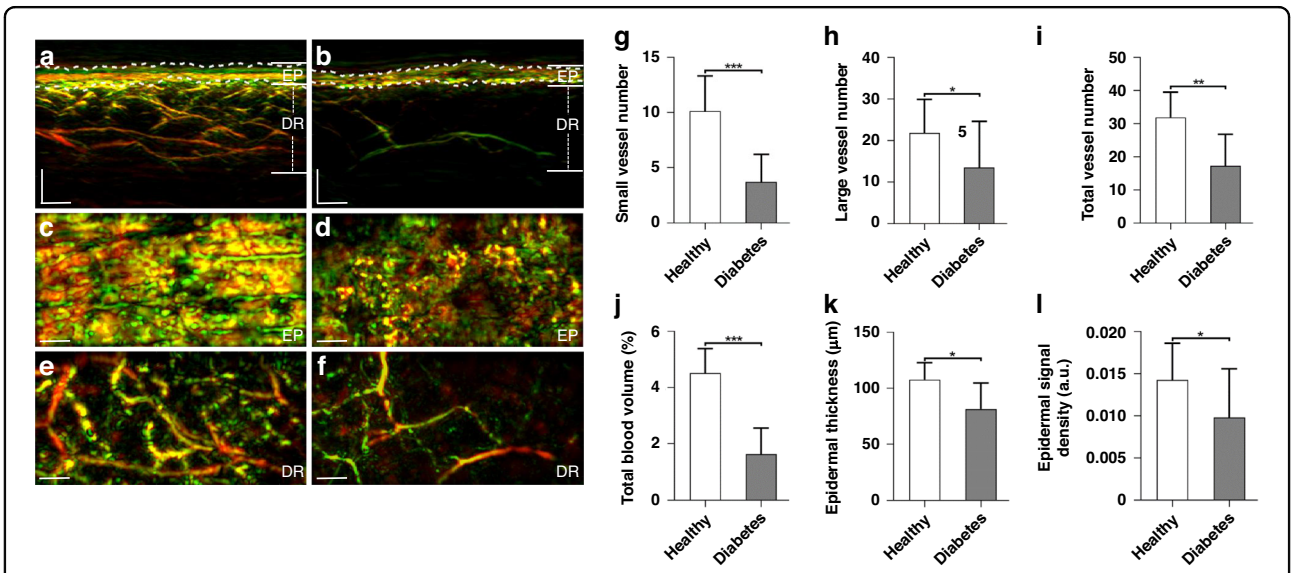

Fig. 2 Skin imaging of the lower extremities (distal pretibial region) of healthy volunteers and participants with diabetes using clinical RSOM. a Sectional RSOM image of healthy skin. **b** Sectional RSOM image of skin from a participant with diabetes but without neuropathy. MIP images of the EP and DR layers in the coronal views corresponding to (**a**, **b**) are displayed in (**c**, **d**) and (**e**, **f**), respectively. **g**–**l** Comparisons of computed biomarkers between healthy volunteers and participants with diabetes. **g** Total number of small vessels (with diameter ≤40 μm) in DR layer. **h** Total number of large vessels (with diameter >40 μm) in DR layer. **i** Total numbers of vessels in DR layer. **j** Total blood volume of the DR vasculature. **k** Average thicknesses of the EP layers. **l** Signal densities of the EP layers. The healthy volunteer (control) group had a population of 48, while the group of participants with diabetes had a population of 95. *$P < 0.05$, **$P < 0.01$, and ***$P < 0.001$, respectively. Scale bar = 500 μm. EP epidermis, DR dermis

diabetes and 48 volunteers without diabetes, where the characteristics of study participants are listed in Table 1 (see data grouping section in "Methods" section). Inspection of 2-band RSOM images of the skin (Fig. 2) visually exemplifies differences between a healthy volunteer and a participant with diabetes mellitus. Figure 2a depicts an image from a 36-year-old female volunteer without diabetes, while Fig. 2b shows the corresponding

image from a 42-year-old male participant with diabetes. The images are rendered as maximum intensity projections (MIP) of the entire volume scanned and depict the epidermal (EP) and dermal (DR) layers, reaching a depth of ~1.5 mm. The typical RSOM appearance of healthy skin shows a dense signal from the epidermis layer (coronal view, Fig. 2c, d) and a vascular network in the dermal layer (coronal view, Fig. 2e) that comprises several blood vessels of various diameters. Conversely, the dermal vessel density (coronal view, Fig. 2f) is far lower in the participant with diabetes mellitus compared to the healthy volunteer, a finding that is confirmed by three-dimensional skin visualizations (see Suppl. Movie. 1 and 2). Due to the loss of fine dermal vasculature, the diabetic skin exhibits a characteristic high-contrast boundary between the epidermal and dermal layers that is not present in the healthy skin.

A next step was to examine the correlation of the six computed biomarkers (see Fig. 1c, d) to diabetes status (Fig. 2g–l). We found that the mean number of small vessels (Fig. 2g) was ~2.8 times less in participants with diabetes than in the volunteers without diabetes (3.45 ± 2.62 vessels versus 9.78 ± 3.41 vessels). A Mann–Whitney *U*-test showed statistically significant differences between the mean number of small vessels in healthy vs. diabetic subjects ($P < 0.001$). The mean number of large vessels (Fig. 2h) was about 1.5 times less in the diabetic compared to the healthy group (13.39 ± 11.30 vessels versus 20.34 ± 8.32 vessels, $P < 0.05$). This suggests that the systemic impacts of diabetes on vasculature are more prominent in small vessels than in larger vessels. These results were corroborated by analyzing the full band RSOM image (Fig. 2i), revealing the total vessel number in the volume examined. The total number of vessels was found to be 16.87 ± 9.30 for diabetic participants vs. 30.12 ± 9.87 for healthy volunteers ($P < 0.01$).

The total blood volume in the DR layer was also markedly different between the diabetic and healthy groups (Fig. 2j), with values of 1.58 ± 0.90% and 4.21 ± 1.10%, respectively. The Mann–Whitney *U*-test here also showed significant differences between the healthy and diabetic subjects ($P < 0.001$). Analysis of the EP layer also demonstrated statistically significant changes between the two groups. The mean values of epidermal thickness were 105.27 ± 17.04 µm for healthy volunteers and 81.03 ± 23.06 µm for participants with diabetes (Fig. 2k) with $P < 0.05$. Likewise, the signal density of the EP layer (Fig. 2l) in the reconstructed segmented volume, which contains contributions from melanin and capillaries, was markedly lower in the participants with diabetes than in the healthy volunteers ($P < 0.05$).

The relation between RSOM features and age (see Fig. S6), disease duration (see Fig. S7), body mass index (see Fig. S8) and HbA1c values (see Fig. S9) were investigated and shown in the supplementary results. We found that these parameters did not show obvious correlation with the RSOM biomarkers and did not significantly influence the outcome of our study. We have computed the Spearman correlation value between age/disease duration /HbA1c /BMI with the vascular biomarkers TBV (Total blood volume) and SVN (Small vessel number), which showed no significant correlation as presented in supplementary Table I. In addition, we also applied multivariate logistic regression analysis to compute the statistics of the two biomarkers TBV and SVN with adjustment of age/disease duration /Hb1Ac /BMI, which also revealed no significant association between these vascular biomarkers and characteristics of the participants (supplementary Table I). There were no significant differences in age, Hb1Ac and BMI values between the participant groups with type 1 or type 2 diabetes (supplementary Table V).

Quantification of RSOM biomarkers in diabetic neuropathy

We next investigated the relationship between peripheral diabetic neuropathy and microvasculature via the extracted RSOM label-free biomarkers. Diabetes is a chronic disease with systemic complications that generally evolve with time and affect several systems (e.g., cardiovascular, nervous etc.). For the cardiovascular system in particular, diabetes affects all of parts of the cardiovascular system resulting in cardiovascular disease being the leading cause of death among participants with diabetes. Therefore, the question of understanding severity is perhaps more critical than the separation of diabetic from healthy groups. Indeed, while diabetes encompasses a continuum of stages, a diagnostic test simply separates healthy individuals from participants with diabetes based on a threshold value. Consequently, we foresee RSOM playing an important role in quantifying benchmarks or features associated with these different stages of diabetes. To address this question, we first examined RSOM features obtained from measurements of participants with diabetes without complications and measurements from participants with diabetes and different severities of neuropathy. The severity of diabetic neuropathy was clinically evaluated using the Neuropathy Disability Score (NDS) and the Neuropathy Symptom Score (NSS)[42,43]. We divided the diabetic group into three categories: those with no complications (NC, $n = 45$), those with low score neuropathy (LN, $n = 13$; $1 \le \text{NDS} \le 5$ or $1 \le \text{NSS} \le 5$) and those with high score neuropathy (HN, $n = 12$; $\text{NDS} > 5$ or $\text{NSS} > 5$). Representative RSOM images from the healthy group and the three diabetic groups are depicted in cross-sectional (sagittal) views (Fig. 3a–d) and coronal views (images parallel to the RSOM scan plane) from the EP (Fig. 3e–h) and DR (Fig. 3i–l) layers. The images

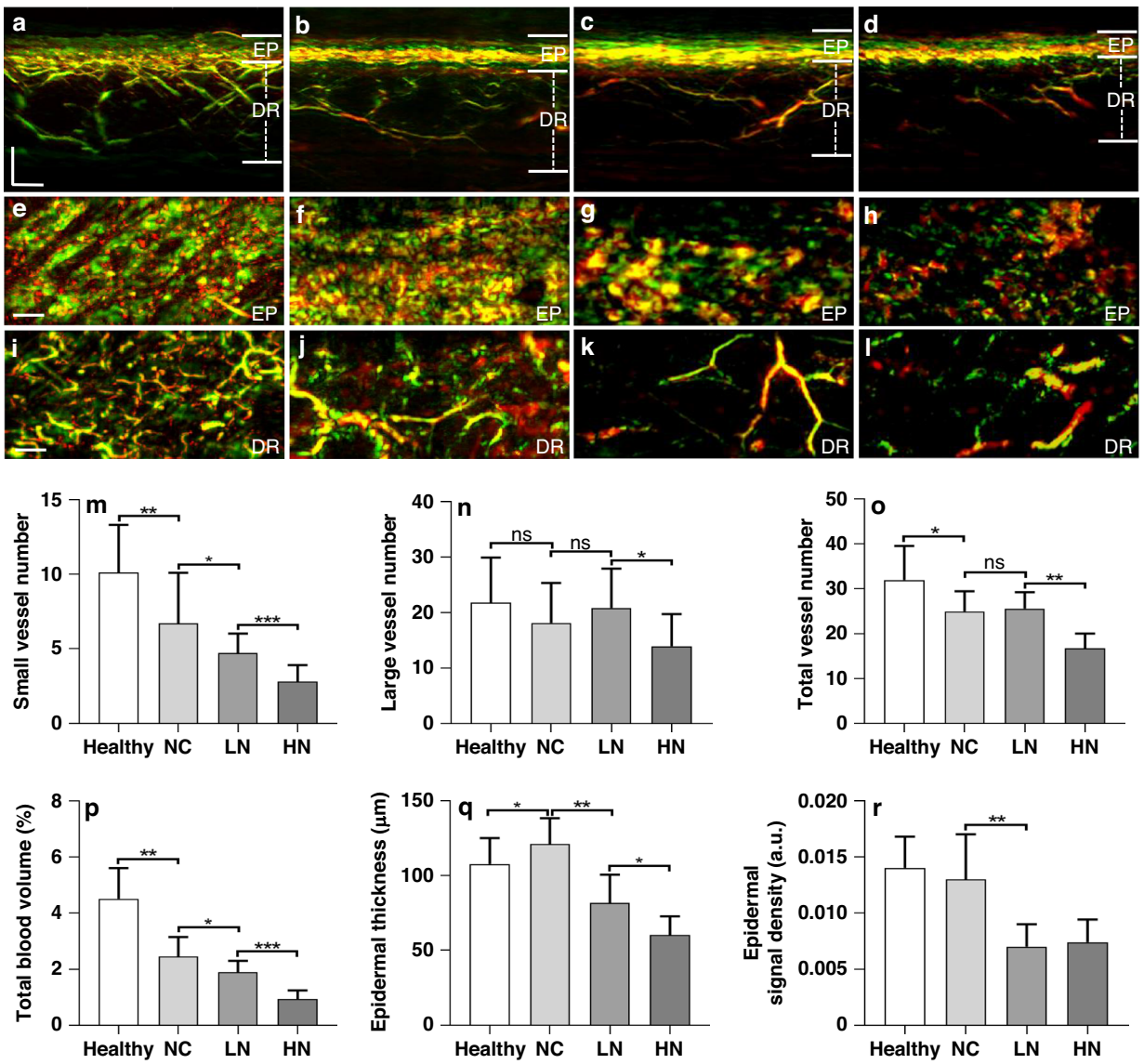

Fig. 3 Quantification of RSOM features in participants with diabetic neuropathy. The diabetic participants were grouped as follows: NC ($n = 45$), participants and no complications; LN ($n = 13$), participants with diabetes and low score neuropathy ($1 \le NDS \le 5$ or $1 \le NSS \le 5$); HN ($n = 12$), participants with diabetes and high score neuropathy (NDS > 5 or NSS > 5). **a** Sectional RSOM image of healthy skin. **b** Sectional RSOM image of skin from a participant with diabetes but without neuropathy. **c** Sectional RSOM image of skin from a participant with diabetes and low score neuropathy (NDS: 3, NSS: 3). **d** Sectional RSOM image of skin from a participant with diabetes and high score neuropathy (NDS: 9, NSS: 9). MIP images of the EP and DR layers in the coronal views corresponding to (**a**–**d**) are displayed in (**e**–**h**) and (**i**–**l**) respectively. **m**–**r** Comparisons amongst the four groups of participants with diabetes and healthy volunteers for each of the six computed biomarkers. **m** Total number of small vessels (with diameter ≤40 μm) in DR layer. **n** Total number of large vessels (diameter >40 μm) in DR layer. **o** Total vessel numbers in DR layer. **p** Total blood volume in DR layer. **q** Thickness of EP layer. **r** Signal density of EP layer as a function of group studied. $^{*}P < 0.05$, $^{**}P < 0.01$, and $^{***}P < 0.001$, respectively. Scale bar = 500 μm. ns not statistically significant, NDS Neuropathy Disability Score, NSS Neuropathy Symptom Score, EP epidermis, DR dermis

confirm a reduced vascular density in the DR with progression of the disease and its complications. Moreover, observation of the coronal views of the EP layer depicts clearly resolved superficial skin ridges in the healthy skin, which change into an amorphous pattern without ridge definition depending on disease status, especially for the groups with diabetic neuropathy.

Quantitative comparisons of the performance of different RSOM features are presented in (Fig. 3f–i). Overall, the count of small vessels (Fig. 3m) demonstrated statistically

significant differences between the three diabetic groups, i.e., healthy versus NC ($P < 0.01$), NC versus LN ($P < 0.05$), and LN versus HN ($P < 0.001$). As shown in (Fig. 3m), the neuropathy grade is visible in the count of small vessels (<40 μm diameter). However, the presence of neuropathy had no significant effects on the number of large vessels (Fig. 3n). This finding is also reflected in the total vessel number between the healthy and the NC ($P < 0.05$), as well as between the LN and HN groups ($P < 0.01$). No marked changes were observed between the NC and LN groups. The computation of blood volume (Fig. 3p) demonstrated a similar performance to the small vessel count, with the NC group exhibiting significantly lower blood volume compared to healthy group ($P < 0.01$). The total blood volume was further reduced in the LN compared to NC group ($P < 0.05$). A significant difference in total blood volume was observed between the LN and HN groups ($P < 0.001$).

The EP layers of the NC group were markedly thicker when compared to the healthy volunteers, while neuropathy decreased the epidermal thickness significantly (Fig. 3q). An unpaired *t*-test supported significant differences between the healthy versus NC ($P < 0.05$), as well as the LN versus HN ($P < 0.05$). The differences between the NC versus LN groups were even more significant ($P < 0.01$). The overall optoacoustic signal density of the EP layer (Fig. 3r) decreased in NC groups, compared to the healthy and NC groups ($P < 0.01$).

In addition, we have computed the Spearman correlation values between age/disease duration /HbA1c/BMI with the vascular biomarkers TBV and SVN in the NC, LN, and HN groups, and found no significant correlations as presented in supplementary Tables II and III. We applied multivariate logistic regression analysis to compute the statistics of the two biomarkers TBV and SVN with adjustment of age/disease duration /Hb1Ac /BMI, which showed no significant association between the vascular biomarker and participant parameters (supplementary Table IV).

Quantification of RSOM biomarkers in diabetic neuropathy and atherosclerosis

We were also interested in exploring the association between RSOM features and macrovascular atherosclerosis. Most of the diabetic subjects with atherosclerosis enrolled in this study had also been diagnosed with neuropathy. Therefore, participants with diabetes were divided into two groups: diabetic subjects with neuropathy and no atherosclerosis (NnA, $n = 25$), and diabetic subjects with neuropathy and atherosclerosis (NA, $n = 24$). Representative cross-sectional (sagittal) views and coronal views of the DR layer from the two groups (Fig. 4a–d) showed marked differences. There were significant differences in the numbers of small, large, and the total number of vessels between the group with and the group without atherosclerosis (Fig. 4e–g). The small vessel counts again exhibited the most statistically significant difference ($P < 0.001$) between the two groups, compared with the total vessel count ($P < 0.01$) and large vessel count ($P < 0.05$). In addition, the total blood volume (Fig. 4h) was significantly reduced in diabetic participants with atherosclerosis ($P < 0.001$). Conversely, atherosclerosis had no apparent effect on the epidermal thickness (Fig. 4i) or the optoacoustic signal density of the EP layer (Fig. 4j).

While no other imaging method has previously studied imaging biomarkers in relation to severity of diabetes microangiopathy, the pilot RSOM data collected herein has been shown to be able to classify participants with diabetes based on skin microvascular changes. Typically, previous imaging studies could only detect changes by comparing monitored parameters of healthy and diabetic populations, demonstrating a function that can be also achieved in a straightforward way using a blood test. In comparison, the RSOM features can be used to separate participants with diabetes from healthy individuals with high accuracy. For example, using the small vessel number (SVN) as the differentiating biomarker, a simple classification model demonstrated a 90.2% accuracy with a 93.1% sensitivity, an 80.0% specificity and an area under the Receiver Operator Characteristic (ROC) curve of 0.93 (see Fig. S11). However, we do not envision RSOM for simple diagnostic tests as above, but rather in its possible role to study the state of the vascular system on a personalized basis and, in the future, contribute to assigning a more informative "health score" as elaborated in the discussion.

Discussion

The skin has been heralded as a window to assessing systemic health conditions. This premise has so far held true for identifying several conditions, for example, manifestations of systemic sclerosis, lupus erythematosus, sarcoidosis, or several types of infections based on superficial features appearing on the upper layers of the epidermis[44]. In this work, we employ RSOM as a novel technique that can provide high-resolution imaging under the skin surface and a detailed assessment of dermal microvasculature and other skin features. RSOM is the only technique available that can non-invasively provide highly detailed three-dimensional images with virtually isotropic resolution and precise cross-sectional images of optical contrast through the deep skin dermis layer. Therefore, it enables new opportunities for three-dimensional investigation of sub-surface skin features and new ways to use the skin in identifying disease than it is possible with the traditional superficial inspection. We note that previous studies based on OCTA have offered in vivo insights into the diabetic skin microvasculature but

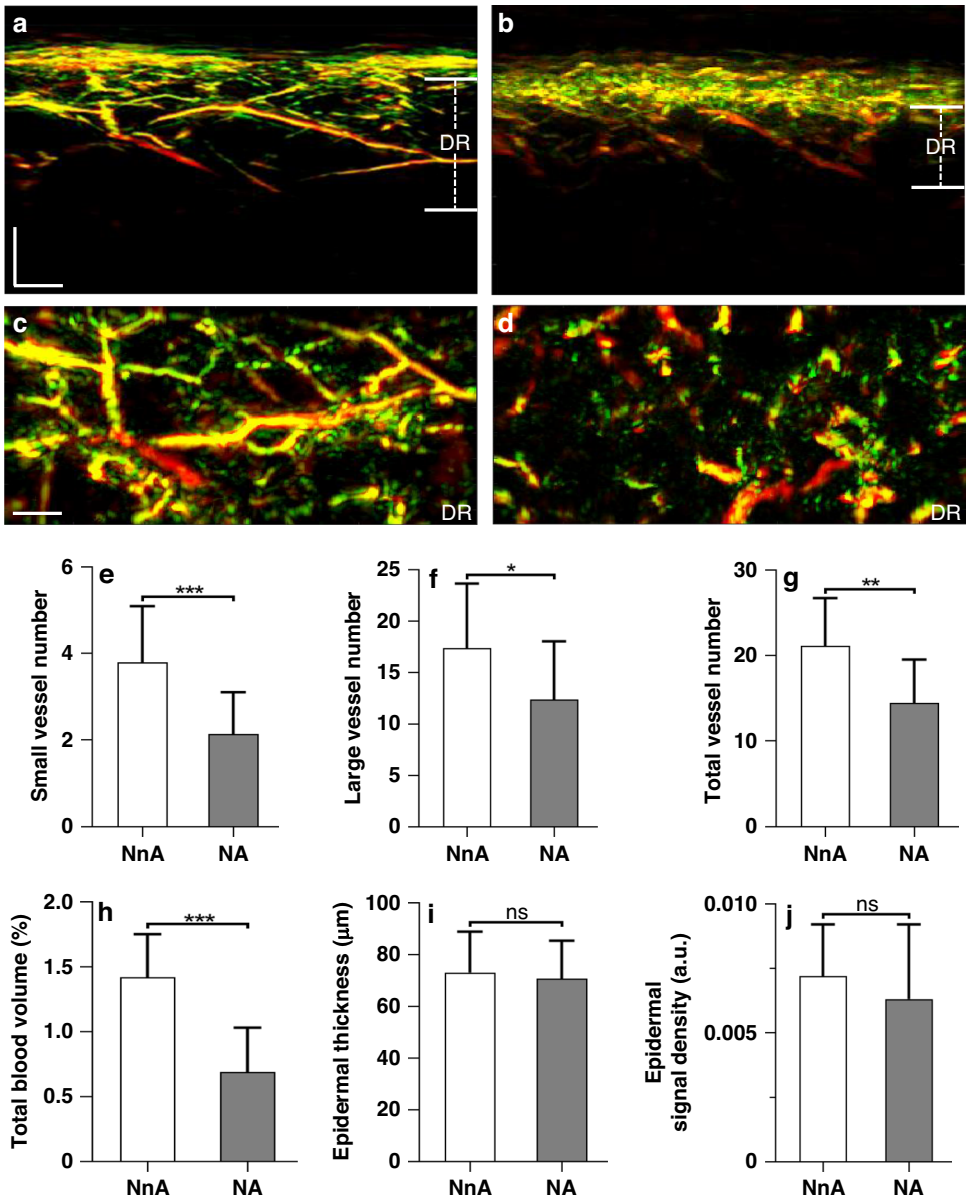

Fig. 4 Quantification of RSOM features in participants with diabetic neuropathy and atherosclerosis. Participants with diabetes were grouped as follows: diabetic subjects with neuropathy and no atherosclerosis (NnA, $n = 25$); diabetic subjects with neuropathy and atherosclerosis (NA, $n = 24$). **a** Sectional RSOM image from NnA participant. **b** Sectional RSOM image from NA participant. **c**, **d** MIP images of vascular maps in the coronal views of DR layers corresponding to (**a**, **b**). **e**–**j** Comparisons between the two groups for the following features: **e** total number of small vessels (with diameter ≤40 μm) in DR layer; **f** total number of large vessels (with diameter >40 μm) in DR layer; **g** total number of vessels in DR layer; **h** total blood volume in DR layer; **i** thickness of EP layer; **j** signal density of EP layer. *$P < 0.05$, **$P < 0.01$, and ***$P < 0.001$, respectively. Scale bar = 500 μm. ns not statistically significant. EP epidermis, DR dermis

did not reach the deep skin dermis layer compared to RSOM. Furthermore, in our study, RSOM skin features are associated with the stage of diabetes mellitus, as reflected by the presence of different diabetes-related complications. Successfully accomplishing these goals would introduce a new label-free and portable technology for quantifying diabetes complications, possibly serving in the future as a portable tool for studying and monitoring disease progression with fine precision, complementing symptom-based assessments.

The relationship between skin microvasculature and diabetes stage has not been previously investigated in a non-invasive manner, due to the lack of tools that are capable of detailed assessments of fine vasculature. Likewise, no

technologies used in other imaging studies to date have examined the relationship between biomarkers detected in vivo and disease states. High-frequency ultrasound has been applied to assess skin morphology in participants with diabetes mellitus[15–18]. However, speckle effects prevent ultrasound from visualizing microvasculature, i.e., vessels of <100 μm in diameter[45], without applying contrast agents (microbubbles), which limits routine application in humans. Hyperspectral imaging (HSI) assesses oxy- and deoxy-hemoglobin concentrations in the skin[19,20], but this method cannot visualize skin microvasculature, as it suffers from low resolution and quantification accuracy caused by variations in skin absorption and scattering properties. Nailfold capillaroscopy circumvents the scattering problem, due to the relative transparency of the nail bed, and has been employed to observe capillary abnormalities of diabetic participants[21,22]. However, thicker, opaque, or pigmented nail folds challenge the accuracy of the measurements[46,47]. OCT has been employed to assess retinal vasculature in relation to diabetic retinopathy[48–51] or measure the epidermal thickness in participants with type I diabetes mellitus[52]. Similarly, OCT angiography (OCTA) can quantify impairments of the retinal vasculature in participants with diabetic retinopathy compared to the control group[53,54]. In addition, a few studies have applied OCTA to quantify skin microvasculature structure and function, showing the possibility to distinguish between healthy individuals and participants with diabetes[23,24].

In general, several studies have explored the opportunity to differentiate between healthy volunteers and participants with diabetes based on imaging of the skin[23,24]. Nevertheless, none of these studies thoroughly examined these changes at different stages of the disease, as reported by the presence and severity of relevant complications. Herein, ultra-wideband RSOM resolves skin vessels with diameters ranging from 10 μm to about 150 μm, allowing a detailed understanding of the relationship between disease severity and vessel size, which was not previously possible. The implications of this ability of RSOM are multi-faceted, since successful application of the technology could improve the longitudinal study of diabetes and enable a method to monitor lifestyle or other interventions in a detailed, quantitative way that is not available today. RSOM can play a very different role in comparison to blood glucose measurements. While the latter determines the day-to-day glucose status and is necessary for reducing hypoglycemic incidents, RSOM could monitor an actual state of diabetes using a measure of systemic damage. Importantly, cutaneous microvasculature changes could be non-invasively monitored by means of RSOM frequently, at intervals close together enough that monitoring allows for interventions before the appearance of new clinical symptoms. Regular monitoring would also provide a more precise measure of diabetes progression.

We have previously demonstrated that RSOM can provide detailed images of skin vasculature, and that quantitative information pertaining to dermatological conditions can be extracted from these images[27,32,55,56]. However, it was unclear previously if RSOM would have the sensitivity to capture diabetes-related changes within skin microarchitecture. The ability to capture microvascular changes with RSOM would allow correlations to be drawn with diabetes severity, which had not been examined before. The study herein provided RSOM images of the skin of participants with different diabetic conditions (diabetes severity). Six RSOM label-free biomarkers were extracted from these images: three associated with dermal micro-vasculature (total vessel count, vessel count for vessels <40 μm in diameter, and vessel count for vessels >40 μm in diameter), and three associated with bulk measurements, such as the total blood volume and the thickness and signal density of the epidermis. The precision/accuracy of our segmentation methods was further validated by means of relevant animal studies. More specifically RSOM was also used to image the skin microvasculature in mice. These measurements were finally validated via histological analysis of the same skin region excised after the RSOM measurement. Visual inspection of RSOM images revealed changes in the patterns observed in the different pathologies. Qualitatively, it was generally visible that as diabetes progresses, the vascular density in the dermal layer decreases and the epidermis becomes thinner and less light absorbing. Statistical significance tests performed on features quantitatively extracted from the RSOM images confirmed that all these biomarkers are associated with aspects of diabetes progression and its complications. Moreover, these analyses identified density of vessels <40 μm in diameter to be the most indicative marker of diabetes severity, providing the starkest contrast between the different groups of participants. The identification of small vasculature as the component of the skin that is most affected by diabetes progression highlights the vulnerability of small vessels to systemic effects caused by diabetes and suggests that this marker could possibly be used as a label-free biomarker that indicates diabetes severity.

The results obtained are consistent with findings based on histology studies. Diabetes is known to alter human skin microvasculature, reflecting a systemic effect of the disease. Participants with diabetic neuropathy demonstrate pathological alterations of the microvessels[57], as also observed by RSOM. Likewise, histological analysis of the skin revealed a 7.2% increase in epidermal thickness in participants with diabetes and without neuropathy and a 16.5% decrease in participants with diabetic neuropathy compared to healthy controls (all $P < 0.05$)[58], a finding also confirmed in the current study using RSOM (Fig. 3). However, while RSOM offers a comprehensive view of the human skin, histology studies afford only partial observations. For example,

previous analyses of thick samples using confocal microscopy[59] confirmed the presence of decreased vascular densities within the sub-epidermal layers of participants with diabetes compared to healthy individuals. These findings were also consistent with our RSOM readouts (Fig. 3). In contrast, histological analysis of thin samples from superficial skin layers using conventional microscopy[60] showed that the dermal vascular density was: (i) significantly lower in participants with no or mild neuropathy but (ii) higher in participants with moderate to severe neuropathy, always compared to healthy individuals. RSOM's ability to capture three-dimensional images of the entire skin in vivo not only enables longitudinal studies on the same individual, but also more complete analyses of the effects of diabetes on the skin.

RSOM represents a potential paradigm shift in the non-invasive evaluation of skin vasculature, well beyond the current state-of-the-art. Depending on the wavelength employed, the method can penetrate several millimeters under the skin surface. Using laser with a wavelength of 532 nm in this study, we focused on visualizing the first millimeter of the skin while retaining high contrast due to the relatively high absorption of hemoglobin in the green region. Highly detailed RSOM images were showcased herein both as cross-sectional images and as coronal images from different layers. No other method today can achieve this imaging detail and depth, using label-free operation. Moreover, an RSOM system is cost-efficient and can be made highly portable to allow disseminated use. Therefore, the results point to the use of RSOM as a highly potent strategy for offering a quantitative assessment of the effects of diabetes on skin and possibly in diabetes staging. Other tests that can measure skin changes include simple visual assessment of the skin surface or Doppler imaging[61] to assess changes in blood flow in the skin due to stimuli, such as the post-occlusive increase of shear stress, hyperthermia, or drug applications[62,63]. Optical coherence tomography also offers partial views of skin microvasculature[33,64]. However, none of these methods offers the quality and detail of RSOM, and consequently, none of these methods have been considered for assessing skin microvasculature and diabetes-related alterations.

There are several reports that microvascular changes occur early in the course of diabetes[3,5,7,8,59,60]. This observation points to a prospective study in high-risk populations to examine RSOM biomarkers at different stages of disease development, from pre-diabetes to diabetes. Such a study could further expand the possible applications of RSOM, not only as a tool to stage and monitor the progression of diabetes, but also as a means for early detection. For example, with RSOM being safe, portable, and non-invasive, such measurements could be readily extended to larger-scale and multi-center studies, in particular as it concerns collection of data for identifying the early detection power of the RSOM biomarkers. Likewise, optimization studies could be performed to identify potential differences in different skin loci of RSOM acquisition and select locations that further improve performance. Our current RSOM system is equipped with a monochromatic laser and provides access to total hemoglobin measurements but does not differentiate further between oxygenated and deoxygenated hemoglobin. In the future, we aim to employ multispectral RSOM imaging (see Fig. S12) to quantify changes in both oxygenated and deoxygenated hemoglobin and extract information on skin metabolism and oxygenation. These measurements can be used to explain the pathophysiology of chronic wounds and prognose disrupted wound healing processes in participants with diabetes mellitus that result in an enormous cost burden and decreased of quality of life. Another potential use of RSOM could be in improving classification of participants with diabetes by assigning a quantitative "health score" based on the status of skin features. The current practice of separating diabetic and healthy populations based on a simple threshold is a sub-optimal strategy for prevention and diabetes healthcare[25,26] that converts a gradual progression to a binary distribution. It has been noted[25,26] that it is possible to administer better healthcare when the population is not separated by a threshold but rather assigned a score so that individuals are better alerted to their condition, monitored closely and be considered for a prevention program. A non-invasive portable and label-free technology such as RSOM could play a vital role in offering quantitative metrics in high-risk populations and evaluating possible interventions. Although such strategies apply primarily to participants with type 2 diabetes, the overall need to improve diabetes staging has been outlined for both types of diabetes 1 and 2[25,26].

In summary, we presented the first imaging study correlating in vivo biomarkers to diabetes severity. The data also represents the first optoacoustic mesoscopy images of the skin of participants with diabetes, as well as the first non-invasive in vivo study of the effects of diabetes and its complications on skin microvasculature and skin microanatomy in participants with diabetes mellitus. RSOM extracted six label-free biomarkers associated with skin morphology and microvasculature and identified fine vasculature as the feature most sensitive to progress of complications of diabetes. This finding further shows the promise of RSOM as a potential point-of-care device for quantifying systemic complications of diabetes and providing a quantitative score indicative of disease stage. Due to its safety, portability, low cost, high image quality, and ability to quantify label-free biomarkers, RSOM may offer a paradigm shift in the clinical characterization of diabetes, assessment of interventions and in prevention programs.

Materials and methods

RSOM imaging system

We employed an in-house portable RSOM imaging system featuring a transducer with a 10–120 MHz bandwidth and central frequency of ~50 MHz (Fig. 1a), which has been described in detail elsewhere[27,65]. Illumination was provided by a pulsed laser at a wavelength of 532 nm. The repetition rate of the laser was 1 kHz, yielding an optical fluence of 3.75 μJ/mm^2, which is far below the safety limit according to the American National Standards for Safe Use of Lasers in humans[66]. An optically and acoustically transparent plastic membrane was affixed on the participant's skin over the examined position. Both the laser output and ultrasound transducer (UT) were mounted on the same scanning head placed close to the membrane to position the focal point of the ultrasound detector slightly above the skin surface and maximize detection sensitivity. For every measurement, we conducted a calibration step by placing the RSOM transducer in a position so that the most superficial skin signal could be clearly detected. The scanning head contained water as a coupling medium. Two mechanical stages (PI, Germany) were used to move the RSOM head. Both the laser and the controller of the mechanical stages were placed inside a plastic case, which ensured laser safety for all participants, as shown in Fig. S1. The scanning field of view is 4×2 mm^2 with a step size 7.5 μm in the fast axis and 15 μm in the slow axis. The axial and lateral resolutions of RSOM is about 4.5 μm and 18.4 μm respectively, our previous characterization measurements showed that the resolutions generally remained constant throughout the whole dermis (1.5 mm deep)[27,65].

Recruitment, data grouping, and statistical analysis

One hundred and two ($n = 102$) participants with diabetes and 48 age-matched healthy volunteers were scanned in total. Participants with diabetes and healthy volunteers were recruited following approval from the Ethics Committee of the Faculty of Medicine of the Technical University of Munich (Protocol No 109/17S). All participants with and without diabetes gave written informed consent before the planned RSOM examination. RSOM data quality was evaluated based on our previously developed RSOM quality evaluation approach and low-quality data was excluded[67]. Significantly, higher melanin concentrations in skin could decrease the penetration depth of our imaging system. The scanned regions from participants with strong melanin were excluded to minimize the influence of the melanin. Finally, RSOM data from 95 participants with diabetes and 48 healthy volunteers were included in the current analysis. Included participants were split into three main groups based on the presence of relevant complications, such as peripheral neuropathy and macrovascular atherosclerosis and peripheral artery disease (ASCVD/PAD). Group A consisted of 45 participants with diabetes but without complications (neither neuropathy nor ASCVD/PAD). Group B included 25 participants with diabetic neuropathy but without ASCVD/PAD. Group C consisted of 25 participants with diabetic neuropathy and ASCVD/PAD. The presence and severity of peripheral neuropathy was assessed by using the neuropathy symptom score (NSS)[42] and painful symptoms were quantified with a visual analog score ranging between 1 and 10. Peripheral neuropathy was also assessed using the neuropathy disability score (NDS)[43] in the range of 1 to 10, which included 10 g mono-filament testing, tuning fork vibration perception, pin prick perception, and temperature perception.

To quantify the effects of neuropathy, Group B was further divided into two sub-groups with the low NDS and NSS scores ($n = 13$, $1 \le \mathrm{NDS} \le 5$ or $1 \le \mathrm{NSS} \le 5$) and high scores ($n = 12$, $\mathrm{NDS} > 5$ or $\mathrm{NSS} > 5$). Participants with ASCVD/PAD were characterized either by a history of cardiovascular events or by having undergone an arterial revascularization procedure. PAD was characterized by the presence of a clinically relevant stenosis in the peripheral arterial system, as diagnosed by Doppler ultrasound measurements, which was associated with intermittent claudication.

Participant preparation and image acquisition

Participants were asked to consume no caffeine or food for at least 4 h before the RSOM measurements. They were placed in a quiet and dark room and left to relax for at least 5 min. The temperature of the room was held stable at 23 °C during the whole procedure. The measurements were performed with the participants in the supine position. Each participant was scanned at 2 symmetric regions of interest (ROIs, 4×2 mm^2) over the pretibial region of the distal lower limb. The scan of the dominant leg was used for further analysis. The pretibial region was used as representative of skin microcirculation since the participants with diabetes are prone to developing cutaneous alterations at this very position. Each RSOM scan lasted ~70 s. Before each scan, the skin was cleaned with alcohol wipes. Both the participants and the operators used appropriate goggles for laser safety reasons.

Image reconstruction

Acquired RSOM signals were divided into two frequency bands, 10–40 MHz (low) and 40–120 MHz (high), for the 10–120 MHz bandwidth. Signals in the two different bands were independently reconstructed. Reconstructions were based on beam-forming algorithms that generated three-dimensional images[65]. The reconstruction algorithm was accelerated by parallel computing on a graphics processing unit and improved by incorporating the spatial sensitivity field of the detector as a weighting matrix. The reconstruction time of one bandwidth takes

about 5 min with voxel size of the reconstruction grid at 12 μm × 12 μm × 3 μm. The two reconstructed images R_{low} and R_{high} corresponded to the low- and high frequency bands. A composite image was constructed by fusing R_{low} into the red channel and R_{high} into the green channel of an RGB image. A weighting factor was introduced for modulating the intensity of the high-frequency band image. The detail process has been introduced in our previous work[27]. The RSOM images can be rendered by taking the maximum intensity projections of the reconstructed images along the slow axis or the depth direction as shown in Fig. 2.

Data quality control

For this study, we recruited 103 participants with diabetes and 48 healthy volunteers and recorded 302 RSOM measurements (two scans per person). Our previous studies have shown that motion can significantly affect image quality, although our motion correction algorithms can offer marked improvements[67,68]. However, various motions from physiological displacements due to arterial pulsation and heartbeat and unintentional movements of the participant may lead to inconsistent motion correction improvements. Therefore, we developed a quality control scheme based on the amount of motion in the raw data that classifies the quality of data collected. The quality control scheme enables the selection of high-quality datasets, in which the motion is minimal enough for the motion-correction algorithm to correct, resulting in consistent correction improvements and uniform image quality for quantitative analysis[68]. After the data quality evaluation, RSOM datasets of 8 participants with diabetes were excluded due to serious motion and low image quality.

Skin layer and microvasculature segmentation and calculation of RSOM-based biomarkers

For layer segmentation, RSOM images were first flattened based on our surface detection approach[68]. The reconstructed volume of the selected frequency band (10–40 MHz) was split into four stacks with 0.5 mm thickness along the slow scanning axis. Then, the epidermis layer in the MIP image of each stack was automatically segmented by a graph theory and dynamic programming-based approach (see Fig. S2)[40]. The segmented boundaries of the epidermis layer from the four stacks were smoothed to achieve the final segmented results, as shown in (Figs. 1c and S2). The thickness of the epidermis layer was calculated as the average width of the four segmented boundaries. Additionally, the signal density of the epidermis layer was determined as the ratio between the sum of the pixel intensity in the epidermis layer and the total segmented volume of the epidermis layer in the $4 \times 2\ mm^2$ scanning region.

The dermis layer was segmented starting from the bottom boundary of the epidermis layer and extending 1.5 mm deep. In the $4 \times 2\ mm^2$ scanning region, the total blood volume in the segmented dermis layer was calculated as ratio $\left(\frac{N}{T}\right) * 100$, where N represents the number of voxels with intensities above 20% of the maximum voxel intensity, and T is the total voxel number inside the $4 \times 2 \times 1.5\ mm^3$ volume. Afterwards, the vascular mask in the dermis was segmented by the multi-scale matched filter-based vessel segmentation algorithm, as shown in (Fig. 1d)[41]. Based on the mask, vessel boundaries were extracted, and the corresponding width of the boundaries was calculated as the vessel diameter (Figs. 1d and Fig. S3). Then, the centerlines of vessel boundaries were extracted, and junction points of the centerlines were counted as the total vessel number (see Fig. S3). To reduce noise or artifacts, we removed isolated vessels with lengths <5 pixels (20 μm spatial resolution divided by 3 μm pixel size is ~7). The total vessel number was further divided into the small vessel group and the large vessel group, which can be used to investigate the diabetes effects on different size of vessels. The small vessel number was determined based on the number of junction points, where the average diameter of the connected vessel was <40 μm. Correspondingly, the large vessel number was computed as the number of junction points, where the average diameter of the connected vessel was >40 μm. The 40 μm cut-off is a popular value for differentiating small arterioles and venules from larger or even smaller (5–10 μm) capillaries[69]. Furthermore, smaller vessels (<40 μm) reside only within the epineurium and endoneurium[70], and endoneurial microvessels are affected with the diabetic nerves resulting in impaired blood supply (vasa nervorum) and thus diabetic neuropathy[71]. We also analyzed this cut-off value of 40 μm based on vessel diameter distributions of 20 healthy volunteers and 20 participants with diabetes as shown in Fig. S5. The vessel diameter was equally categorized into 10 groups according to size (10 μm size ranges from 10 μm in diameter to 100 μm or more than 100 μm to investigate the effects of diabetes on different vascular beds. We noticed that more significant differences of vessel diameter were found above the cut-off value of 40 μm when comparing healthy participants against participants with diabetes. Depending on the vessel characteristics of the studied participants with and without diabetes, the cut-off value can be altered to maximize sensitivity or specificity for the intended application. In addition, the relation between RSOM features and age (see Fig. S6), disease duration (see Fig. S7), body mass index (BMI) (see Fig. S8), and HbA1c values (see Fig. S9) were investigated and shown in the supplementary results. We found that these parameters did not show obvious correlation with the RSOM biomarkers and thus they did not significantly influence the outcome of our study.

Validation of the layer and vessel segmentation methods

The accuracy of the RSOM biomarker computation was determined by the layer and vessel segmentation methods. In RSOM images, the epidermal layer signal mostly derives from the melanin generating a low frequency layer structure, while the microvasculature contains higher frequency contents. It is very easy to separate visually the epidermal layer from the dermal vasculature in RSOM images. To validate the layer segmentation method, we compared the results of the proposed automatic segmentation method with the manual segmentation performed by two well-trained and independent observers as shown in Fig. S2. The correlation coefficients between the automatic and manual segmentation methods are 0.92 (Observer 1) and 0.96 (Observer 2). Furthermore, we collected RSOM data from the skin of the hip area (4×2 mm^2) of 8 healthy mice and compared with the corresponding histological images. The animal measurements were performed in full compliance with the institutional guidelines of the Helmholtz Center Munich and with approval from the Government District of Upper Bavaria. All scanning parameters of the mouse measurements followed the same configurations of the human measurements. The RSOM datasets of the 8 mice were reconstructed and analyzed following the same analysis procedure of the human data. The RSOM image of mouse skin was segmented into dermis and hypodermis layers, and the vasculature in the hypodermis layer was further segmented to compute the RSOM biomarker (total blood volume). In addition, the dermis thickness of each mouse was calculated in both histological and corresponding RSOM images. CD31 immunostaining was performed to evaluate vessel footprints. The total blood volume in the histological image was computed as the ratio between the vessel marker area and the total hypodermis area, while the total blood volume of RSOM mouse image was computed using the same analysis method of the participants with diabetes data. As shown in Fig. S4, the dermis thicknesses and total blood volumes showed very good correlations between values obtained from the histological and RSOM images (the correlation coefficients values are 0.94 and 0.91 respectively). Furthermore, our previous work has made a comparison of capillary imaging by conventional nailfold capillaroscopy and RSOM[55]. The capillary diameter and capillary density, which computed from the segmented RSOM images, were correlated well with the nailfold capillaroscopy. Moreover, our approaches to segment RSOM skin features (including the epidermis layer thickness and dermal vasculature) were validated in previous work using histology[27].

Statistics

A total number of 95 participants with diabetes and 48 healthy volunteers were grouped together to compute biomarkers. All metrics were displayed into column table with mean value and standard deviations as error bar. Information of age/disease duration /Hb1Ac /BMI between healthy controls and participants with diabetes, and differences between the groups with diabetes and subgroups or individuals with Type 1 or Type 2 diabetes were evaluated by the mean of the Mann–Whitney U-test as shown in Table 1 and supplementary Table I to Table V. To assess the significance of the statistical differences for the metrics between healthy and diabetic groups, and sub-groups among participants with diabetes, we performed parametric tests (unpaired t test) for normally distributed data; otherwise, nonparametric tests (Mann–Whitney U test) were applied. We have computed the Spearman correlation to show the relationship among age/disease duration /HbA1c /BMI with the vascular biomarkers TBV (Total blood volume) and SVN (Small vessel number). In addition, we also applied multivariate logistic regression analysis to compute the statistics of the two biomarkers TBV and SVN between different diabetic groups with adjustment of age/disease duration /Hb1Ac /BMI, and in the analysis of the diabetic neuropathy groups as well. For the multiple regression analysis, all variables that were significantly associated with RSOM biomarkers in the univariate analysis were included in the model. Statistical significance was defined at $P < 0.05$.

Acknowledgements

This project has received funding from the European Union's Horizon 2020 research and innovation programme under grant agreement No 687866 (INNODERM) and No 871763 (WINTHER), from the European Research Council (ERC) under the European Union's Horizon 2020 research and innovation programme under grant agreement No 694968 (PREMSOT) and from Helmholtz Zentrum München through Physician Scientists for Groundbreaking Projects, in part by the Helmholtz Association of German Research Center, through the Initiative and Networking Fund, i3 (ExNet-0022-Phase2-3), and from the DZHK (German Centre for Cardiovascular Research; FKZ 81Z0600104). We thank Dr. Robert J. Wilson and Dr Serene Lee for their attentive reading and improvements of the manuscript. We express our gratitude to the staff at the Diabetes Center in Marienplatz, Munich, Germany as well as the Department for Vascular and Endovascular Surgery, Klinikum rechts der Isar, Technical University of Munich (TUM), Germany, for their valuable assistance in conducting the study presented here.

Author details

[1]Institute of Biological and Medical Imaging, Helmholtz Zentrum München, Neuherberg, Germany. [2]Chair of Biological Imaging at the Central Institute for Translational Cancer Research (TranslaTUM), School of Medicine, Technical University of Munich, Munich, Germany. [3]Department for Vascular and Endovascular Surgery, Klinikum rechts der Isar, Technical University of Munich (TUM), Munich, Germany. [4]DZHK (German Centre for Cardiovascular Research), partner site Munich Heart Alliance, Munich, Germany. [5]Diabetes Center at Marienplatz, Munich, Germany. [6]Forschergruppe Diabetes e.V., Helmholtz Zentrum München, Neuherberg, Germany. [7]Institute of Diabetes Research, Helmholtz Zentrum München, Neuherberg, Germany

Author contributions

H.H. designed the study, built the imaging system, performed the experiments, collected and analyzed the data, generated the figures, and wrote the paper. N.-A.F. designed the study, recruited the participants with and without diabetes, performed the experiments, collected the data, interpreted the results, and wrote the paper. A.K. designed the study, recruited the participants with and without diabetes, interpreted the results, and wrote the paper. M.O. built the imaging system, performed the experiments, and collected data.

J.A. built the imaging system and provided conceptual input. J.L. recruited participants with diabetes. M.K. recruited participants with diabetes. M.F. recruited the participants with diabetes and provided conceptual input. H.-H.E. provided conceptual input. A.Z. provided conceptual input. V.N. provided conceptual input, supervised, led the research, and wrote the paper.

Funding
Open Access funding enabled and organized by Projekt DEAL.

Conflict of interest
V.N. is an equity owner and consultant for iThera Medical GmbH, Munich, Germany.

Supplementary information The online version contains supplementary material available at https://doi.org/10.1038/s41377-023-01275-3.

Received: 15 February 2023 Revised: 10 August 2023 Accepted: 28 August 2023
Published online: 18 September 2023

References

1. Guariguata, L. et al. Global estimates of diabetes prevalence for 2013 and projections for 2035. *Diabetes Res. Clin. Pract.* **103**, 137–149 (2014).
2. NCD Risk Factor Collaboration (NCD-RisC). Worldwide trends in diabetes since 1980: a pooled analysis of 751 population-based studies with 4·4 million participants. *Lancet* **387**, 1513–1530 (2016).
3. Barrett, E. J. et al. Diabetic microvascular disease: an endocrine society scientific statement. *J. Clin. Endocrinol. Metab.* **102**, 4343–4410 (2017).
4. Cheung, C. Y. et al. The clinical implications of recent studies on the structure and function of the retinal microvasculature in diabetes. *Diabetologia* **58**, 871–885 (2015).
5. Papanas, N., Vinik, A. I. & Ziegler, D. Neuropathy in prediabetes: does the clock start ticking early? *Nat. Rev. Endocrinol.* **7**, 682–690 (2011).
6. Baron, R., Binder, A. & Wasner, G. Neuropathic pain: diagnosis, pathophysiological mechanisms, and treatment. *Lancet Neurol.* **9**, 807–819 (2010).
7. Caballero, A. E. et al. Microvascular and macrovascular reactivity is reduced in subjects at risk for type 2 diabetes. *Diabetes* **48**, 1856–1862 (1999).
8. Greenman, R. L. et al. Early changes in the skin microcirculation and muscle metabolism of the diabetic foot. *Lancet* **366**, 1711–1717 (2005).
9. Strain, W. D. & Paldánius, P. M. Diabetes, cardiovascular disease and the microcirculation. *Cardiovasc. Diabetol.* **17**, 57 (2018).
10. Sörensen, B. M. et al. Prediabetes and type 2 diabetes are associated with generalized microvascular dysfunction: the maastricht study. *Circulation* **134**, 1339–1352 (2016).
11. Sörensen, B. M. et al. Cardiovascular risk factors as determinants of retinal and skin microvascular function: the Maastricht Study. *PLoS ONE* **12**, e0187324 (2017).
12. Ziegler, D. et al. Early detection of nerve fiber loss by corneal confocal microscopy and skin biopsy in recently diagnosed type 2 diabetes. *Diabetes* **63**, 2454–2463 (2014).
13. Azmi, S. et al. Corneal confocal microscopy identifies small-fiber neuropathy in subjects with impaired glucose tolerance who develop type 2 diabetes. *Diabetes Care* **38**, 1502–1508 (2015).
14. Papanas, N. & Ziegler, D. Corneal confocal microscopy: recent progress in the evaluation of diabetic neuropathy. *J. Diabetes Investig.* **6**, 381–389 (2015).
15. Nouveau-Richard, S. et al. In vivo epidermal thickness measurement: ultrasound vs. confocal imaging. *Skin Res. Technol.* **10**, 136–140 (2004).
16. Chao, C. Y. L., Zheng, Y. P. & Cheing, G. L. Epidermal thickness and biomechanical properties of plantar tissues in diabetic foot. *Ultrasound Med. Biol.* **37**, 1029–1038 (2011).
17. Van Mulder, T. J. S. et al. High frequency ultrasound to assess skin thickness in healthy adults. *Vaccine* **35**, 1810–1815 (2017).
18. Collier, A. et al. Relationship of skin thickness to duration of diabetes, glycemic control, and diabetic complications in male IDDM patients. *Diabetes Care* **12**, 309–312 (1989).
19. Yudovsky, D., Nouvong, A. & Pilon, L. Hyperspectral imaging in diabetic foot wound care. *J. Diabetes Sci. Technol.* **4**, 1099–1113 (2010).
20. Nouvong, A. et al. Evaluation of diabetic foot ulcer healing with hyperspectral imaging of oxyhemoglobin and deoxyhemoglobin. *Diabetes Care* **32**, 2056–2061 (2009).
21. Hsu, P. C. et al. Nailfold capillary abnormalities are associated with type 2 diabetes progression and correlated with peripheral neuropathy. *Medicine* **95**, e5714 (2016).
22. Uyar, S. et al. Assessment of the relationship between diabetic retinopathy and nailfold capillaries in type 2 diabetics with a noninvasive method: nailfold videocapillaroscopy. *J. Diabetes Res.* **2016**, 7592402 (2016).
23. Argarini, R. et al. Visualizing and quantifying cutaneous microvascular reactivity in humans by use of optical coherence tomography: impaired dilator function in diabetes. *Am. J. Physiol.: Endocrinol. Metab.* **319**, E923–E931 (2020).
24. Untracht, G. R. et al. Pilot study of optical coherence tomography angiography-derived microvascular metrics in hands and feet of healthy and diabetic people. *Sci. Rep.* **13**, 1122 (2023).
25. Yagihashi, S. Clinical staging of type 2 diabetes: the time has come. *J. Diabetes Investig.* **3**, 1–2 (2012).
26. Insel, R. A. et al. Staging presymptomatic type 1 diabetes: a scientific statement of JDRF, the Endocrine Society, and the American Diabetes Association. *Diabetes Care* **38**, 1964–1974 (2015).
27. Aguirre, J. et al. Precision assessment of label-free psoriasis biomarkers with ultra-broadband optoacoustic mesoscopy. *Nat. Biomed. Eng.* **1**, 0068 (2017).
28. Omar, M., Aguirre, J. & Ntziachristos, V. Optoacoustic mesoscopy for biomedicine. *Nat. Biomed. Eng.* **3**, 354–370 (2019).
29. Schwarz, M. et al. Three-dimensional multispectral optoacoustic mesoscopy reveals melanin and blood oxygenation in human skin in vivo. *J. Biophoton.* **9**, 55–60 (2016).
30. Schwarz, M. et al. Optoacoustic dermoscopy of the human skin: tuning excitation energy for optimal detection bandwidth with fast and deep imaging in vivo. *IEEE Trans. Med. Imaging* **36**, 1287–1296 (2017).
31. He, H. L. et al. Fast raster-scan optoacoustic mesoscopy enables assessment of human melanoma microvasculature in vivo. *Nat. Commun.* **13**, 2803 (2022).
32. Hindelang, B. et al. Enabling precision monitoring of psoriasis treatment by optoacoustic mesoscopy. *Sci. Transl. Med.* **14**, eabm8059 (2022).
33. Chen, C. L. & Wang, R. K. Optical coherence tomography based angiography [Invited]. *Biomed. Opt. Express* **8**, 1056–1082 (2017).
34. Choi, W. et al. Three-dimensional multistructural quantitative photoacoustic and US imaging of human feet in vivo. *Radiology* **303**, 467–473 (2022).
35. Li, J. et al. Spatial heterogeneity of oxygenation and haemodynamics in breast cancer resolved in vivo by conical multispectral optoacoustic mesoscopy. *Light Sci. Appl.* **9**, 57 (2020).
36. Razansky, D., Buehler, A. & Ntziachristos, V. Volumetric real-time multispectral optoacoustic tomography of biomarkers. *Nat. Protoc.* **6**, 1121–1129 (2011).
37. Deán-Ben, X. L. & Razansky, D. Optoacoustic imaging of the skin. *Exp. Dermatol.* **30**, 1598–1609 (2021).
38. Aguirre, J. et al. Broadband mesoscopic optoacoustic tomography reveals skin layers. *Opt. Lett.* **39**, 6297–6300 (2014).
39. Brown, E. L. et al. Quantification of vascular networks in photoacoustic mesoscopy. *Photoacoustics* **26**, 100357 (2022).
40. Chiu, S. J. et al. Automatic segmentation of seven retinal layers in SDOCT images congruent with expert manual segmentation. *Opt. Express* **18**, 19413–19428 (2010).
41. Sofka, M. & Stewart, C. V. Retinal vessel centerline extraction using multiscale matched filters, confidence and edge measures. *IEEE Trans. Med. Imaging* **25**, 1531–1546 (2006).
42. Maser, R. E. et al. Measuring diabetic neuropathy: assessment and comparison of clinical examination and quantitative sensory testing. *Diabetes Care* **12**, 270–275 (1989).
43. Feldman, E. L. et al. A practical two-step quantitative clinical and electrophysiological assessment for the diagnosis and staging of diabetic neuropathy. *Diabetes Care* **17**, 1281–1289 (1994).
44. Kanne, J. P. et al. Beyond skin deep: thoracic manifestations of systemic disorders affecting the skin. *RadioGraphics* **31**, 1651–1668 (2011).
45. Errico, C. et al. Ultrafast ultrasound localization microscopy for deep super-resolution vascular imaging. *Nature* **527**, 499–502 (2015).
46. Barchetta, I. et al. High prevalence of capillary abnormalities in patients with diabetes and association with retinopathy. *Diabet. Med.* **28**, 1039–1044 (2011).

47. Karbalaie, A. et al. Practical issues in assessing nailfold capillaroscopic images: a summary. *Clin. Rheumatol.* **38**, 2343–2354 (2019).
48. Mariampillai, A. et al. Speckle variance detection of microvasculature using swept-source optical coherence tomography. *Opt. Lett.* **33**, 1530–1532 (2008).
49. Srinivasan, V. J. et al. Rapid volumetric angiography of cortical microvasculature with optical coherence tomography. *Opt. Lett.* **35**, 43–45 (2010).
50. Kee, A. R., Wong, T. Y. & Li, L. J. Retinal vascular imaging technology to monitor disease severity and complications in type 1 diabetes mellitus: a systematic review. *Microcirculation* **24**, e12327 (2017).
51. Hafner, J. et al. Regional patterns of retinal oxygen saturation and microvascular hemodynamic parameters preceding retinopathy in patients with type II diabetes. *Investig. Ophthalmol. Vis. Sci.* **58**, 5541–5547 (2017).
52. Zakharov, P. et al. Full-field optical coherence tomography for the rapid estimation of epidermal thickness: study of patients with diabetes mellitus type 1. *Physiol. Meas.* **31**, 193–205 (2010).
53. Shin, Y. I. et al. Peripapillary microvasculature in patients with diabetes mellitus: an optical coherence tomography angiography study. *Sci. Rep.* **9**, 15814 (2019).
54. Vujosevic, S. et al. Early detection of microvascular changes in patients with diabetes mellitus without and with diabetic retinopathy: comparison between different swept-source OCT-a instruments. *J. Diabetes Res.* **2019**, 2547216 (2019).
55. Aguirre, J. et al. Assessing nailfold microvascular structure with ultra-wideband raster-scan optoacoustic mesoscopy. *Photoacoustics* **10**, 31–37 (2018).
56. Berezhnoi, A. et al. Assessing hyperthermia-induced vasodilation in human skin in vivo using optoacoustic mesoscopy. *J. Biophoton.* **11**, e201700359 (2018).
57. Malik, R. A. et al. Microangiopathy in human diabetic neuropathy: relationship between capillary abnormalities and the severity of neuropathy. *Diabetologia* **32**, 92–102 (1989).
58. Chao, C. Y. L., Zheng, Y. P. & Cheing, G. L. The association between skin blood flow and edema on epidermal thickness in the diabetic foot. *Diabetes Technol. Ther.* **14**, 602–609 (2012).
59. Sohn, E. et al. A novel method to quantify cutaneous vascular innervation. *Muscle Nerve* **62**, 492–501 (2020).
60. Quattrini, C. et al. Reduced vascular endothelial growth factor expression and intra-epidermal nerve fiber loss in human diabetic neuropathy. *Diabetes Care* **31**, 140–145 (2008).
61. Fuchs, D. et al. The association between diabetes and dermal microvascular dysfunction non-invasively assessed by laser Doppler with local thermal hyperemia: a systematic review with meta-analysis. *Cardiovasc. Diabetol.* **16**, 11 (2017).
62. Roustit, M. & Cracowski, J. L. Assessment of endothelial and neurovascular function in human skin microcirculation. *Trends Pharmacol. Sci.* **34**, 373–384 (2013).
63. Bajwa, A. et al. Assessment of tissue perfusion in the lower limb: current methods and techniques under development. *Circ. Cardiovasc. Imaging* **7**, 836–843 (2014).
64. Themstrup, L. et al. Validation of Dynamic optical coherence tomography for non-invasive, in vivo microcirculation imaging of the skin. *Microvasc. Res.* **107**, 97–105 (2016).
65. Omar, M., Gateau, J. & Ntziachristos, V. Raster-scan optoacoustic mesoscopy in the 25-125 MHz range. *Opt. Lett.* **38**, 2472–2474 (2013).
66. American National Standards Institute. ANSI Z136.1, – Safe Use of Lasers. (Laser Institute of America, 2022).
67. Aguirre, J. et al. Motion quantification and automated correction in clinical RSOM. *IEEE Trans. Med. Imaging* **38**, 1340–1346 (2019).
68. Schwarz, M. et al. Motion correction in optoacoustic mesoscopy. *Sci. Rep.* **7**, 10386 (2017).
69. Russell, R. D. et al. Oral glucose challenge impairs skeletal muscle microvascular blood flow in healthy people. *Am. J. Physiol. Endocrinol. Metab.* **315**, E307–E315 (2018).
70. Klein, C. J. Autoimmune-mediated peripheral neuropathies and autoimmune pain. *Handb. Clin. Neurol.* **133**, 417–446 (2016).
71. Yagihashi, S., Mizukami, H. & Sugimoto, K. Mechanism of diabetic neuropathy: where are we now and where to go? *J. Diabetes Investig.* **2**, 18–32 (2011).

Supplementary Information for

Opening a window to skin biomarkers for diabetes stage with optoacoustic mesoscopy

Figure S1. **Picture of the portable RSOM imaging system**. The laser source and the stage controller are contained within a plastic suitcase, creating a controlled laser safety environment during the measurement of the participants with or without diabetes mellitus.

Layer segmentation method and validation. To segment the epidermis (EP) layer, RSOM images were first flattened based on our surface detection approach[1]. The reconstructed volume of the selected frequency band [10-40 MHz, Fig. S2a] was split into four stacks with 0.5 mm thickness along the slow scanning axis. Then, the epidermis layer in the MIP image of each stack was automatically segmented by a graph theory and dynamic programming-based approach[2]. To validate the layer segmentation method, we randomly selected 30 RSOM images (from the healthy volunteers and participants with diabetes) and compared the results of the automatic segmentation method with the manual segmentation performed by two well-trained and independent observers as shown in Fig. S2f. The correlation coefficients between the automatic and manual segmentation methods are 0.92 (Observer 1) and 0.96 (Observer 2).

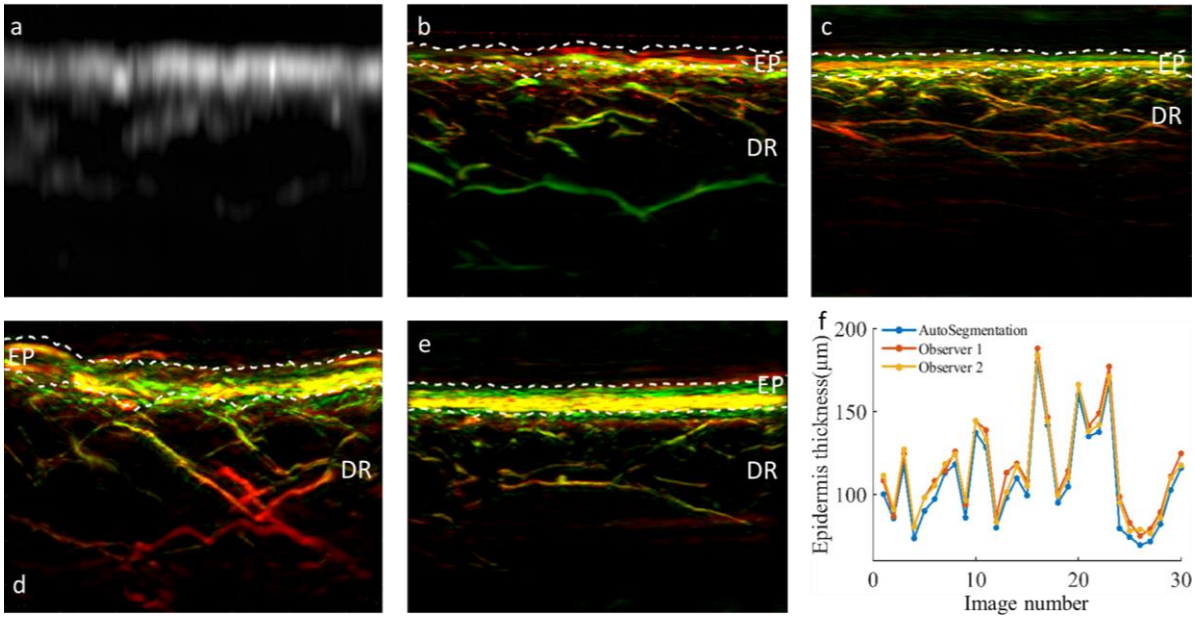

Figure S2. **RSOM image layer segmentation**. (a) The reconstructed RSOM image of low frequency (10-40 MHz) signals, which mainly contain the epidermis layer structure originated from the skin pigment melanin. (b) The corresponding reconstructed RSOM image of (a) in the full frequency bandwidth, where the white dashed lines segment the epidermis layer. (c-e) Validation results of the layer segmentation on RSOM images of several healthy volunteers and participants with diabetes. (f) Comparisons of the layer segmentation results of 30 RSOM images between the automatic and manual segmentation methods by two observers based on human vision showing good correlations. EP: Epidermis, DR: Dermis.

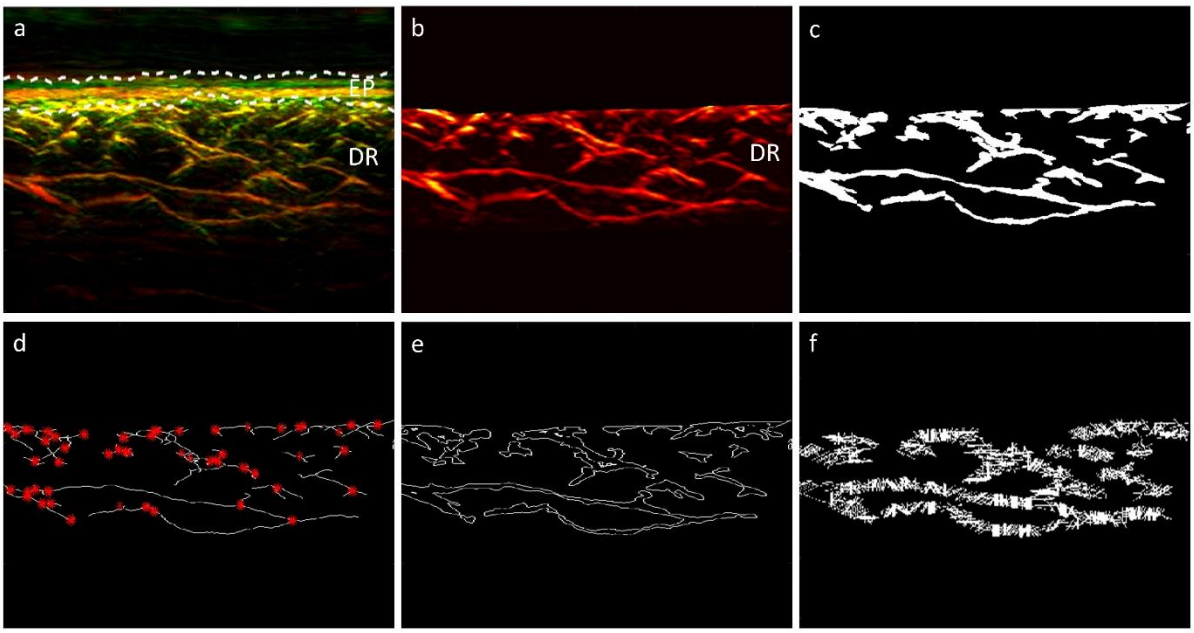

Figure S3. **Automatic vessel segmentation of the dermal vasculature and computation of biomarkers**. (a) Cross-sectional RSOM image from a healthy volunteer. The white dashed lines segment the epidermal layer and dermis layer; (b) The segmented dermal layer; (c) The binary image of the segmented dermal vasculature; (d) The centerlines of the segmented binary image (c); Red dots mark the branches of vessels, used to count the vessel number; (e) The segmented boundaries of the binary image (c); (f) Computation of the diameter of the segmented vessel boundaries (e). EP: Epidermis, DR: Dermis.

Validations of the layer and vessel segmentation method. To validate the RSOM computed biomarkers, we collected RSOM data from the skin of the hip area (4×2 mm^2) of 8 healthy mice and compared with the corresponding histological images. As shown in Fig. S4a and S4c, the RSOM image of the mouse skin was segmented into dermis and hypodermis layers, and the vasculature in the hypodermis layer was further segmented to compute the total blood volume. In addition, the dermis thickness of each mouse was calculated in both histological (Fig. S4c) and corresponding RSOM images (Fig. S4a). CD31 immunostaining was performed to evaluate vessel footprints (black arrows in Fig. S4c). The total blood volume in the histological image was computed as the ratio between the vessel marker area and the total hypodermis area, while the RSOM biomarker (total blood volume) was computed using the same analysis method of the human data. The dermis thickness and total blood volume showed very good correlations between the histological and RSOM images (the correlation coefficient values are 0.94 and 0.91, respectively) shown in Fig. S4d.

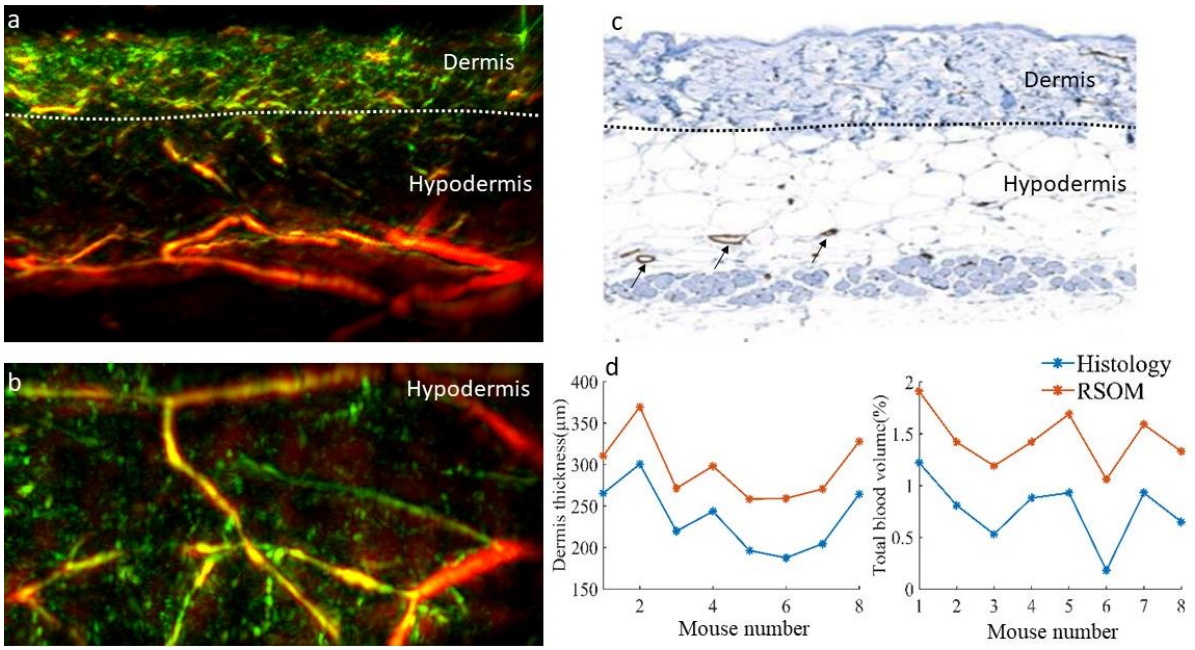

Figure S4. **Validations of layer and vessel segmentation methods on animal data with histology**. (a) Cross-sectional RSOM image of the skin obtained from the hip area of a healthy male mouse. The dermis and hypodermis layers of mouse skin were automatically segmented as indicated by the white dashed line. (b) Corresponding MIP RSOM image of the microvasculature in the coronal view of the hypodermis layer. (c) CD31 immunostaining of the scanned mouse skin, where the black dashed line separates the dermis and hypodermis, in good correlation with the RSOM image (a). The vessels are indicated by the black arrows. To validate the segmentation method, the results of automatic segmentation of RSOM images were compared against manual segmentation of histological images using 8 mice of different weights. (d) The dermis thicknesses and total blood volumes were calculated from histological images and RSOM images, with high correlations found between values obtained from RSOM and histological images.

Selection of the cut-off vessel diameter to distinguish between participants with and without diabetes. In this study, vessels were categorized according to size (10 µm size ranges from 10 µm in diameter to 100 µm or more than 100 µm) to investigate the effects of diabetes on different vascular beds. The cut-off value was determined based on vessel diameter distributions of 20 healthy volunteers and 20 participants with diabetes as shown in Fig. S5. We noticed that more significant differences were found above the cut-off value of 40 µm when comparing healthy participants against participants with diabetes. Depending on the vessel characteristics of the study participants with and without diabetes, the cut-off value can be altered to maximize sensitivity or specificity for the intended application.

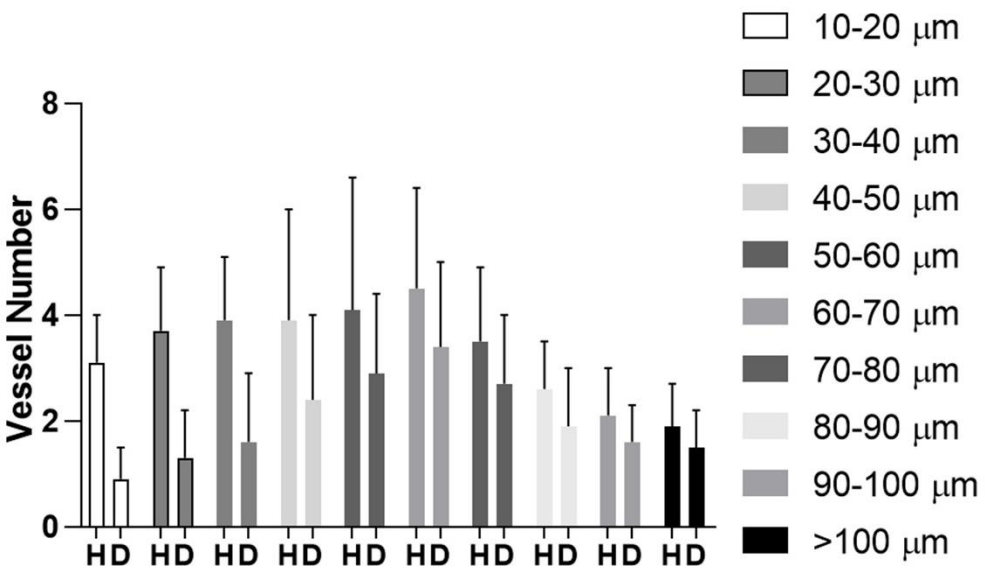

Figure S5. **Vessel number distributions in healthy volunteers and participants with diabetes**. All vessels of 20 healthy (H) volunteers and 20 participants with diabetes (D) are categorized into 10 groups based on the vessel diameter. Values are means with standard deviations shown as error bars.

To understand the effects of diabetes on the vascular biomarker, we computed the Spearman correlation value between age/disease duration/HbA1c/BMI with the vascular biomarker TBV and found no significant correlations as shown in supplementary Table I. We further applied multivariate logistic regression analysis to estimate the significance of TBV between the healthy and diabetic groups including variables of age and BMI, which showed no significant association between the vascular biomarker and patient parameters.

Table I Correlation and multivariate logistic regression analysis between vascular biomarker (Total blood volume: TBV) and patient parameters.

	Correlation*		Multivariate**	
	r	*p*	*β*	*p*
Age (years)	-0.08	0.54	0.92	0.0007
Disease duration (years)	-0.04	0.69	n/a	n/a
HbA1c (%)	-0.014	0.90	n/a	n/a
BMI (kg/m²)	-0.13	0.42	0.83	0.0004

Note: *The Spearman correlation value was calculated between TBV and the various patient parameters and no significant correlations were found; **Multivariate logistic regression analysis was applied to compute the significance of vascular biomarker TBV between the healthy and participants with diabetes groups including the variables of age and BMI, which still show significant differences between the healthy and patient groups. n/a: Not applicable. BMI: Body mass index, HbA1c: Glycated hemoglobin.

For participants with neuropathy, we carefully compared age, disease duration, HbA1c and BMI between NC (participants with diabetes and no complications), LN [participants with diabetes and low score neuropathy (1≤ NDS ≤ 5 or 1≤NSS ≤ 5)] and HN [participants with diabetes and high score neuropathy (NDS > 5 or NSS > 5)] as shown in supplementary Table II. There are no significant differences in age, HbA1c and BMI values among the three groups and only the duration of disease between the NC and LN differs significantly. We also computed the Spearman correlation between age/ duration of disease /HbA1c/BMI with the vascular biomarker TBV of the three groups and we found no significant correlation as shown in supplementary Table III.

Table II Participant information for diabetic neuropathy analysis.

	NC (n=45)	LN (n=13)	P value*	HN (n=12)	P value**
Age (years)	63.1±18.7	68.8±8.3	ns	71.3±10.8	ns
Disease duration (years)	12.1±11.2	28.7±18.9	<0.05	27.1±14.2	ns
HbA1c (%)	7.1±1.6	7.2±0.7	ns	7.3±0.7	ns
BMI (kg/m²)	27.4±7.6	30.6±10.7	ns	29.8±6.0	ns

Note: * NC group versus LN group; **LN group versus HN group [participants with diabetes and high score neuropathy (NDS > 5 or NSS > 5). NC: participants with diabetes and no complications, LN: participants with diabetes and low score neuropathy (1 ⩽ NDS ⩽ 5 or 1⩽NSS ⩽ 5) and HN: participants with diabetes and high score neuropathy (NDS > 5 or NSS > 5). We performed parametric tests (unpaired t-test) for normally distributed data; otherwise, non-parametric tests (Mann Whitney U test) were applied. Statistical significance was assumed at $P < 0.05$. ns: Not statistically significant. BMI: Body mass index, HbA1c: Glycated hemoglobin.

Table III Correlation between vascular biomarker (Total blood volume: TBV) and participant parameters in the diabetic neuropathy groups.

Variable	NC		LN		HN	
	r	*p*	*r*	*p*	*r*	*p*
Age (years)	-0.08	0.41	-0.11	0.41	-0.18	0.42
Disease duration (years)	-0.04	0.41	-0.17	0.27	-0.09	0.31
HbA1c (%)	0.019	0.43	-0.13	0.34	-0.24	0.29
BMI (kg/m²)	-0.19	0.57	-0.14	0.41	-0.07	0.38

Note: The Spearman correlation value was computed between TBV and the patient parameters in each group with no significant correlations found. NC: participants with diabetes and no complications, LN: participants with diabetes and low score neuropathy (1⩽ NDS ⩽ 5 or 1⩽NSS ⩽ 5) and HN: participants with diabetes and high score neuropathy (NDS > 5 or NSS > 5). BMI: Body mass index, HbA1c: Glycated hemoglobin.

To examine the effects of age, disease duration, HbA1c and BM, as shown in supplementary Table IV, we applied multivariate logistic regression analysis including the variables of age, duration of the disease, HbA1c and BMI, which did not show significant effects in the statistical analysis among the three groups NC, LN, and HN.

Table IV Multivariate logistic regression analysis of participant groups with neuropathy, including patient parameters**.**

Patient parameters	Patient groups	*P value*[*]	*P value with adjustment*[**]
Age (years)	NC and LN	<0.05	<0.05
	LN and HN	<0.001	<0.001
Disease duration (years)	NC and LN	<0.05	<0.05
	LN and HN	<0.001	<0.001
HbA1c (%)	NC and LN	<0.05	<0.05
	LN and HN	<0.001	<0.001
BMI (kg/m²)	NC and LN	<0.05	<0.05
	LN and HN	<0.001	<0.001

Note: * We performed parametric tests (unpaired t-test) for normally distributed data; otherwise, nonparametric tests (Mann Whitney U test) were applied. Values of P < 0.05 were considered statistically significant. **Multivariate logistic regression analysis was applied to compute the significance of the vascular biomarker TBV between the patient groups NC and LN, and LN and HN including the variables of age, disease duration, Hb1Ac, and BMI, which did not affect the statistical results. NC: participants with diabetes and no complications, LN: participants with diabetes and low score neuropathy (1⩽ NDS ⩽ 5 or 1⩽ NSS ⩽ 5) and HN: participants with diabetes and high score neuropathy (NDS > 5 or NSS > 5). BMI: Body mass index, HbA1c: Glycated hemoglobin.

We compared the characteristics of participants with type 1 and type 2 diabetes, as shown in supplementary Table V. We found that there were no significant differences in age, Hb1Ac and BMI values between the two groups and that only the type 1 group had significantly longer disease duration compared with the type 2 group.

Table V Characteristics of participants with type 1 and type 2 diabetes

	Type 1 (n=21)	Type 2 (n=74)	P value
Age (years)	67.2±12.4	68.2±11.4	ns
Disease duration (years)	32.0±19.3	16.1±11.5	<0.05
Hb1Ac (%)	7.5±0.8	7.0±1.2	ns
BMI (kg/m²)	27.1±3.4	26.9±8.1	ns

Note: We performed parametric tests (unpaired t-test) for normally distributed data; otherwise, nonparametric tests (Mann Whitney U test) were applied. Statistical significance was assumed at P < 0.05, ns: Not statistically significant. BMI: Body mass index, HbA1c: Glycated hemoglobin.

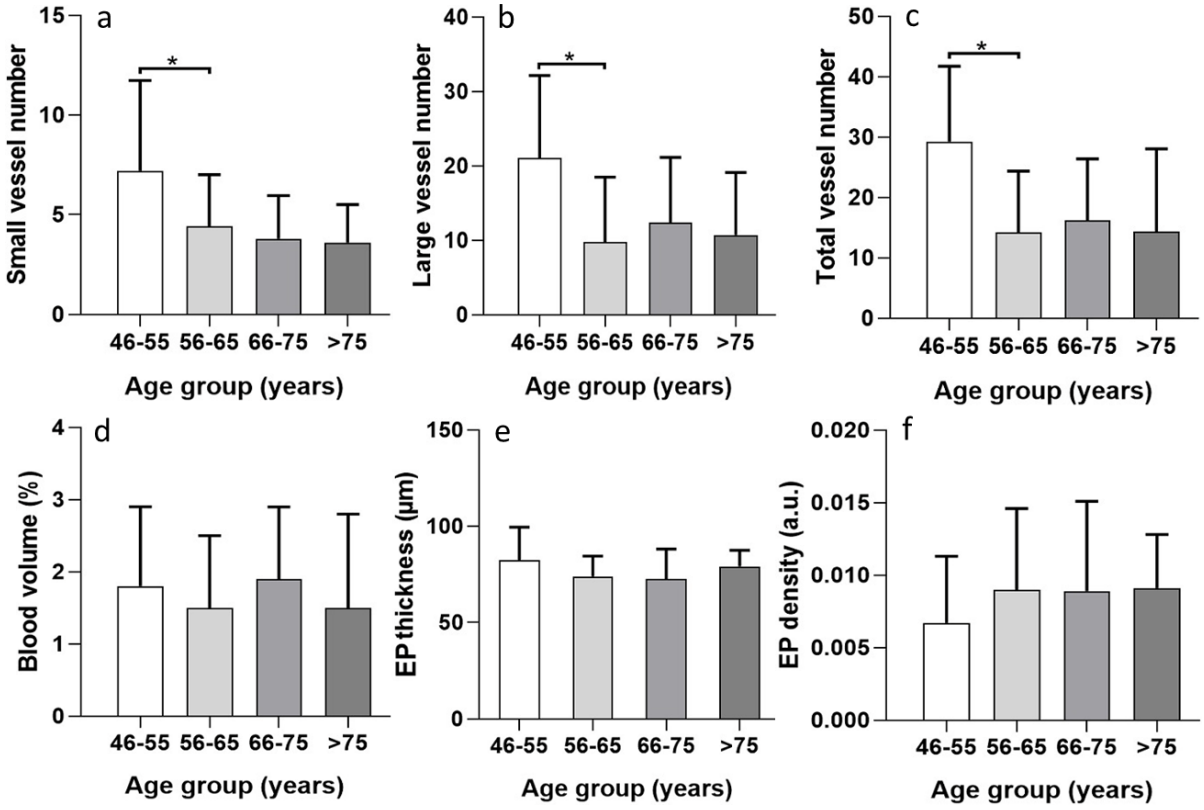

Figure S6. **Quantification of RSOM features in relation to patient ages**. 72 participants with diabetes from the first dataset were grouped based on their ages (years) as follows: 46-55 (n = 15), 56-65 (n = 18), 66-75 (n = 20), >75 (n = 10). Comparisons among age groups for six RSOM features were carried out: (a) Total number of small vessels (with diameter <= 40 μm) in DR layer; (b) Total number of large vessels (diameter > 40 μm) in DR layer; (c) Total number of vessels in DR layer; (d) Total blood volume in DR layer; (e) Thickness of EP layer; (f) Signal density of EP layer. * Represents $P < 0.05$. The numbers of small, large, and total vessels were significantly reduced for 45 to 55-year-old participants when compared to 56 to 65-year-old participants. The vessel number and blood volume decrease with increasing age, however, there is no significant change among the groups (56-65, 66-75 and >75). In addition, age does not obviously affect the Epidermal thickness and the Epidermal signal density. EP: Epidermis, DR: Dermis.

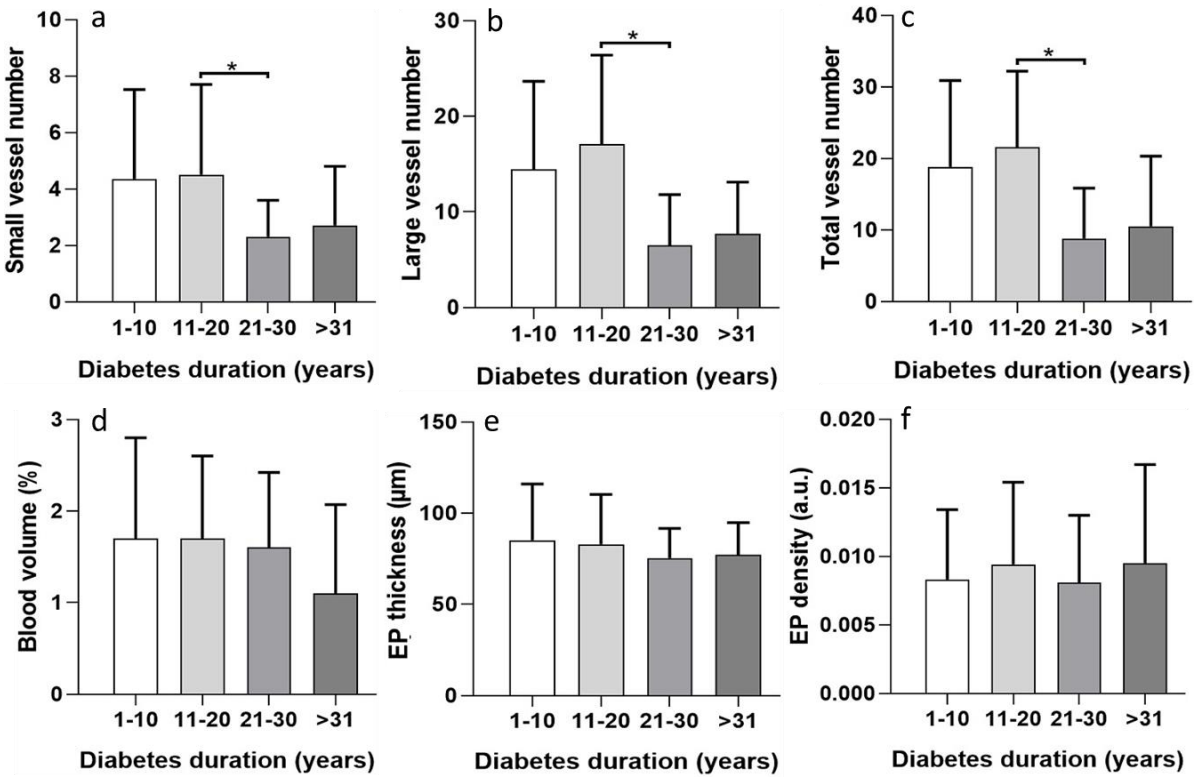

Figure S7. **Quantified RSOM features plotted against diabetes duration**. 72 participants with diabetes from the first dataset were grouped based on disease duration (years) as follows: 1-10 (n =25), 11-20 (n = 18), 21-30 (n = 10), >30 (n = 10). Comparisons amongst disease duration for six RSOM features were carried out: (a) Total number of small vessels (with diameter <= 40 µm) in DR layer; (b) Total number of large vessels (diameter > 40 µm) in DR layer; (c) Total number of vessels in DR layer; (d) Total blood volume in DR layer; (e) Thickness of EP layer; (f) Signal density of EP layer. * Represents $P < 0.05$. The numbers of small, large, and total vessels were significantly reduced in the group with 11 to 20 years of diabetes duration compared to the group with 21 to 30 years of diabetes duration. However, there were no significant changes when the other groups, i.e., 1-10 versus 11-20 or 21-30 versus >31 were compared. Mean blood volume reduced with the increment disease duration. The diabetes duration did not play a significant role in influencing the Epidermal thickness and the Epidermal signal density. EP: Epidermis, DR: Dermis.

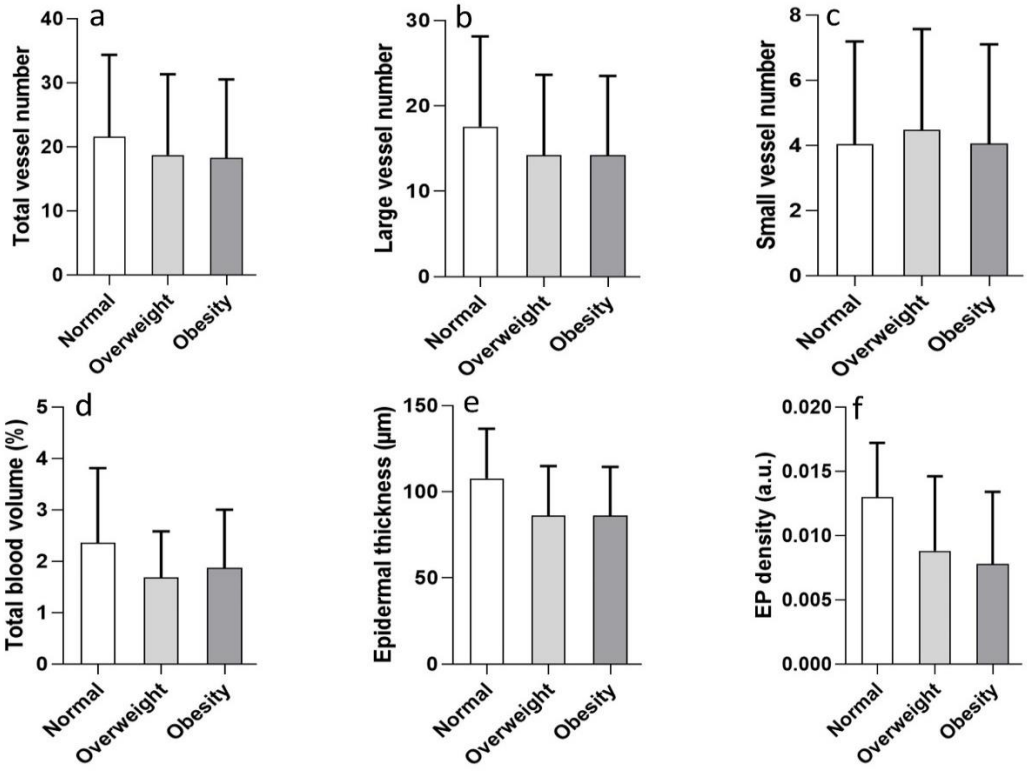

Figure S8. **Quantification of RSOM features in relation to body mass index (BMI).** 72 participants with diabetes from the first dataset were grouped based on BMI values as follows: Normal weight (18.5<BMI<25, n =18), Overweight (25<BMI<30, n = 25), Obesity (BMI>30, n = 20). Comparisons among the three BMI groups were done for six RSOM features: (a) Total number of small vessels (with diameter <= 40 µm) in DR layer; (b) Total number of large vessels (diameter > 40 µm) in DR layer; (c) Total number of vessels in DR layer; (d) Total blood volume in DR layer; (e) Thickness of EP layer; (f) Signal density of EP layer. * Represents $P < 0.05$. It can be observed that the mean numbers of total and large vessels were reduced between the group with normal weight and the overweight group. However, there is no significant difference. Mean blood volume, Epidermal thickness and Epidermal density were all decreased in the overweight and obesity groups compared to the normal weight patient group. However, the BMI values did not play a significant role in influencing RSOM biomarkers. EP: Epidermis, DR: Dermis.

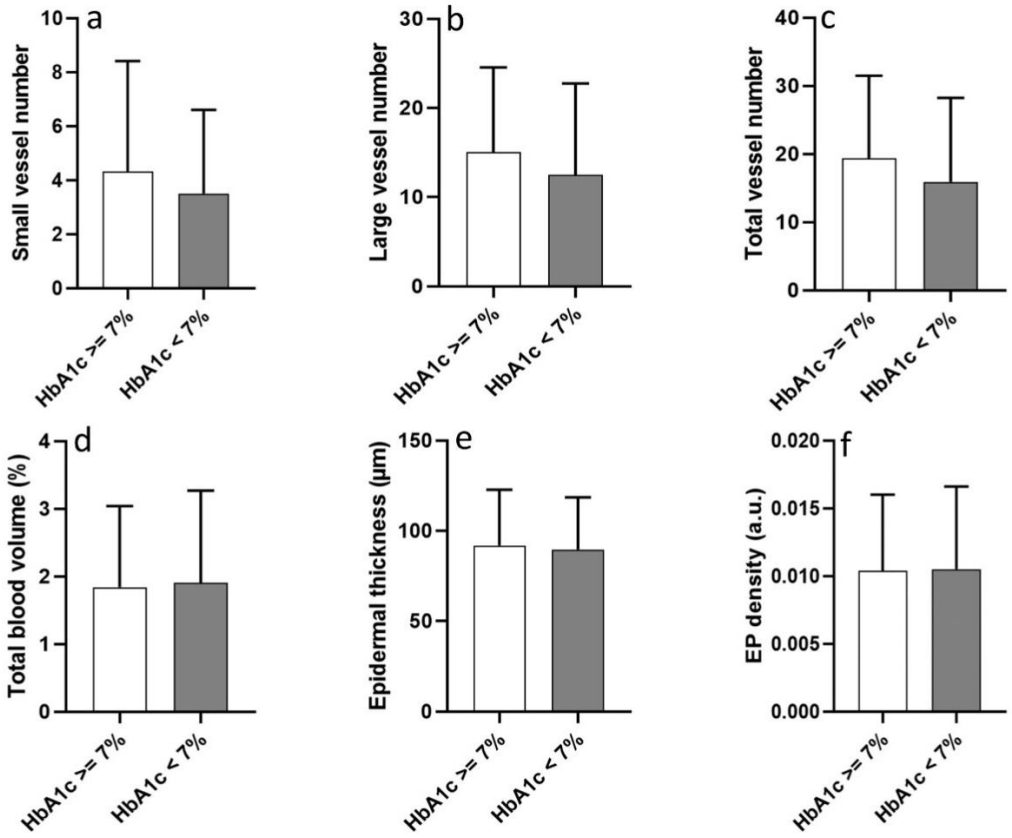

Figure S9. **Quantification of RSOM features associated with HbA1c values.** 72 participants with diabetes from the first dataset were grouped based on HbA1c values as follows: HbA1c >= 7% (n=34), HbA1c < 7% (n=38). Comparisons between the two HbA1c groups were carried out for six RSOM features: (a) Total number of small vessels (with diameter <= 40 µm) in DR layer; (b) Total number of large vessels (diameter > 40 µm) in DR layer; (c) Total vessel numbers in DR layer; (d) Total blood volume in DR layer; (e) Thickness of EP layer; (f) Signal density of EP layer. It can be noticed that the HbA1c values did not significantly affect the RSOM biomarkers examined. EP: Epidermis, DR: Dermis, HbA1c: Glycated hemoglobin.

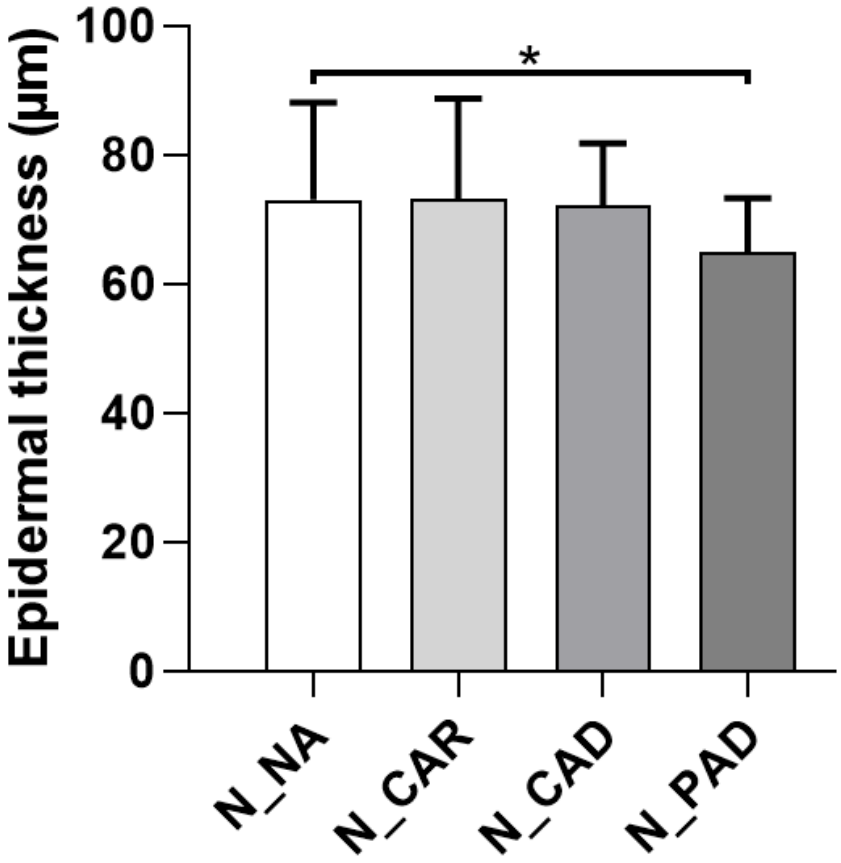

Figure S10. **Quantification of epidermal thickness in participants with diabetes with neuropathy and the presence of atherosclerosis**. Participants with diabetes were grouped as follows: N_NA (n=25), diabetic subjects with neuropathy and no atherosclerosis; N_CAR (n=7), diabetic subjects with neuropathy and carotid atherosclerotic disease; N_CAD (n=11), diabetic subjects with neuropathy and coronary artery disease; N_PAD (n=10), diabetic subjects with neuropathy and peripheral arterial disease; * Represents $P < 0.05$. The Epidermal thickness of the N_PAD group (64.89±8.43 µm) is significantly lower than in the group N_NA (73.02±15.08 µm).

Classification between participants with diabetes and healthy volunteers based on RSOM biomarkers. As demonstrated in Fig. 1 and 2, the RSOM biomarkers (Total blood volume and Small vessel number) were the two most indicative markers of diabetes (see Fig.1, 2), providing the starkest contrast between groups with or without diabetes. To investigate how RSOM biomarkers differentiate participants with diabetes from healthy volunteers, we trained a simple linear SVM (support vector machines) model to classify the participants with diabetes and the healthy volunteers. Since the RSOM data were collected from two hospitals and we simply separated them into the primary cohort (dataset 1 acquired from the first hospital: 72 participants with diabetes and 20 healthy volunteers) and the testing cohort (dataset 2 acquired from the second hospital: 23 participants with diabetes and 28 healthy volunteers). All patient information is listed in Table I and supplementary Table I. The total data (dataset 1 + dataset 2) based on the values of the two biomarkers were divided into four groups: non-diabetic volunteers from dataset 1 (NV-1, n=20), participants with diabetes from dataset 1 (DP-1, n=72), non-diabetic volunteers from dataset 2 (NV-2, n=28), participants with diabetes from dataset 2 (DP-2, n=23). As shown in Fig. S11a, the SVM classifier achieved 89.1% accuracy with 88.8% sensitivity and 90.0% specificity based on the biomarker of TBV (Total blood volume), while 90.2% accuracy with 93.1% sensitivity and 80.0% specificity was obtained using the biomarker of SVN (Small vessel number). Receiver operating characteristic (ROC) curves (Fig. S11b) were constructed based on the biomarkers of the TBV and SVN, revealing an area under the ROC curve (AUC) of 0.91 and 0.93 respectively. The combination of the two biomarkers resulted in a higher accuracy of 91.3% with 93.1% sensitivity and 85.0% specificity. Furthermore, we tested the classifier trained from the primary cohort on the testing cohort and achieved the prediction classification accuracy of 84.1% with 82.6% sensitivity and 82.1% specificity, which suggested that the SVM classifier determined by the two biomarkers performs well in classifying the participants of the testing cohort into the non-diabetic or the diabetic groups.

a

Biomarkers	Accuracy	Sensitivity	Specificity	AUC
TBV	89.1%	88.8% (64/72)	90.0 % (18/20)	0.91
SVN	90.2%	93.1% (66/72)	80.0% (16/20)	0.93
SVN +TBV	91.3%	93.1% (67/72)	85.0% (17/20)	0.94
Prediction	84.1%	82.6% (19/23)	82.1% (23/28)	

b

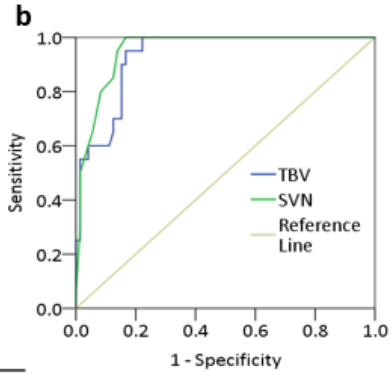

Figure S11. **Classification model to differentiate participants with diabetes and healthy volunteers**. The total data was grouped into a primary cohort (dataset 1, 72 participants with diabetes and 20 volunteers without diabetes) and a testing cohort (dataset 2, 23 participants with diabetes and 28 volunteers without diabetes). The total dataset was divided into four groups: non-diabetic volunteers from dataset 1 (NV-1, n=20), diabetic participants from dataset 1 (DP-1, n=72), non-diabetic volunteers from dataset 2 (NV-2, n=28), diabetic participants from dataset 2 (DP-2, n=23). The black line indicates the position of the linear SVM classifier based on the combination of the two biomarkers. a. Classification accuracy, sensitivity, specificity, and the AUC values computed by the linear SVM classifier on dataset 1. The trained SVM classifier was tested on dataset 2 with the prediction values. b. ROC plots in the differentiation of diabetes using TBV and SVN separately. TBV: Total blood volume, SVN: Small vessel number, ROC: Receiver operating characteristic, AUC: Area under the ROC curve.

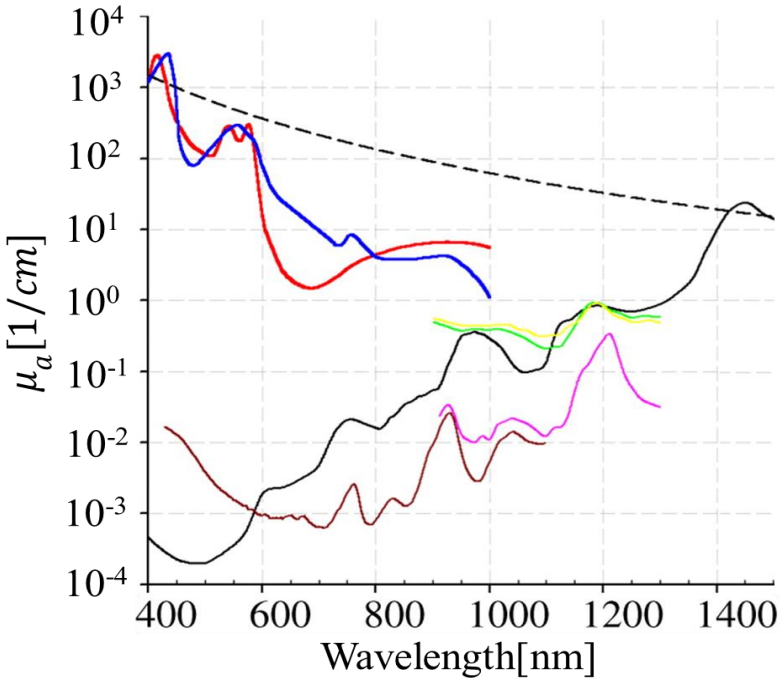

Figure S12. **Absorption coefficient spectra of several endogenous tissue chromophores.** Red line: oxyhemoglobin; blue line: deoxyhemoglobin; black line: water; brown line: lipid; black dashed line: melanin; green line: collagen: green line; and yellow line: elastin: yellow line. Data compiled by Scott Prahl, Oregon Medical Laser Center (http://www.omlc.ogi.edu/spectra).

Supplementary information accompanies the manuscript on the Light: Science & Applications website (http://www.nature.com/lsa)

Bibliography

1. Schwarz, M., Garzorz-Stark, N., Eyerich, K., Aguirre, J. & Ntziachristos, V. Motion correction in optoacoustic mesoscopy. *Sci Rep***7**, 10386 (2017).
2. Chiu, S.J.*, et al.* Automatic segmentation of seven retinal layers in SDOCT images congruent with expert manual segmentation. *Optics express***18**, 19413-19428 (2010).